Kinetic Stabilisation of the Internal Kink Mode for Fusion Plasmas

Division of Theoretical Mechanics
School of Mathematical Sciences

Jonathan Peter Graves

A thesis submitted to the University of Nottingham for the degree of Doctor of Philosophy, December 1999.

To my mother and father

Contents

Abstract

Attaining ignited plasmas in next-step tokamaks requires the avoidance of strong sawtooth activity in the plasma core. This has motivated studying correlations between observed sawtooth behaviour and theoretical models describing the effects of collisionless populations of ions on the internal kink mode. An energy principle approach has been developed which allows the kinetic effects of collisionless ions on MHD modes to be studied. The analysis accounts for linear wave-particle interaction, which in some cases is stabilising to the internal kink mode and in others destabilising. The stability boundary depends sensitively on the distribution of the collisionless population and the equilibrium.

The recent Joint European Torus deuterium-tritium campaign has yielded ion cyclotron resonance heated (ICRH) pulses during which both the sawtooth characteristics and the ICRH minority ion population both evolve substantially. At multiple times during each pulse, the evolution of the kinetic–fluid MHD potential energy is calculated from measurement of the energetic ions and compared with the evolving sawtooth duration. It is shown that there is a strong correlation between sawtooth duration and minority ion stabilisation of the ideal internal kink.

Thermal ions in the banana regime also give rise to significant deviations from the ideal MHD internal kink mode stability threshold. However, the behaviour of such ions are found to be sensitive to the equilibrium electric field and the induced sheared plasma rotation. An analysis is presented which includes the effects of the equilibrium electric field and plasma rotation. For changing levels of plasma rotation, the calculated critical pressure for internal kink displacements can change by a factor of two.

The Author

The author was born on the 15th of May 1974 in Stamford, Lincolnshire. He attended school at Casterton Community College, Rutland, and was educated to eighteen years at Stamford College for Further Education. He gained a first class degree in Electronic Engineering and Mathematics from the University of Nottingham and has accepted a research post at British Aerospace Sowerby Research Centre, Bristol.

Acknowledgements

I take this opportunity to acknowledge my colleagues, friends and family. I thank my supervisors Keith Hopcraft and Richard Dendy for their inspiration and guidance throughout my Ph.D. I am especially indebted to Keith, who, through his enthusiastic and coherent approach to lecturing and supervision, has inspired in me a genuine interest in scientific research. I also thank Jim Hastie for graciously sharing a wealth of expertise and providing invaluable guidance. I express my gratitude to colleagues Ken McClements, Mervi Mantsinen and the late David Start for their contributions to journal submissions and access to JET data. In addition, I acknowledge financial assistance from the Engineering and Physical Sciences Research Council and UKAEA Fusion.

I should also like to acknowledge my excellent friends Jon and James for always supporting and encouraging me despite living a distance apart over recent years. Finally, my warmest thanks are saved for my parents and for Jen who has endured all stages of this thesis.

Declaration

No portion of the work referred to in the thesis has been submitted in support of an application for another degree or qualification of this or any other university or other institute of learning.

Chapter 1

Introduction

At a time when there is an increasing need to produce environmentally friendly energy there are few practical sources capable of meeting current energy demand. Controlled nuclear fusion however promises to be a safe and efficient source of energy. The most accessible fusion reaction is that forming helium 'He' and a neutron 'n' from deuterium D and tritium T, where the energy released is 17.6 MeV per reaction:

$$\mathrm{D} \quad + \quad \mathrm{T} \quad \longrightarrow {}^{4}\mathrm{He}\ (3.5\ \mathrm{MeV}) \quad + \quad \mathrm{n}\ (14.1\ \mathrm{MeV}).$$

In order to induce D-T fusion it is necessary to overcome the mutual repulsion due to the positive charges of the nuclei. The most promising method of supplying the energy is to heat the D-T fuel to a sufficiently high temperature that the thermal velocities of the nuclei are high enough to produce the required reactions. Fusion brought about in this way is called thermonuclear fusion. The necessary temperature is around 20 keV ($\sim 2 \times 10^8$ °K). At such a temperature the fuel is fully ionised and the resulting state of matter is termed 'plasma'. In a reactor it would be necessary to confine a sufficiently dense plasma for a time which allows an adequate fraction of the fuel to fuse. At an ion density of around $10^{20}\mathrm{m}^{-3}$ and a fuel temperature of 20 keV the Lawson criterion [1] indicates that the confinement time must be greater than 1 second.

The most successful approach for achieving this objective is by confining the plasma in a tokamak configuration. In a tokamak, shown schematically in Fig. 1.1, currents in external coils create a strong toroidal magnetic field. A current through the plasma is induced by a transformer with the plasma forming the second winding. The plasma current provides heating through Ohmic dissipation, and also creates a poloidal magnetic field. Consequently, the plasma current produces the helical magnetic field line structure inherent in tokamak plasmas. The toroidal surfaces on which the helical field lines lie are known as flux surfaces. Because a tokamak is an axis-symmetric device, a single field line covers an entire flux surface. However, exceptions to this occur at 'rational surfaces'. Here the field lines close on themselves after an integer numbers of poloidal and toroidal circuits.

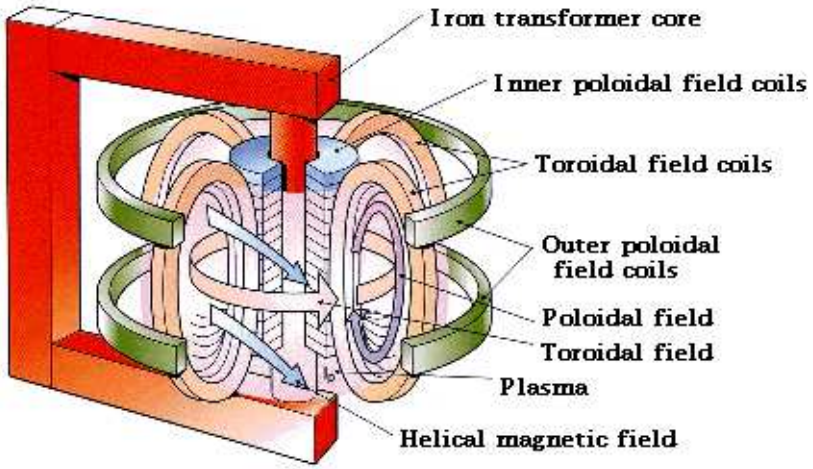

Figure 1.1: The configuration of a tokamak.

Each charged particle is confined to a helical orbit about a magnetic field line and consequently transport coefficients parallel to the magnetic field are much larger than perpendicular transport coefficients. Therefore, the density and pressure are approximately constant on a flux surface, while large gradients may exist across the flux surfaces.

Plasma heating by the Ohmic dissipation of the induced current is not a sufficient means of reaching the ignition conditions because the electrical resistivity of the plasma falls as the electron temperature increases. To reduce the deficit, additional heating schemes are employed. Such schemes include the injection of neutral beam ions (NBI) and the launching of electromagnetic waves which resonate with the cyclotron frequency of a minority population of ions (ICRH). In both cases the resulting energetic ions form a minority of the overall population and therefore give up their energy to the bulk of the plasma population through collisions. Using such auxiliary heating techniques both the Joint European Torus (JET) and the Toroidal Fusion TEST Reactor (TFTR) have attained individual elements of the ignition conditions. In particular JET has achieved a peaked fusion power of 16 MW [2]. It is widely agreed, however, that a larger tokamak such as the International Thermonuclear Experimental Reactor (ITER) [3] is required if the Lawson criteria [1] is to be satisfied. It is envisaged that the next step tokamak will ignite and become entirely self heating through the increased yield of fusion born alpha particles (^{4}He).

A problem which has been apparent since the earliest experiments is the occurrence of instabilities. All instabilities limit the achievable confinement and the internal disruption or sawtooth instability [4] is no exception to this. This instability causes a rapid redistribution of the hot central plasma, so that the initially peaked density and temperature profiles are flattened close to the centre of the tokamak. When heating of the plasma continues, the peaked profiles reform, only to collapse once more whenever some threshold is exceeded. It is of interest to exploit a means of

delaying the sawtooth crash because in doing so, the hot plasma is confined in the centre for longer which ultimately allows for an increased fusion yield. The importance of sawtooth suppression was especially highlighted in the recent D-T campaign at JET [2]. An example is given in Fig. 1.2, where in the first of two apparently very similar discharges a large sawtooth occurs, limiting the fusion power considerably. In the second discharge the fusion power reached the record, for that time, of 12.9 MW.

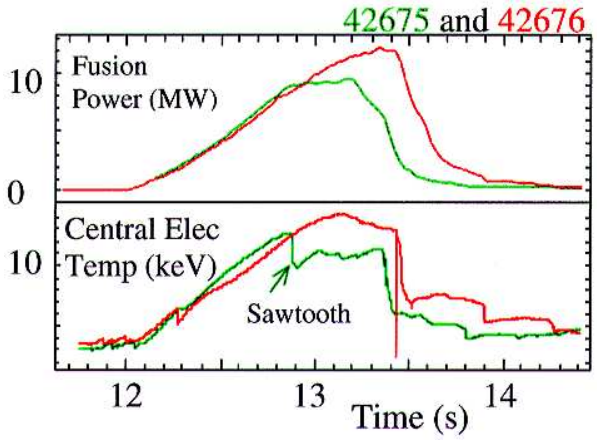

Figure 1.2: Illustrating the comparison of two JET DT discharges: conditions were almost identical until a giant sawtooth in 42675 degraded the performance. Discharge 42676 does not exhibit giant sawteeth and a record fusion power was measured. The record has subsequently been superseded.

A precursor oscillation, is often observed prior to the crash event. Experiments show that it has the topology of the internal kink mode. The internal kink mode comprises a fundamental MHD oscillation of the form $\sim \exp(i\theta - i\phi - i\omega t)$, where θ and ϕ are the poloidal and toroidal angle respectively, $\Re\{\omega\}$ is the rotation frequency and $\gamma = \Im\{\omega\}$ is the growth rate of the kink mode. The instability is located in the tokamak where the wave propagates perpendicularly to the magnetic field line. At this location, commonly known as the $q = 1$ rational surface, the field lines do not react in response to the travelling wave and the stabilising influence of magnetic field line bending is lost. The remaining stabilising and destabilising influences on the internal kink mode are usually quantified using energy principle methods [5].

The collective motion of collisional particles frozen in the magnetic field is adequately described by the MHD approach, but this is not the case for energetic particles whose motion is decoupled from the magnetic field lines. Their dynamics are best described using the guiding centre approach in which their rapid gyration and resulting helical path is approximated by a smooth drifting trajectory. The energy principle has been extended to include the behaviour of such populations [6]. The effects of collisionless populations of alphas, ICRH, NBI and energetic thermal ions on the internal kink mode stability have all been considered - but with varying success.

It is now recognised that populations of collisionless ions such as those produced by auxiliary heating, affect the sawtooth instability. Perhaps the most direct exper-

imental evidence is observed in ICRH heated plasmas where the sawteeth have been delayed for several seconds in JET [7, 8, 9]. Plasmas heated with NBI do not usually exhibit strong sawtooth stabilisation unless heated in conjunction with ICRH [9]. Evidence for alpha particle stabilisation is probably premature because the density of fusion alphas as opposed to auxiliary heated minority particles has thus far been small. However, alpha particle stabilisation of sawteeth has been predicted in 'ITER like discharges' on a very large scale [10].

Analysis involving the kinetic effects of collisionless populations on the internal kink mode requires detailed knowledge of the plasma equilibrium. The most crucial quantity is the hot ion distribution function. Advances have been made in the measurement and modelling of ICRH distribution functions. However, internal kink calculations based on accurate models of the ICRH distribution functions have until recently been scarce. Some equilibrium quantities are often neglected in internal kink calculations altogether. Such quantities include the equilibrium electric field and the induced toroidal plasma rotation. It is envisaged that the inclusion of a more detailed equilibrium into the internal kink stability analysis should provide a greater understanding of the behaviour of sawteeth.

The goal of this thesis is to extend the analysis of the internal kink mode by introducing a more accurate representation of the experimentally observed equilibrium. The thesis concentrates on the collisionless effects of ICRH populations and energetic thermal ions. ICRH discharges have thus far produced scenarios with the greatest observed sawtooth suppression [7, 8, 9], and have clearly demonstrated the link between sawtooth activity and the behaviour of energetic ions [11]. An accurate model for the ICRH minority distribution function is used to represent the kinetic component of the equilibrium. The largely analytical theory that follows is ultimately used to demonstrate strong correlations with experiment. This thesis also contains a detailed analysis of the kinetic effects of thermal ions in the banana regime. The effects of the equilibrium electric field and sheared flows are also included in the theory. The calculations suggest that the effects of the equilibrium electric field in hybrid plasmas can significantly modify the internal kink mode stability.

The thesis is organised as follows. Chapter 2 presents a historical review of the theoretical and experimental evidence for kinetic stabilisation of the internal kink mode. Also detailed in Chapter 2 is the linear MHD description of the internal kink mode. Chapter 3 begins by introducing various aspects of single particle theory and the drift kinetic equation. These results are then coupled with those of Chapter 2 and the fundamental kinetic extensions of the internal kink mode are derived. Chapter 4 continues from the review chapters by introducing and deriving further kinetic effects. Subsequently, various regimes and scenarios are described and new results and insights discussed. In Chapter 5 ICRH discharges from the recent deuterium - tritium campaign are analysed. Ideal internal kink mode models are employed based on the theory described in Chapter 4 and subject to parameters inferred from the JET discharges. In Chapter 6, the analysis describing the ideal internal kink mode is extended to include the equilibrium electric field and induced plasma rotation. These effects are included in numerical evaluations of internal kink stability for plasmas in the banana regime. Finally, in Chapter 7 the thesis concludes with a summary of the

major results and their implications, together with suggestions for further work.

Chapter 2

Theoretical Review

2.1 Historical Overview of the Internal Kink Mode

The avoidance and control of large scale instabilities has constituted a large fraction of experimental and theoretical plasma physics over the last few decades. Experiments show that the stability boundaries of gross instabilities determine the normal operating regime of tokamaks. Indeed, to trigger one results in complete loss of the plasma. The sawtooth instability is an exception to this insofar as the plasma recovers. It is a macroscopic instability which affects the hot and dense plasma core but it does not usually terminate a discharge, rather the core recovers and the instability repeatedly occurs in a regular manner. The sawtooth was first reported by von Goeler *et al* [4] and is a feature common to all tokamaks. The complete sawtooth cycle is illustrated in Fig. 2.1, where the following three regimes are clearly observed.
1. The sawtooth ramp phase; a quiescent period during which the central plasma density and temperature increase approximately linearly in time.
2. The precursor oscillation phase during which the helical perturbation exhibits growing oscillatory behaviour.
3. The collapse phase in which the central electron temperature and density fall rapidly.

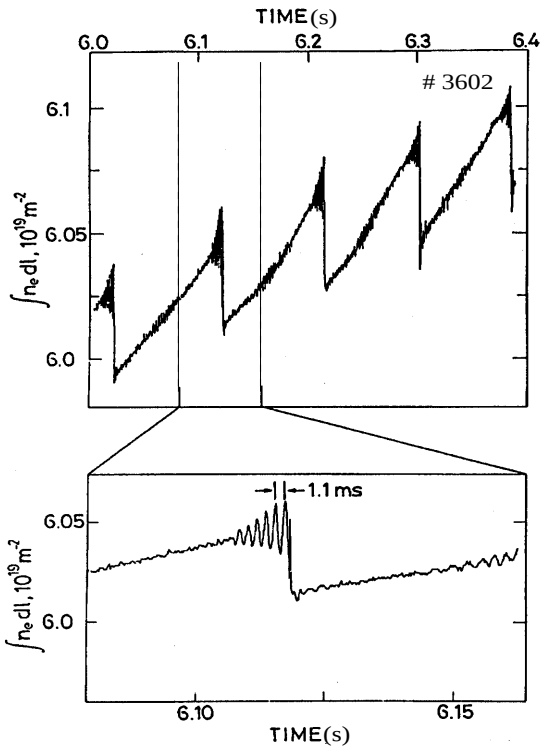

Figure 2.1: Showing the line integrated electron density measured from an early sawtoothing discharge at JET. The sawtooth comprises of a ramping phase, a precursor oscillation and a collapse phase.

When a sawtooth collapse (or crash) occurs, hot electrons transport rapidly across flux surfaces into a cooler region away from the centre. As a consequence the temperature profile is flattened rapidly during the collapse phase. The 'mixing radius' is the location at which the temperature is observed not to change during a sawtooth cycle. Measurements of the mixing radius can provide a good estimate of the instability location. It is found experimentally that the sawtooth precursor has a $m = n = 1$ topology, where m and n are the poloidal and toroidal mode numbers respectively. Such a growing oscillation is described by an internal kink mode perturbation, i.e. $\sim \exp(i\theta - i\phi + \gamma t)$, where θ is the poloidal angle and ϕ the toroidal angle, as shown in Fig. 2.2. Also shown in Fig. 2.2 is the minor radius r, plasma edge radius a, major radius R, axial major radius R_0 and the vertical height Z.

Since the phase of the mode is conserved the mode twisting number is defined $d\phi/d\theta = m/n = 1$. In a large aspect ration tokamak, the magnetic field line twisting number, which is commonly known as the safety factor, is defined as $q \equiv d\phi/d\theta = rB_\phi/R_0B_\theta$, where B_ϕ is the toroidal magnetic field and B_θ is the poloidal magnetic field. In the case of sawteeth, a resonance exists at the rational surface located where the twisting of the field line and mode match, i.e. $q(r = r_1) = 1$. The instability

can therefore only exist if the local value of the safety factor falls below unity. The safety factor is usually a monotonically increasing function of the minor radius r and from Ampère's law, the existence of a flux surface with $q < 1$ corresponds to an axial toroidal current density $j_\phi(0)$ exceeding $2B_\phi(0)/(R_0\mu_0)$.

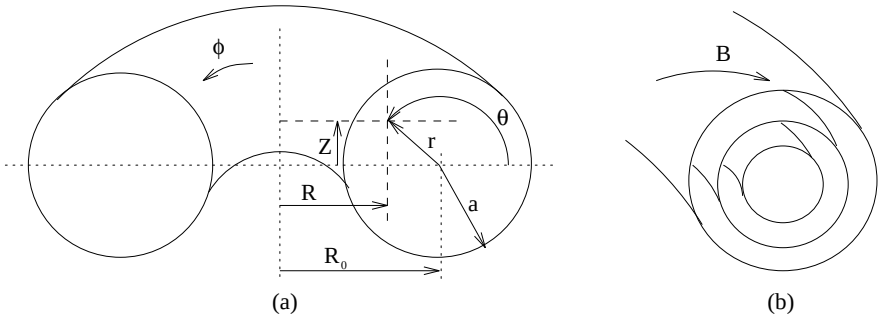

Figure 2.2: Showing (a) the cylindrical coordinate systems (R, ϕ, Z) and (r, θ, ϕ) where R is the major radius, Z the vertical height ϕ the toroidal angle, r the minor radius and θ the poloidal angle. Also shown is the plasma edge radius a. In (b), examples of nested toroidal flux surfaces or constant pressure surfaces are illustrated.

Experiments in a number of tokamaks including JET [12] have demonstrated that whilst q_0 ramps down during the quiescent period, it often remains well below unity during the whole sawtooth cycle. These observations indicated that $q < 1$, is a necessary but not sufficient condition for the sawtooth collapse.

When the sawtooth was first reported, only two relevant calculations were known. These concerned the ideal linear MHD instability [13] and its saturated amplitude [14]. Both of these used energy principle methods to analyse the ideal MHD stability. The energy principle is described in detail later in this chapter, but its basic philosophy can be summarised briefly as follows. A variational scheme is used to minimise the potential energy δW with respect to a perturbed MHD displacement $\boldsymbol{\xi}$. If, for a particular equilibrium, it is found that $\delta W < 0$, then the plasma is unstable to the perturbation.

Shafranov [13] minimised δW with respect to $\boldsymbol{\xi} = \boldsymbol{\xi}(r)\exp(i\theta - i\phi - i\omega t)$. The analysis was made tractable by letting the 'local inverse aspect ratio' $\varepsilon = r/R_0$ be a formal expansion parameter. Shafranov assumed a cylindrical plasma column and expanded δW to second order in the local inverse aspect ratio. It was found that a top-hat displacement (which takes the form of a uniform tilt and shift of the plasma inside r_1 and zero displacement outside) minimises the potential energy to zero, thus requiring δW to be determined to higher order in ε. Rosenbluth *et al* [14] reported a linear and non-linear ideal cylindrical MHD treatment up to fourth order in the aspect ratio together with an analysis of the layer region (a region centred about r_1). Rosenbluth *et al* [14] showed that the discontinuity of the top-hat displacement at r_1

is removed by allowing for the effects of finite inertia. This analysis yielded a linear relationship between the growth rate $\gamma = \Im\{\omega\}$ of the internal kink mode and the minimised fourth order potential energy of the external region (far away from the inertial layer).

Soon after the first reported observation of sawteeth, Bussac *et al* [15] again tackled the problem up to fourth order in ε but this time took into account the effects of toroidal curvature. In the all important $m = n = 1$ case, Bussac *et al* showed that the fourth order cylindrical terms derived in Ref. [14] are exactly cancelled by some of the new toroidal terms resulting in only pure toroidal curvature effects remaining. Bussac *et al* [15] were then at liberty to use the singular layer analysis of Ref. [14] thus linking the growth rate to the new minimised potential energy. Upon considering a parabolic q profile it was shown that the mode is unstable for,

$$\beta_p = -\frac{2\mu_0}{B_0^2 \varepsilon_1^2 r_1^2} \int_0^{r_1} r^2 \frac{dP}{dr} dr > 0.3, \tag{2.1}$$

where β_p is the poloidal beta measured at r_1, μ_0 is the permeability of vacuum, B_0 is the axial magnetic field strength, P is the plasma pressure and $\varepsilon_1 = r_1/R_0$, the inverse aspect ratio at r_1. The poloidal beta is one of many definitions used for characterising the efficiency of the confinement. β_p is essentially the ratio of the plasma internal energy and the poloidal magnetic energy. For more realistic q profiles, which are flatter inside r_1, the threshold poloidal beta corresponds to $0.1 < \beta_p^c < 0.2$, depending on the exact safety factor profile.

Some other important results should be mentioned at this point. Glasser *et al* [16] realised that in the singular layer region, the toroidal component of the inertia competes with the poloidal component. This adjusted the equation for the growth rate by a factor of $\sqrt{3}$. Also, Bussac *et al* [17] and later Ara *et al* [18] generalised the linear resistive theory of Ref. [19] to include the separate behaviour of ion and electron fluids. The result most crucially affecting the ideal stability is the effect of finite ion Larmor radius in the singular layer. The modification is seen as a shift in the ideal eigenvalue, ω, and the corresponding dispersion relation is defined as:

$$i\sqrt{\omega(\omega - \omega_{*pi})} \propto \delta W,$$

where δW is the potential energy of the mode minimised to fourth order (e.g. Bussac's expression [15]), and $\omega_{*pi} = -P_i'/(eZn_iB_0r)$ is the pressure weighted ion diamagnetic frequency. Here, P_i' is the radial derivative of ion pressure, n_i is the ion density, e is the proton charge, Z is the charge number ($Z = 1$ for hydrogen isotopes) and B_0 is the axial magnetic field strength. Note that two solutions of differing magnitude exist, whereas single fluid ideal MHD predicts $i\,|\omega| \propto \delta W$.

Bussac's [15] result agrees with the hypothesis that the observed quiescent ramping of the density and temperature induces a pressure driven trigger. In conflict with this, tokamak discharges where the heating is Ohmic alone, regularly display sawtooth activity at much smaller values of β_p (~ 0.05), implying the internal kink instability observed prior to each sawtooth collapse is not of ideal MHD character. Neither do many researchers consider ideal MHD capable of describing the sawteeth trigger

condition. The three other main branches having been used to assess the trigger problem [20] are:
(1) resistive single fluid MHD [19],
(2) two fluid, resistive equations [17, 18],
(3) MHD plus the kinetic treatment of a collisionless population of ions.
This review will continue by reporting the essential developments made in the ideal (non-resistive) limit of (3) together with some vital experimental evidence.

The energy principle is useful for several reasons. It allows for both a tractable determination of stability as well as aiding in understanding competing physical processes. Furthermore, in many instances the minimisation of the energy principle potential energy provides access to the solutions of the exact equations of motion (e.g. see Refs. [13, 14, 15]).

The motivation for developing a kinetic energy principle is the need for a simplified description of the collisionless plasma. MHD deals only with the fluid displacement $\boldsymbol{\xi}$ which is a function of position. In the collisionless case one must also compute the distribution function, which depends on both position and at least two coordinates in velocity space. Hence, a kinetic energy principle can provide a shortcut to solving a nearly intractable problem. It renders a method of determining stability by only considering trial functions and minimisation with respect to $\boldsymbol{\xi}$.

To develop a useful energy principle one must introduce constraints on the plasma behaviour under consideration. For example one may adopt the assumption that the plasma and the magnetic field move together (which is the behaviour that obtains as a consequence of the ideal Ohm's law $\boldsymbol{E} + \boldsymbol{v} \times \boldsymbol{B} = 0$). Also, to remove a degree of complexity one may consider a reduced description of the plasma such as the guiding centre model (see Chapter 3). Construction of a useful energy principle also invariably requires making assumptions about relative time scales [21]. Only two energy principles [22, 6], each with different time scales, are described here.

In both [22] and [6], the potential energy comprises the sum of a fluid component δW_f, and a kinetic component δW_k. If it is assumed that the equilibrium is isotropic, the fluid term δW_f is simply the ideal MHD energy principle term. Whichever time scale is of interest, δW_k has a contribution from the perpendicular compression of the fluid. In fact $\boldsymbol{\nabla} \cdot \boldsymbol{\xi}_\perp = 0$ gives $\delta W_k = 0$.

Kruskal and Oberman [22] showed that a kinetic energy principle must contain the effects of heat flow along magnetic field lines. Using a guiding centre model consistent with the ordering $\partial/\partial t \sim \boldsymbol{v}_\parallel \cdot \boldsymbol{\nabla}$, which treats kinetically the particle motion along field lines, Kruskal and Oberman [22] derived,

$$\delta W(\boldsymbol{\xi}, \boldsymbol{\xi}^*) = \delta W_f(\boldsymbol{\xi}, \boldsymbol{\xi}^*) + \delta W_{kK}(\boldsymbol{\xi}, \boldsymbol{\xi}^*).$$

where again δW_{kK} represents the energy required to compress the plasma perpendicularly. It can be shown that δW_{kK} is positive definite and increasingly stable with respect to increasing $\boldsymbol{\nabla} \cdot \boldsymbol{\xi}_\perp$. The evaluation of δW_{kK} requires orbit averages and integrations over energy and pitch angle space of particles. The Kruskal and Oberman [22] energy principle has been used relatively recently to model the stability of the internal kink mode in plasmas containing collisionless thermal ions. For example in

Ref. [23] it was used for the case of 'ultra flat q profiles', and also in Ref. [24] where it was shown that the internal kink mode is stable if

$$(1-q_0)[\beta_p^2-(\beta_p^c)^2]-\frac{\mu_1\sqrt{2\varepsilon}}{8\pi\varepsilon^2}\beta_i<0, \tag{2.2}$$

where β_p^c is poloidal beta at which the ideal MHD stability calculated by Bussac [15] is marginal (e.g. for parabolic q profile $\beta_p^c=0.3$), $\mu_1\approx 1.1$ is a coefficient proportional to an approximate solution of the inherent pitch angle integrals (see Chapter 3), and

$$\beta_i=\frac{5\mu_0}{2r_1^{5/2}}\int_0^{r_1}drr^{3/2}\frac{2P_i}{B^2}, \tag{2.3}$$

with μ_0 the permeability of a vacuum. Equation (2.2) is a limiting solution of the stability criterion used in this thesis to analyse the stability of the internal kink mode for plasmas with energetic thermal ions.

Some time after the Kruskal and Oberman calculation it was pointed out [6] that some collisionless instabilities may have mode frequencies sufficiently small to fall outside the correct regime of Ref. [22]. Antonsen *et al* [6] demonstrated that the analysis for modes satisfying $\partial/\partial t << \boldsymbol{v}_{||}\cdot\boldsymbol{\nabla}$ requires the drift of particles with respect to the non-homogeneity of the magnetic field. Subsequently Antonsen *et al* [25] derived a collisionless energy principle for modes satisfying $\partial/\partial t\sim\boldsymbol{v}_{md}\cdot\boldsymbol{\nabla}$, where $\boldsymbol{v}_{md}$ is the magnetic drift velocity. The result is

$$\delta W(\boldsymbol{\xi},\boldsymbol{\xi}^*)=\delta W_f(\boldsymbol{\xi},\boldsymbol{\xi}^*)+\delta W_{kA}(\boldsymbol{\xi},\boldsymbol{\xi}^*).$$

Antonsen *et al* [25] showed that δW_{kA} is not only smaller than δW_{kK} but can, depending on the equilibrium conditions and specific mode in question, also change sign, and thus alerted to the possibility of new instabilities not described previously.

Some of the first investigations concerning the effect of energetic particles came from studies of the ballooning mode. Connor *et al* [26] proposed that the introduction of an energetic anisotropic minority species can be stabilising. Initially however, the experimental evidence of fast particle stabilisation was not encouraging. In 1982 a new form of $m=n=1$ internal kink instability was observed on the Princeton Poloidal Divertor experiment (PDX) [27]. Like the precursor oscillation of the sawtooth instability, the new instability, known as the 'fishbone', appeared as a slowly growing and oscillating signal (both in electron temperature and poloidal magnetic field) rotating in the toroidal direction. In contrast to the sawtooth however, no rapid thermal collapse phase was observed, rather the oscillating signal grows and then decays in amplitude giving the characteristic 'fishbone' signal. Measurements of the electron temperature and the time derivative of the poloidal magnetic field, as shown in Fig. 2.3, demonstrate that periods of quiescence alternate with bursts of fishbone activity in a regular manner. The fact that both fishbones and sawteeth are driven unstable by the internal kink mode implies that they are intricately linked. In fact, great insight into the kinetic behaviour of sawteeth has its origins in the theory of fishbones.

An explanation of the fishbone instability using the recent energy principles of Antonsen *et al* [25] was presented in [28]. In this work a distinction was made between

the two major components of the plasma: the plasma core (comprising collisional thermal ions and electrons) and a highly anisotropic collisionless minority species. The minority ion pressure can be ordered according to $P_{\perp h} \sim \varepsilon P_c$, where $P_{\perp h}$ is the perpendicular pressure corresponding to the hot ions and P_c the pressure of the core plasma. Because of this ordering the analysis of Ref. [15] for the core plasma stability and layer region still applies [28]. The potential energy of the energetic particles have associated with them two terms, both of which depend only on the leading order 'top-hat' displacement. The terms are fourth order in the inverse aspect ratio and correspond to a fluid component δW_{fh} and a kinetic component δW_{kh}. Ignoring diamagnetic effects in the layer the dispersion relation for ω becomes [28],

$$i\,\omega \;\propto\; \delta W_{fc} + \delta W_{fh} + \delta W_{kh}(\omega),$$

where δW_{fc} is the core plasma term [15], and we note that both ω and δW_{kh} have real and imaginary parts. Chen *et al* [28] showed that δW_{kh} only contains the effects of trapped particles, and if there are enough of these, a destabilising mode can exist with an ordering $\omega_r \equiv \Re\{\omega\} \sim \langle\omega_{mdh}\rangle$ where $\partial/\partial t \equiv \omega$ and $\langle\omega_{mdh}\rangle$ is the bounce averaged magnetic drift of hot trapped particles corresponding to the quantity $\boldsymbol{v}_{mdh} \cdot \boldsymbol{\nabla}$.

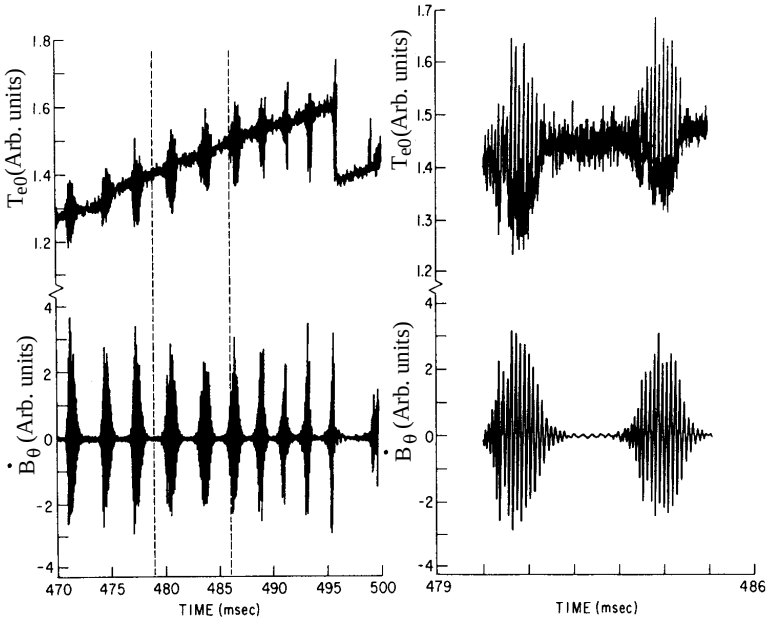

Figure 2.3: Both electron temperature and the time derivative of the poloidal magnetic field illustrate the characteristics of the fishbone instability.

The unique feature of the PDX device causing it to exhibit the instability so clearly lay in the fact that the angle of the neutral beam injection (NBI) was nearly perpendicular

to the toroidal field. The NBI power was also higher than any other machines at that time and meant that there were enough trapped minority particles at a high enough energy to exceed the threshold for the fishbone instability [28].

After the implications of Ref. [28] were realised much theoretical work followed. Some of this focused on another fishbone instability defined with an ordering $\omega_r \sim \omega_{*pi} \sim \langle \omega_{mdh} \rangle$ [29]. With this ordering the diamagnetic corrections to the layer cannot be neglected. By including these corrections, the ideal kink mode dispersion relation allows for the possibility that the mode could be a discrete eigenmode, existing within a gap in the Alfvén continuum [29]. The two fishbone modes of Refs. [28, 29] are in fact limiting solutions of a more general scenario.

Until 1986 both experiment and theory had suggested that energetic particles have only a detrimental effect on the internal kink stability. In 1986, however, JET carried out a series of high power ion cyclotron resonance heating (ICRH) experiments in which the sawtooth instability was suppressed for seconds at a time [7]. Figure 2.4 illustrates further ICRH experiments [11] where sawtooth quiescent periods were interrupted by a sawtooth collapse which followed the switch off of ICRH with a time lag of 60 – 80 ms - comparable to the slowing down time of energetic ions. This clearly confirmed that the ICRH minority ions were providing a stabilising influence to sawteeth. Sawtooth stabilisation with ICRH was subsequently verified in TFTR [9].

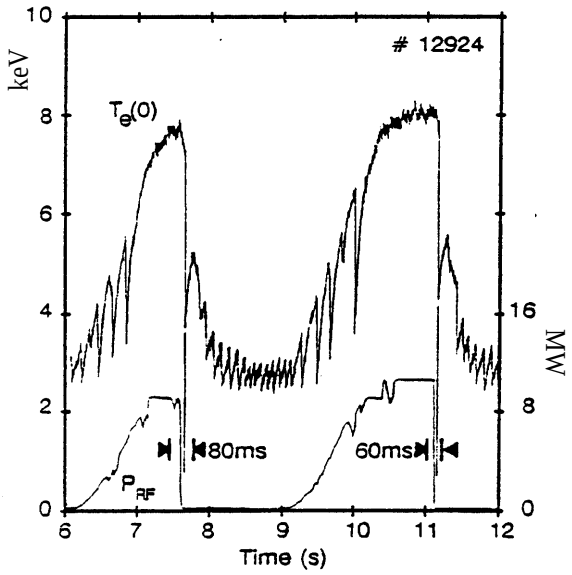

Figure 2.4: Showing one of the JET 'ICRH switch-off' discharges [11]. The figure displays a correlation between the ICRH power P_{RF}, and central electron temperature T_{e0}. The sawteeth were stabilised for about one second and the collapse was triggered 60-80 ms after the abrupt switch-off of P_{RF}, a delay comparable to the slowing down time of the energetic ions.

After the experimental reports on the stabilisation of sawteeth, a flurry of research activity began. Much of this was inspired by the earlier fishbone analysis. Perhaps most notable are Refs. [30, 31, 32]. In these papers a distinction was made between the two branches of the hybrid internal kink mode dispersion relation

$$i\sqrt{\omega(\omega-\omega_{*pi})} \propto \delta W_{fc} + \delta W_{fh} + \delta W_{kh}(\omega).$$

The lower frequency branch, thought to be responsible for sawteeth, was found to correspond to $\omega_r < \langle\omega_{mdh}\rangle$. A branch $\omega_r \sim \langle\omega_{mdh}\rangle$, thought to characterise the fishbone instability, was, in many cases, found to co-exist with the sawtooth oscillation branch.

In Ref. [30] the resistive and two-fluid analysis of Refs. [17, 18] was generalised to include an energetic minority population. White *et al* [30] demonstrated that energetic trapped particles have a strong stabilising influence on the resistive internal kink mode. Simplified distribution functions describing either ICRH or NBI heating were used. In both cases significant stabilisation was shown to be possible providing that the lower frequency branch satisfied $\omega_r < \langle\omega_{mdh}\rangle$. For the first time this provided estimates of lower bounds of the hot ion temperature and also explained why different levels of auxiliary heating can lead to contrasting sawtooth behaviour. Soon after this White *et al* [31] showed that a stability window can exist in a high β plasma which is completely stable to both sawtooth oscillations and the fishbone mode.

Coppi et al [32] also analysed the resistive kink mode. Specifically they examined the regime where $\omega << \langle\omega_{mdh}\rangle$ and corrected earlier assertions that $\Re\{\delta W_h(\omega=0)\} = 0$. However, Coppi *et al* failed to also correct for the fact that $\Im\{\delta W_h(\omega=0)\} \neq 0$, i.e. the Landau resonance of barely trapped energetic ions with the mode was neglected. Nevertheless, Ref. [32] illustrated the existence of stability windows in which the resistive internal kink was stabilised. Consequently, the paper added to the growing consensus that the kinetic additions to the MHD energy principle were, to some extent, taking account of the sawtooth stabilisation witnessed in experiments.

The limit $\omega << \langle\omega_{mdh}\rangle$, often used for studying sawteeth is usually justified in plasmas for which the minority ions are either Alpha particles or are heated by ICRH. For example, in JET and TFTR, ions heated with ICRH are often in the MeV range. Typically however, ions heated with NBI are an order in magnitude cooler, thus increasing the possibility that unstable modes with $\omega_r \sim \omega_{mdh}$ may exist. Porcelli [33] pointed out that the limit $\langle\omega_{mdh}\rangle >> \omega$ conserves the third adiabatic invariant [34], i.e. the magnetic flux encircled by the precessional drift orbits of fast ions. This means that the natural frequencies of trapped energetic ions are sufficiently high that the energetic ions do not react to periodic changes in the equilibrium. Instead, the energetic trapped ions provide rigidity to the area of the torus where particles usually tend to be destabilising: the region of bad curvature. In the limit of strong anisotropy $P_{\|h} \sim \varepsilon P_{\perp h}$, relevant for high power ICRH, and with $\langle\omega_{mdh}\rangle >> \omega$, it is possible to show that the leading order terms in δW_{fh} and δW_{kh} cancel with one another. For moderate shear and pressure the stabilising kinetic term wins. Hence, the overall result is stabilising and the approximate ideal stability criterion [32] is obtained:

$$\beta_{ph} \gtrsim \frac{\alpha_0}{4}\varepsilon_1\left[\beta_{pc}^2 - \left(\beta_{pc}^c\right)^2\right], \tag{2.4}$$

where $\varepsilon_1 = r_1/R_0$ is the inverse aspect ratio of the $q = 1$ rational surface and

$$\beta_{ph} = -\frac{2\mu_0}{B_0^2 \varepsilon_1^2 r_1^2} \int_0^{r_1} r^{3/2} \frac{d}{dr}\left(r^{1/2} P_{\perp h}\right) dr, \tag{2.5}$$

β_{pc} is the poloidal beta for the core plasma given by Eq. (2.1) and $\alpha_0 \sim 1/(1-q_0)$.

The analysis of Ref. [32] contained a number of approximations and assumptions. The energetic particle distribution function was assumed to comprise the sum of a small purely isotropic component and a single pitch angle component, thus aiding the complicated pitch angle integration. The model for the hot pressure profile required on-axis heating and was assumed to be of the form $P_{\perp h} \sim P_{0h} \exp(-r^2/D^2)$. It should be noted that whenever one attempts to calculate the stability criterion in ICRH plasmas one has to consider carefully the models used for the distribution function of the hot ions. Subsequent improvements on Ref. [32] have concentrated on a more realistic representation of the distribution function. However, such studies do not usually yield clear stability criteria, such as that of Eq. (2.4), because the energy and pitch angle integration can not be carried out analytically. Simpler calculations, and possibly more robust predictions, are possible when the energetic ions are alpha particles. In such cases the distribution function is isotropic and the calculations become more tractable [35].

Soon after the publication of Ref. [32], Porcelli *et al* [36] compared results from the newly reported theory with observed sawtooth behaviour at JET. Again, assumptions were made due to the difficulty in measuring the minority ion distribution function and of integrating the hot ion terms. In particular it was assumed that the hot ion pressure profile was identical to the the thermal ion pressure profile. Porcelli *et al* [36] were responsible for bringing to light some of the following general trends:
1) The hybrid model supported the experimental observation that an increased inversion radius $\approx r_1$ introduces stronger internal kink destabilisation.
2) High minority ion concentrations do not stabilise sawteeth as well as smaller concentrations. Porcelli argued that when the concentration is high, the RF coupling to the ions is inefficient and the tail temperatures are small. Therefore, the conservation of the third adiabatic invariant is less certain for high concentration levels, thus affecting the stability properties of energetic ions.
3) Only in a few specialised cases has NBI competed with ICRH for achieving sawtooth quiescent times of the order of 1s and, moreover, many NBI heated discharges are accompanied by fishbone activity. Porcelli argued that on JET most NBI power is injected at an energy per neutral of 80keV. At such an energy the third adiabatic invariant is not conserved and the stability window is obscured.

In an effort to link ideal stability to experimental observation at TFTR, Phillips *et al* [37] found similar trends to Porcelli [36]. One of their key observations was the peaking of current and pressure profiles during the quiescent phase of the sawtooth. Measurements of the poloidal magnetic field indicated that q on axis (q_0) decreases to a value of around 0.55 after a quiescent period of ~ 0.5 seconds has transpired. The ideal MHD - kinetic theory used in Ref. [37] predicted that a corresponding expansion of the $q = 1$ volume leads to increased instability as observed in many discharges.

Firmer comparisons between theory and experiment were essentially limited by two factors [33]. First, the stability threshold depends sensitively on parameters that are difficult to measure such as the q profile and the distribution function of energetic ions. Second, the theory may not be sufficiently developed. In this context equilibrium electric fields and sheared flows constitute additional effects which have not until now been considered [33] but are often measured as being significant. Indeed, some NBI experiments have suggested that sheared flow can influence sawtooth stability. Also, $m = 2$, $n = 1$ Resonant Magnetic Perturbations (RMP's) that are sufficiently large to lock the plasma to the $q = 2$ surface, eliminate sawtoothing altogether [38]. The sawteeth reappear when the RMP amplitude is reduced and the plasma rotation profile is altered.

In 1995 Dendy *et al* [39] worked on improving some of the assumptions and simplifications of previous analysis. The work used a realistic but analytically tractable model for the distribution function of the heated ions based upon the approach of Stix [40]. Here the level of anisotropy and the ICRH resonance position remain free parameters in the integral expressions. Dendy *et al* showed that the hot ion stability is almost invariant to changes in the level of anisotropy in the range $\varepsilon \lesssim P_{\|h}/P_{\perp h} \lesssim 1$. The result was consistent with a previous analysis [35] showing that the stability of the isotropic case is of the same order as the highly anisotropic case. In the isotropic limit the passing particles are more numerous and spend time in the region of good curvature thereby giving rise to stabilising terms which are of the same order as the destabilising trapped fluid terms. However, the kinetic term is smaller in the isotropic limit because the number of trapped particles are fewer. The overall result is similar in magnitude to the highly anisotropic case.

In the following year McClements *et al* [41] followed up the improved models of Ref. [39] and made further comparisons to JET experiments. Unlike other theorists McClements used an ordering where the hot ion pressure was comparable to the core pressure and the anisotropy was assumed only slight, i.e. $P_{\perp h} \sim P_c$ and $P_{\|h}/P_{\perp h} \sim \sqrt{\varepsilon}$. Such an ordering meant that the hot ions had to be included into the fluid toroidal curvature terms which before had only contained the core plasma. To do this a modified version of Ref. [15], capable of dealing with the small level of anisotropy [42] was used. The shaping of the toroidal cross sections was also considered [43] together with kinetic terms. The paper contained two major results based on discharges described in Ref. [8], two of which McClements *et al* described as discharge A and discharge B. The first result contained two ideal kink calculations, one made near the start of the sawtooth quiescent period of discharge A and another just proceeding the sawtooth crash. McClements *et al* showed that the expansion of r_1 and the decrease in q_0 did not alter the kinetic stabilisation significantly but did strongly destabilise both the toroidal terms and the shaping terms, which, in line with the experiment, destabilised the ideal internal kink.

The second result contained in Ref. [41] concerned the different characteristics exhibited by discharges A and B. In discharge A, the ICRH power was limited to 4.3 MW, whereas in discharge B, the ICRH power was set to approximately 6 MW. Aside from the contrasting hot ion tail temperatures, the plasmas were very similar. However, the evolving central electron temperature yielded differing sawtooth

characteristics. In discharge A the sawtooth quiescent period was approximately 1s, whilst in discharge B there were many sawtooth cycles per second. These experimental findings suggested that the ICRH power can be set to a level too high to produce sawtooth stabilisation. McClements argued that the hot ions contained in the destabilising toroidal terms dominate the stabilising kinetic effects at higher pressure. A similar process can be seen quite simply for the collisionless thermal ion case of Eq. (2.2). Here the destabilising toroidal effects dominate stabilising kinetic effects at high pressure because of the parabolic dependence in β_p.

Also in 1996, Porcelli *et al* [10] simulated sawtooth cycling in a projected ITER discharge by introducing into a transport code a sawtooth trigger criterion and prescription for sawtooth collapse. The trigger criterion involved a resistive treatment which depends critically on the shear $s = d\log q/d\log r$ at r_1. Porcelli's model showed that the sawteeth can be stabilised transiently by fusion alpha particles in ITER. They went on to point out that their calculations suggested that the sawtooth period could exceed 100 seconds and the mixing radius easily exceed half the minor radius. Subsequently, this raised a great deal of interest concerning the desirability of transient sawtooth suppression in ITER.

Alpha particles, ICRH and NBI heated ions are not the only energetic species that give rise to kinetic effects. With the design and construction of ever larger and hotter tokamaks, the kinetic effects of thermal ions have been increasingly considered. It was mentioned earlier that the Kruskal and Oberman [22] energy principle has been applied to plasmas with energetic thermal ions [23, 24]. The Kruskal and Oberman [22] calculation for thermal ions was also used in Ref. [10]. Fogaccia and Romanelli [44] went further and included the kinetic effects of thermal ions based on the energy principle devised by Antonsen *et al* [6]. They identified a trapped thermal ion instability characterised by $\omega \sim \langle\omega_{mdi}\rangle$. Other authors have made more sophisticated numerical stability calculations. For example, Antonsen and Bondenson [45] included the effects of the perturbed parallel electric field $\delta E_{||}$ - a quantity which does not exist in ideal MHD. It was found that $\delta E_{||}$ had a small stabilising influence. None of these papers, however, included the effects of energetic thermal ions in the singular layer.

Some time earlier Mikhailovskii [46] published a paper reporting a modification to the dispersion relation at the singular layer. It was found that the collisionless effects of thermal ions in the layer, as with the modifications arising from the perturbed toroidal flow [16], enhance the inertia. Unfortunately Mikhailovskii [46] used the simplifying assumption that perturbations in the long-mean-free-path limit are isotropic. A derivation yielding the correction to Mikhailovskii's result is given in Chapter 4. Romanelli *et al* [47] also realised the importance of the kinetic effects of thermal ions in the singular layer. Unlike Mikhailovskii [46], they employed an ordering $\omega \sim \omega_{ti}$, where ω_{ti} is the transit frequency of passing thermal ions. It was argued that this ordering was required in the hybrid plasma (which included both collisionless thermal ions and a collisionless minority population) under consideration.

This thesis attempts to fill some of the gaps highlighted in this literature review. Using the improved calculations for the hot ion kink mode stability of ICRH plasmas [39] a detailed comparison between ideal theory and the JET experiment will be described. Subsequently, some of the limiting factors of Refs. [36, 37, 41] are eliminated.

Moreover, the kinetic description of the internal kink mode is extended to include the effects of an equilibrium electric field. Sheared flows, which can arise as a consequence of the equilibrium electric field, may be significant in many experiments [38]. These effects are included in evaluations for the internal kink mode stability of collisionless plasmas. In addition, unlike previous analysis [23, 24, 44, 45], the kinetic effects of collisionless thermal ions are included consistently in both the external region and the singular layer.

2.2 MHD Stability

The theory of magnetohydrodynamics (MHD) describes quasi neutral plasmas (where the local electron charge is balanced by the ion charge) with scale lengths greater than the Debye length and time scales slow enough that the plasma is collision dominated. The MHD equations are formed by taking velocity moments of the ion and electron kinetic equations. The resulting single fluid description of the plasma is known as MHD. The ions carry the inertia of the plasma and the motion of the more mobile electrons give rise to electromagnetic phenomena. MHD has proved to be a very powerful tool. For example it provides a tractable means of identifying the stability of the plasma against various macroscopic instabilities in the complicated magnetic configurations required for the confinement of plasmas. In the approximation of infinite plasma conductivity the resulting ideal MHD equations are defined as:

$$\begin{aligned}
\frac{d\rho}{dt} + \rho \boldsymbol{\nabla} \cdot \boldsymbol{u} &= 0 \text{ (Conservation of mass)} \\
\rho \frac{d\boldsymbol{u}}{dt} + \boldsymbol{\nabla} P - \boldsymbol{j} \times \boldsymbol{B} &= \mathbf{0} \text{ (Equation of motion)} \\
\frac{d}{dt}\left(P \rho^{-\gamma}\right) &= 0 \text{ (Adiabatic equation of state)} \\
\boldsymbol{E} + \boldsymbol{u} \times \boldsymbol{B} &= \mathbf{0} \text{ (Ideal Ohm's law)} \\
\boldsymbol{\nabla} \cdot \boldsymbol{B} &= 0 \text{ (Conservation of magnetic flux)} \\
\boldsymbol{\nabla} \times \boldsymbol{B} - \mu_0 \boldsymbol{j} &= \mathbf{0} \text{ (Ampère's law)} \\
\frac{\partial \boldsymbol{B}}{\partial t} + \boldsymbol{\nabla} \times \boldsymbol{E} &= \mathbf{0} \text{ (Faraday's law),}
\end{aligned} \tag{2.6}$$

where $\boldsymbol{u}$ is the fluid velocity, ρ is the mass density, P is the plasma pressure, $\boldsymbol{j}$ is the current density, γ is the adiabaticity index and the convective derivative $d/dt = \partial/\partial t + \boldsymbol{u} \cdot \boldsymbol{\nabla}$. The electric and magnetic fields $\boldsymbol{E}$ and $\boldsymbol{B}$ consist of externally applied fields and averaged fields arising from long-range inter-particle interactions.

2.2.1 The Normal Mode Approach

One way of identifying the instabilities that exist in MHD is the normal mode approach. In this approach all the MHD quantities comprise the sum of an equilibrium

component and a perturbation which is small in comparison:

$$\boldsymbol{Q} \rightarrow \boldsymbol{Q} + \boldsymbol{\delta Q}.$$

The perturbations acquire the form $\boldsymbol{\delta Q}(\boldsymbol{x}, t) = \boldsymbol{\delta Q}(\boldsymbol{x}) \exp(-i\omega t)$, representing disturbances that have always existed and do not require initial conditions.

In MHD it is usually assumed that the equilibrium velocity $\boldsymbol{u}$ is negligible. This approximation is valid providing the centrifugal forces associated with a circulating fluid is small. It is convenient to define the perturbed fluid velocity in terms of the fluid displacement $\boldsymbol{\xi}$ such that

$$\boldsymbol{\delta u} = \frac{\partial \boldsymbol{\xi}}{\partial t}.$$

The linearised equation of motion is defined:

$$\rho \frac{\partial^2 \boldsymbol{\xi}}{\partial t^2} = \boldsymbol{\delta F}, \tag{2.7}$$

where

$$\boldsymbol{\delta F} = \boldsymbol{\delta j} \times \boldsymbol{B} + \boldsymbol{j} \times \boldsymbol{\delta B} - \boldsymbol{\nabla} \delta P.$$

The perturbed pressure can be written in terms of the fluid displacement as follows,

$$\delta P = -\gamma P \boldsymbol{\nabla} \cdot \boldsymbol{\xi} - \boldsymbol{\xi} \cdot \boldsymbol{\nabla} P,$$

and the remaining terms, $\boldsymbol{\delta j} \times \boldsymbol{B} + \boldsymbol{j} \times \boldsymbol{\delta B}$, can also be written in terms of $\boldsymbol{B}$ and $\boldsymbol{\xi}$ giving

$$\boldsymbol{\delta F}(\boldsymbol{\xi}) = \boldsymbol{\nabla}(\gamma P \boldsymbol{\nabla} \cdot \boldsymbol{\xi} + \boldsymbol{\xi} \cdot \boldsymbol{\nabla} P) + \frac{1}{\mu_0}[(\boldsymbol{\nabla} \times \boldsymbol{\nabla} \times (\boldsymbol{\xi} \times \boldsymbol{B})) \times \boldsymbol{B} + (\boldsymbol{\nabla} \times \boldsymbol{B}) \times (\boldsymbol{\nabla} \times (\boldsymbol{\xi} \times \boldsymbol{B}))].$$

Hence the normal mode approach represents an eigenvalue problem problem in ω^2 with solutions conforming to,

$$-\omega^2 \rho \boldsymbol{\xi} = \boldsymbol{\delta F}(\boldsymbol{\xi}),$$

with $\boldsymbol{\xi}$ no longer an explicit function of time.

The force operator possess an important property which greatly aids the analysis of linearised MHD stability. In particular it can be shown that for two independent displacement vectors $\boldsymbol{\xi_1}$ and $\boldsymbol{\xi_2}$ the following relation holds

$$\int \boldsymbol{\xi_1} \cdot \boldsymbol{\delta F}(\boldsymbol{\xi_2}) d^3x = \int \boldsymbol{\xi_2} \cdot \boldsymbol{\delta F}(\boldsymbol{\xi_1}) d^3x, \tag{2.8}$$

where the integration is performed over all space. Thus, $\boldsymbol{\delta F}$ is self-adjoint [5].

Using the self-adjoint property of the force operator it is straightforward to show that ω^2 is real. The possibilities are
1) Two stationary modes, with one growing and the other decaying (i.e. $\omega^2 < 0$)
2) Two modes neither growing or decaying but both propagate with equal speeds and in the opposite sense (i.e. $\omega^2 > 0$).

2.2.2 The Energy Principle

The fact that stability boundaries occur when ω^2 crosses zero ultimately leads to an elegant and efficient means for testing MHD stability known as the energy principle. The formulation is derived by forming the scalar product of Eq. (2.7) with $\boldsymbol{\xi}^*$ and integrating over all space giving

$$\delta K(\boldsymbol{\xi}, \boldsymbol{\xi}^*) + \delta W(\boldsymbol{\xi}, \boldsymbol{\xi}^*) = 0, \tag{2.9}$$

where the self-adjoint property of Eq. (2.8) has been used for the definitions of

$$\begin{aligned} \delta K(\boldsymbol{\xi}, \boldsymbol{\xi}^*) &= -\frac{1}{2}\omega^2 \int \rho \left|\boldsymbol{\xi}^2\right| \, d^3x \\ \delta W(\boldsymbol{\xi}, \boldsymbol{\xi}^*) &= -\frac{1}{2} \int \boldsymbol{\xi}^* \cdot \boldsymbol{\delta F}(\boldsymbol{\xi}) \, d^3x. \end{aligned} \tag{2.10}$$

Hence from Eq. (2.9) it is clear that the energy due to the mode is conserved.

The energy principle [5, 48] states that the eigenfunction $\boldsymbol{\xi}$ is obtained by minimising $\delta K(\boldsymbol{\xi}, \boldsymbol{\xi}^*) + \delta W(\boldsymbol{\xi}, \boldsymbol{\xi}^*)$ with respect to $\boldsymbol{\xi}$ and keeping ω fixed. Subsequently, from Eq. (2.9),

$$\omega^2 = \frac{2\delta W}{\int \rho \left|\boldsymbol{\xi}^2\right| \, d^3x} \tag{2.11}$$

determines the growth rate. This procedure is equivalent to obtaining a normal mode solution of Eq. (2.7).

The energy principle also renders a simplified analysis. Equation (2.11) indicates that the stability transition occurs for $\delta W = 0$, i.e. a mode is stable for $\delta W > 0$ and unstable for $\delta W < 0$. Hence, if one is interested only in whether the mode is stable, and the exact growth rate is not required, only the sign of δW needs to be calculated. A proof exists [5] showing that the sign of δW is obtained correctly by minimising only δW, rather than $\delta K + \delta W$, with respect to $\boldsymbol{\xi}$. This allows for a tractable means of calculating stability boundaries and intuitive comparisons between competing sources of stability.

Care must be taken if one uses the simplified energy principle to infer growth rates. In the case of the internal kink mode, the minimisation of only δW and the subsequent implementation of Eq. (2.11) leads to large errors in ω. However, if one minimises $\delta K + \delta W$, it is found that $\boldsymbol{\xi}$ depends on ω in such a way that $\int \rho \left|\boldsymbol{\xi}^2\right| \, d^3x \propto 1/\omega$. Therefore, even when δW is close to its stability boundary, one must minimise $\delta K + \delta W$ if accurate growth rates are required.

2.2.3 Intuitive form of δW

The potential energy can be written in a convenient form [49] enabling various competing energy sources in δW to be easily identified. Assuming that the plasma is bounded by a perfectly conducting wall it can shown that:

$$\delta W(\boldsymbol{\xi}, \boldsymbol{\xi}^*) = \delta W_\perp(\boldsymbol{\xi}_\perp, \boldsymbol{\xi}_\perp^*) + \overline{\delta W}(\boldsymbol{\xi}, \boldsymbol{\xi}^*),$$

with,

$$\delta W_\perp(\boldsymbol{\xi}_\perp, \boldsymbol{\xi}_\perp^*) = \frac{1}{2}\int d^3x \left(\frac{\delta B_\perp^2}{\mu_0} + \frac{B^2}{\mu_0}(\boldsymbol{\nabla}\cdot\boldsymbol{\xi}_\perp + 2\boldsymbol{\xi}_\perp\cdot\boldsymbol{\kappa})^2 \right.$$
$$\left. -2(\boldsymbol{\xi}_\perp\cdot\boldsymbol{\nabla}P)(\boldsymbol{\kappa}\cdot\boldsymbol{\xi}_\perp^*) - j_\parallel(\boldsymbol{\xi}_\perp^*\times\hat{\boldsymbol{e}}_\parallel)\cdot\boldsymbol{\delta B}_\perp \right) \quad (2.12)$$

$$\overline{\delta W}(\boldsymbol{\xi}, \boldsymbol{\xi}^*) = \frac{1}{2}\int d^3x\, \gamma P(\boldsymbol{\nabla}\cdot\boldsymbol{\xi})^2, \quad (2.13)$$

where $j_\parallel$ is the parallel current density,

$$\boldsymbol{\delta B} = \boldsymbol{\nabla}\times(\boldsymbol{\xi}_\perp\times\boldsymbol{B}), \quad (2.14)$$

$\hat{\mathbf{e}}_\parallel = \boldsymbol{B}/B$, the magnetic field line curvature vector

$$\boldsymbol{\kappa} = \partial\hat{\boldsymbol{e}}_\parallel/\partial l \quad (2.15)$$

and l is a length parallel to the magnetic field such that $\partial/\partial l = \hat{\boldsymbol{e}}_\parallel\cdot\boldsymbol{\nabla}$. Each of the terms in Eq. (2.12) has a simple physical interpretation. The first term in $\delta W_\perp$ is always stabilising and is the magnetic energy in the Alfvén wave associated with field line bending. The second term is also stabilising and corresponds to the energy necessary to compress the magnetic field and describes the major potential energy contribution to magnetosonic waves. The third term, proportional to the pressure gradient, is the potential energy for the ballooning instability. It is destabilising if $\boldsymbol{\nabla}P$ and $\boldsymbol{\kappa}$ are parallel (unfavourable curvature). The fourth term is the free energy arising from the current and is responsible for external kink instabilities. The internal kink mode involves a complicated combination of the third and fourth term; that is, both current and pressure play a role. $\overline{\delta W}$ is the energy required to compress the plasma. It is stabilising and corresponds to the major energy source in sound waves.

2.2.4 Incompressibility

Before using the energy principle it is essential to attempt a reduction in the complexity of the analysis. This section demonstrates that under certain conditions, the dimensions of the system can be reduced from three to two.

Equation (2.12) shows that $\delta W_\perp$ is independent of $\boldsymbol{\xi}_\parallel$. This means that δW can be minimised with respect to $\boldsymbol{\xi}_\parallel$ by only considering $\overline{\delta W}$. It is clear that $\overline{\delta W}$ is positive definite and minimises to zero when $\boldsymbol{\nabla}\cdot\boldsymbol{\xi} = 0$. This requires that the parallel flow satisfies

$$B\frac{\partial}{\partial l}\left(\frac{\boldsymbol{\xi}_\parallel}{B}\right) = -\boldsymbol{\nabla}\cdot\boldsymbol{\xi}_\perp. \quad (2.16)$$

Hence, the most unstable modes that exist in the vicinity of the stability boundary are incompressible. One should note that the parallel flow does not satisfy Eq. (2.16) far from the stability boundary, i.e. normal modes are not incompressible when their rate of growth is large. However, in this thesis, the growth rates are small and Eq. (2.16) is appropriate.

2.2.5 Collisionless MHD

The implementation of ideal MHD requires that the plasma is collision dominated. This is not usually the case in fusion plasmas. For example, large tokamaks, like JET and TFTR, often run at high temperatures where neither the thermal ions nor the energetic minority species are collisional. Models other than ideal MHD are used to analyse the stability of collisionless plasmas.

The theory used in much of the work in this thesis involves drift kinetic theory. Here, the perpendicular motion is fluid like (i.e. involves $\boldsymbol{\xi}_\perp$), while a one dimensional kinetic equation governs the behaviour parallel to the field. The model also allows for pressure anisotropy and the effects of wave - particle resonances. Problems involving drift kinetic theory are more difficult to solve than ideal MHD because of inherent wave - particle resonances and the complexities associated with the parallel kinetic motion.

The collisionless MHD model represents a simplifying limit of drift kinetic theory. In this model the pressure is assumed isotropic, the time scales disallow wave-particle interaction and most crucially the kinetic equation for the parallel flow is replaced by the assumption $\boldsymbol{\nabla}\cdot\boldsymbol{\xi}=0$, i.e. perturbations analysed in the collisionless MHD model are incompressible. The ideal MHD equations are altered as follows:

$$\begin{aligned}
\frac{d\rho}{dt}+\rho\boldsymbol{\nabla}\cdot\boldsymbol{u}=0 \quad &\rightarrow \quad \frac{d\rho}{dt}=0 \\
\frac{d}{dt}\left(P\rho^{-\gamma}\right)=0 \quad &\rightarrow \quad \frac{dP}{dt}=0 \\
\rho\frac{d\boldsymbol{u}}{dt}+\boldsymbol{\nabla}P-\boldsymbol{j}\times\boldsymbol{B}=0 \quad &\rightarrow \quad \rho\frac{d\boldsymbol{u}_\perp}{dt}+\boldsymbol{\nabla}_\perp P-\boldsymbol{j}\times\boldsymbol{B}=0.
\end{aligned} \tag{2.17}$$

Since parallel flow does not appear in Eq. (2.17), the collisionless MHD energy principle now corresponds to the minimisation of

$$\delta K_\perp(\boldsymbol{\xi}_\perp,\boldsymbol{\xi}_\perp^*)+\delta W_\perp(\boldsymbol{\xi}_\perp,\boldsymbol{\xi}_\perp^*) \tag{2.18}$$

with respect to $\boldsymbol{\xi}_\perp$ [50], where $\delta W_\perp(\boldsymbol{\xi}_\perp,\boldsymbol{\xi}_\perp^*)$ is the same as that of Eq. (2.12) and

$$\delta K_\perp(\boldsymbol{\xi}_\perp,\boldsymbol{\xi}_\perp^*)=-\frac{1}{2}\omega^2\int\rho\left|\boldsymbol{\xi}_\perp^2\right|\,d^3x. \tag{2.19}$$

Consequently, both collisionless MHD and ideal MHD predict exactly the same stability boundaries but different growth rates. The effects of collisionless thermal ions on the internal kink mode are considered in detail later in this thesis. In particular, comparisons are made between the subsequent energy principles of drift kinetic theory and those of the collisionless and ideal MHD models.

2.3 Large Aspect Ratio Equilibria

For axisymmetric equilibria, that is equilibria independent of the toroidal angle ϕ, the magnetic field lines lie in nested toroidal flux surfaces as illustrated in Fig. 2.2. The

basic condition for equilibrium is that the force on the plasma is zero at all points. This requires that the magnetic force balances the force due to the plasma pressure,

$$\boldsymbol{j} \times \boldsymbol{B} = \boldsymbol{\nabla} P. \tag{2.20}$$

It is clear from this equation that $\boldsymbol{B} \cdot \boldsymbol{\nabla} P = 0$. Thus pressure gradients do not exist along field lines and magnetic flux surfaces are surfaces of constant pressure.

2.3.1 Low beta plasmas

The efficiency of the confinement of plasma pressure by the magnetic field is represented in a simple way by the ratio

$$\beta = \frac{P}{B^2/2\mu_0}.$$

There are several alternative expressions of this type, some arising from varying choices of definition and others from the need to quantify different equilibrium properties. One of these is the poloidal beta measured at r_1 as defined in Eq. (2.1).

The pressure and magnetic field are directly related through the pressure balance equation. This is obtained by considering the equilibrium force balance of Eq. (2.20) and Ampère's law. As will be seen later, when considering plasmas of large aspect ratio (which typically conform to $R_0/a \gtrsim 2.5$) the local inverse aspect ratio $\varepsilon = r/R_0$ is regularly used as a formal expansion parameter. The leading order terms of the pressure balance equation give:

$$\frac{dP}{dr} + \frac{1}{2\mu_0}\frac{d}{dr}\left(B_\phi^2\right) + \frac{B_\theta}{\mu_0 r}\frac{d}{dr}(rB_\theta) = 0.$$

Tokamak equilibria take a comparatively simple form for low β, large aspect ratio plasmas. The following scalings in terms of the local inverse aspect ratio $\varepsilon = r/R_0$ are used throughout this thesis:

$$\begin{aligned}
B_\phi(r,\theta) &= B_0 \frac{R_0}{R(r,\theta)}\left(1 + O(\varepsilon^2)\right) \\
B_\theta &\sim \varepsilon B_\phi \\
q(r) &= \frac{\varepsilon B_0}{B_\theta(r)}\left(1 + O(\varepsilon)\right) \sim 1 \\
\beta &\sim \varepsilon^2 \\
\beta_p &\sim 1 \\
j_\phi &\approx \frac{1}{\mu_0 r}\frac{d}{dr}(rB_\theta) \\
j_\theta &\sim \varepsilon j_\phi.
\end{aligned} \tag{2.21}$$

Hence the pressure balance equation gives

$$\frac{dP}{dr} \sim -\frac{B_\phi}{\mu_0}\frac{dB_\phi}{dr}.$$

The low beta ordering allows for a simplified description of the equilibrium magnetic field structure. In such instances it is convenient to write $\boldsymbol{j} \times \boldsymbol{B} = 0$. Using this together with Ampère's law gives $B\boldsymbol{\nabla}B = (\boldsymbol{B} \cdot \boldsymbol{\nabla})\boldsymbol{B}$. It is now easy to show that

$$\frac{\boldsymbol{\xi}_\perp \cdot \boldsymbol{\nabla} B}{B} = \boldsymbol{\xi}_\perp \cdot \boldsymbol{\kappa}. \tag{2.22}$$

Equation (2.22) is very useful in Chapter 3. It serves to greatly simplify the kinetic modifications of the internal kink mode.

2.3.2 The Shafranov Shift

One can think of a toroidal flux surface as a bent cylindrical plasma column. The resulting toroidal curvature has important consequences on the equilibrium properties of the plasma. The largest of these is a shift in the major radius of nested flux surfaces. The shift, illustrated in Fig. 2.5 is known as the Shafranov shift, $\Delta(r)$, and essentially arises as a consequence of the hoop force and the tyre tube force [50].

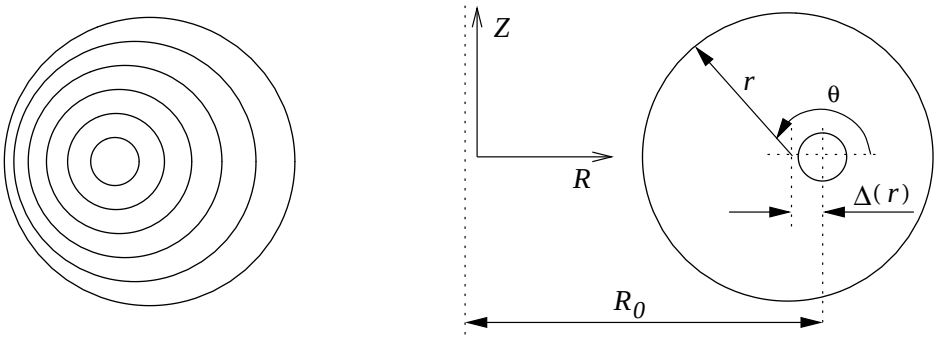

Figure 2.5: Showing nested circular flux surfaces displaced by a distance $\Delta(r)$ from the magnetic axis which is located at distance R_0 from the major axis.

The hoop force emerges because the magnetic field strength is stronger on the inboard side of the torus ($\theta = \pi$) than the outboard ($\theta = 0$) and the tyre tube force because the plasma pressure acts on a smaller surface on the inboard side of the torus than the outboard. These forces combine to produce a shift which is monotonically increasing with r. A unique flux surface is defined by $r =$ constant with $0 \leq \theta \leq 2\pi$, or in terms of the cylindrical system,

$$\begin{aligned} Z &= r \sin\theta \\ R &= R_0 - \Delta(r) + r\cos\theta. \end{aligned}$$

A solution of the Grad-Shafranov equilibrium equation [51] yields

$$\Delta'(r_1) = \varepsilon_1 \left[\beta_p + \sigma + \frac{1}{4}\right], \tag{2.23}$$

where β_p is defined in Eq. (2.1), $\varepsilon_1 = r_1/R_0$ is the inverse aspect ratio at the $q = 1$ rational surface and

$$\sigma = \frac{1}{r_1^4}\int_0^{r_1} r^3 \left(\frac{1}{q(r)^2} - 1\right) dr. \tag{2.24}$$

Equation (2.23) demonstrates that the poloidal beta scales linearly with the gradient of the Shafranov shift. If one now considers Bussac's [15] approximate stability condition, given by Eq. (2.1), it is now clear that the stability of the internal kink mode depends strongly on Δ'. This confirms the earlier statement that the stability of the internal kink mode depends strongly on toroidal effects.

2.3.3 Shaping of Flux Surfaces

The flux surfaces of many tokamak plasmas are not only displaced by the Shafranov shift but are also non-circular. In general R and Z may be expressed respectively as Fourier cosine and sine series in the poloidal angle θ. Truncating each series at the second harmonic:

$$\begin{aligned} Z(r,\theta) &= r\left[(1 + L(r))\sin\theta - T(r)\sin 2\theta\right] \\ R(r,\theta) &= R_0 - \Delta(r) + r\left[(1 - L(r))\cos\theta + T(r)\cos 2\theta\right], \end{aligned} \tag{2.25}$$

where $L(r)$ and $T(r)$ are profiles representing the elongation and triangularity respectively. The effects of elongation and triangularity on flux surface cross sections is illustrated in Fig. 2.6. If large enough, the distortions can affect the MHD stability of the internal kink mode [43]. The effects of triangularity and elongation are considered when interpreting JET sawteeth data in Chapter 5.

Figure 2.6: Showing typical elongated, triangular and Shafranov shifted nested flux surfaces.

2.4 The Internal Kink Mode

In an axisymmetric torus, a perturbation may be described by a Fourier decomposition in poloidal harmonics as

$$\boldsymbol{\xi}(r,\theta,\phi) = \sum_m \boldsymbol{\xi}^{(m)}(r) e^{i(m\theta - n\phi - \omega t)}$$

by virtue of the periodicity in the poloidal and toroidal directions. Since the equilibrium magnetic field strength $B = B_0(1 - \varepsilon\cos\theta)$ is a function of θ, a coupling in the different poloidal harmonics arises in $\boldsymbol{\xi}$.

For the study of the internal kink mode, the principal mode numbers are $m = n = 1$. However, the effect of finite Shafranov shift (i.e. finite toroidal effects) is to couple the principal mode $\boldsymbol{\xi}^{(1)}$ to $\boldsymbol{\xi}^{(0)}$ and $\boldsymbol{\xi}^{(2)}$.

The following sections discuss the minimisation of δW with respect to $\boldsymbol{\xi}$. To aid the analysis the eigenvector is written as follows:

$$\boldsymbol{\xi} = \boldsymbol{\xi}_0 + \boldsymbol{\xi}_1 + \boldsymbol{\xi}_2,$$

where the subscript denotes the aspect ratio ordering of the term, e.g. $\boldsymbol{\xi}_2/\boldsymbol{\xi}_0 \sim O(\varepsilon^2)$. Subsequently, it is found that

$$\delta W = \delta W_0 + \delta W_2 + \delta W_4.$$

δW_0, δW_2 and δW_4 are minimised with respect to $\boldsymbol{\xi}_0$, $\boldsymbol{\xi}_1$ and $\boldsymbol{\xi}_2$ as shown in the following sections.

2.4.1 Minimisation of δW_0

In both δW_0 and δW_2 it is appropriate to write,

$$\begin{aligned} \boldsymbol{\xi}_\perp &= \xi_r \hat{\boldsymbol{e}}_r + \xi_\theta \hat{\boldsymbol{e}}_\theta \\ \boldsymbol{\delta B}_\perp &= \delta B_r \hat{\boldsymbol{e}}_r + \delta B_\theta \hat{\boldsymbol{e}}_\theta \\ j_\parallel &= j_\phi. \end{aligned}$$

In the next section it is shown that $\delta B_{\perp 0} \sim \varepsilon B_0 \boldsymbol{\nabla}\cdot\boldsymbol{\xi}_{\perp 0}$. The parallel curvature vector $\boldsymbol{\kappa}$ is also not a leading order effect i.e. $\boldsymbol{\xi}_{\perp 0}\cdot\boldsymbol{\kappa}/\boldsymbol{\nabla}\cdot\boldsymbol{\xi}_{\perp 0} \sim \varepsilon$. Hence, from Eq. (2.12) it is clear that,

$$\delta W_0 = \frac{1}{2}\int d^3x \frac{B^2}{\mu_0}\left(\boldsymbol{\nabla}\cdot\boldsymbol{\xi}_\perp\right)^2. \tag{2.26}$$

Since this term is positive definite the minimisation of Eq. (2.26) corresponds to $\boldsymbol{\nabla}\cdot\boldsymbol{\xi}_\perp = 0$, which gives $\delta W_0 = 0$. The leading order displacement does not allow poloidal coupling; hence $\boldsymbol{\xi}_0 = \boldsymbol{\xi}_0(r)e^{i(m\theta - n\phi - \omega t)}$, which gives

$$\xi_{\theta 0} = \frac{i}{m}\frac{\partial}{\partial r}\left(r\xi_{r0}\right). \tag{2.27}$$

Since the minimised zeroth order potential energy vanishes, the next order must be considered.

2.4.2 Minimisation of δW_2

All except the third term in Eq. (2.12) feature in δW_2. This term is neglected because the ordering of $\beta \sim O(\varepsilon^2)$ means that terms involving the equilibrium pressure first appear in δW_4. Referring to Eq. (2.12) it is now clear that

$$\delta W_2 = \frac{1}{2}\int d^3x \left(\frac{\delta B_{\perp 0}^2}{\mu_0} + \frac{B^2}{\mu_0}\left(\boldsymbol{\nabla}\cdot\boldsymbol{\xi}_{\perp 1} + 2\boldsymbol{\xi}_{\perp 0}\cdot\boldsymbol{\kappa}\right)^2 - j_{\|}(\boldsymbol{\xi}^*_{\perp 0}\times\hat{\boldsymbol{e}}_{\|})\cdot\boldsymbol{\delta B}_{\perp 0}\right). \quad (2.28)$$

the second term is minimised to zero by a constraint on $\boldsymbol{\xi}_{\perp 1}$ such that,

$$\boldsymbol{\nabla}\cdot\boldsymbol{\xi}_{\perp 1} + 2\boldsymbol{\xi}_{\perp 0}\cdot\boldsymbol{\kappa} = 0. \quad (2.29)$$

Using Eq. (2.22) with Eq. (2.29) gives

$$\frac{(\boldsymbol{\xi}_{\perp 0}\cdot\boldsymbol{\nabla})B}{B} = \boldsymbol{\xi}_{\perp 0}\cdot\boldsymbol{\kappa} = -\frac{1}{2}\boldsymbol{\nabla}\cdot\boldsymbol{\xi}_{\perp 1}. \quad (2.30)$$

Many steps in calculations henceforth interchange between the the expressions contained in Eq. (2.30). An additional important consequence of Eqs. (2.22) and (2.29) should be mentioned. The parallel component of Eq. (2.14) is $\delta B_{\|} = -B\boldsymbol{\nabla}\cdot\boldsymbol{\xi}_{\perp} - (\boldsymbol{\xi}_{\perp}\cdot\boldsymbol{\nabla})B - B\boldsymbol{\xi}_{\perp}\cdot\boldsymbol{\kappa}$. Hence, from Eq. (2.30), it is clear that $\delta B_{\|} = 0$. That is, in a low beta plasma, internal kink oscillations do not support parallel magnetic compression. This result will be used in the kinetic description of the plasma where it will be seen that $\delta B_{\|} = 0$ serves to greatly simplify the analysis. In addition, Eq. (2.29) is also used in the δW_4 calculation [15]. It is shown that $\boldsymbol{\xi}_{\perp 1}$ has ± 1 sidebands so that $\partial\boldsymbol{\xi}_{\perp 1}/\partial\theta \neq im\boldsymbol{\xi}_{\perp 1}$.

To minimise δW_2, both $\delta B_{\theta 0}$ and δB_{r0} are written in terms of ξ_{r0}. The perturbed field is defined in terms of the eigenfunction using Eq. (2.14). Recalling that $\boldsymbol{\nabla}\cdot\boldsymbol{\xi}_{\perp 0} = 0$ and using Eq. (2.21) for q, together with Eq. (2.27) and $\boldsymbol{\nabla} = \hat{\boldsymbol{e}}_r\partial/\partial r + (\hat{\boldsymbol{e}}_\theta/r)\partial/\partial\theta + (\hat{\boldsymbol{e}}_\phi/R)\partial/\partial\phi$ gives,

$$\begin{aligned}
\delta B_{r0} &= \frac{imB_0}{R_0}\left(\frac{n}{m} - \frac{1}{q}\right)\xi_{r0} \\
\delta B_{\theta 0} &= \frac{B_0}{R_0}\frac{\partial}{\partial r}\left[\left(\frac{n}{m} - \frac{1}{q}\right) r\xi_{r0}\right].
\end{aligned}$$

In addition, from Ampère's law:

$$\mu_0 j_\phi = \frac{1}{r}\frac{d}{dr}(rB_\theta) \approx \frac{B_0}{R_0}\frac{1}{r}\frac{\partial}{\partial r}\left(\frac{r^2}{q}\right).$$

Hence, using $\int d^3x = R_0\int_0^{2\pi} d\phi \int_0^{2\pi} d\theta \int_0^a r\,dr$, and integrating by parts to remove terms involving $\xi_{\perp 0} d\xi_{\perp 0}/dr$, Eq. (2.28) becomes,

$$\delta W_2 = \frac{2\pi^2 B_0^2}{\mu_0 R_0}\int_0^a dr\, r\left[\left(r\frac{d\xi_{r0}}{dr}\right)^2 + \left(m^2 - 1\right)^2\xi_{r0}^2\right]\left(\frac{n}{m} - \frac{1}{q}\right)^2 \quad (2.31)$$

where it is assumed that the plasma is bounded by a perfectly conducting wall at $r = a$. Equation (2.31) shows that to second order in the inverse aspect ratio, ideal MHD does not allow unstable internal modes for $\beta \sim O(\varepsilon^2)$ since all the terms are positive definite.

It is now appropriate to minimise Eq. (2.31) with respect to ξ_{r0} for the internal kink mode. Setting $m = 1$ cancels part of the field line stabilising term and δW_2 becomes:

$$\delta W_2 = \frac{2\pi^2 B_0^2}{\mu_0 R_0} \int_0^a dr\, r^3 \left(\frac{d\xi_{r0}}{dr}\right)^2 \left(1 - \frac{1}{q}\right)^2 . \tag{2.32}$$

It can be seen that the integrand reduces to zero for $q(r_1) = 1$. At this rational surface ($r = r_1$) the poloidal curvature of magnetic field lines matches the poloidal mode number $m = 1$. Moreover, a constant ξ_{r0} reduces the integrand to zero for all r. However, Eq. (2.32) is only valid for internal modes having $\xi_{a0} = 0$. Thus a finite constant ξ_{r0} is not allowed. Fig. 2.7 shows a form for ξ_{r0} which is wholly internal and which satisfies the boundary conditions and minimises δW_2.

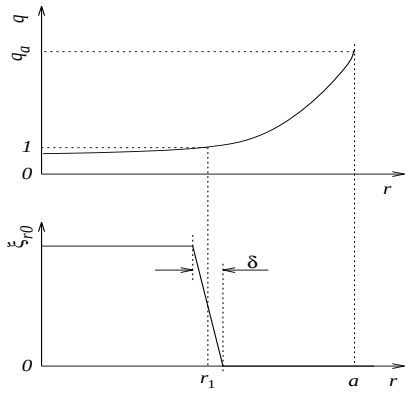

Figure 2.7: The radial dependence of ξ_{r0} with layer width δ. The function approaches a top hat function for $\delta \to 0$. Also shown is the corresponding q-profile.

The inevitable distortion of ξ_{r0} is taken up at r_1. At this surface the perturbation has the same helicity as the magnetic field and as a consequence the energy change can be made arbitrarily small by localisation of $d\xi_{r0}/dr$. This can be shown by calculating the contribution δW_2 receives from the layer region, which is defined approximately by $r_1 - \delta/2 < r < r_1 + \delta/2$. By taking variations of δW_2 with respect to ξ_{r0} within this region, $\delta W_2 \to 0$ for $\delta \to 0$. This implies that $\partial \xi_{r0}/\partial r$ is singular in the vicinity of the $q = 1$ rational surface, and from Eq. (2.27), the poloidal displacement is also singular. A modification of the minimisation procedure is outlined in detail later when an analysis for the growth rate of the internal kink mode is presented. It is found that the discontinuity at r_1 is resolved by including the inertia, δK, in the minimisation. Both δK and δW_2 pick up finite contributions from a layer of finite width δ, such that they are formally the same order as the δW_4 calculation below.

2.4.3 Minimisation of δW_4

Both δW_0 and δW_2 have been minimised to zero. That is, the internal kink mode is marginally stable to order ε^2. The stability of the kink mode therefore depends on the fourth order correction, i.e. since both δW_0 and δW_2 have been minimised to zero one must consider fourth order terms. In calculating δW_4 the results for $\boldsymbol{\xi}_{\perp 0}$ and $\boldsymbol{\xi}_{\perp 1}$ given in the previous two sections must be used. The remaining component of $\boldsymbol{\xi}_{\perp 1}$ together with $\boldsymbol{\xi}_{\perp 2}$ are still to be identified.

A cylindrical calculation accurate to fourth order in the aspect ratio was first published by Rosenbluth [14]. However, for the all important $n = 1$ case Bussac *et al* [15] demonstrated that the fourth order cylindrical calculation is irrelevant. By including the toroidal effects of Shafranov shifted circular flux surfaces, Bussac et al [15] showed that the fourth order solution has the form

$$\delta\hat{W}_4 = \left(1 - \frac{1}{n^2}\right)\delta\hat{W}_4^C + \delta\hat{W}_4^T, \tag{2.33}$$

where $\delta\hat{W} = \delta W/(6\pi^2 R_0 B_0^2 \xi_0^2 \varepsilon_1^4/\mu_0)$, $\delta\hat{W}_4^C$ is the cylindrical potential energy [14] and $\delta\hat{W}_4^T$ is the toroidal contribution.

It was shown in the last section that the poloidal curvature matches the poloidal mode number $m = 1$ in the vicinity of r_1, and as a consequence the stability associated with field line bending is lost. A cylindrical calculation cannot, however, correctly deal with toroidal curvature. By including toroidal effects Bussac [15] demonstrated that a nullifying resonance also exists between the toroidal curvature at $q = 1$ and the toroidal mode number $n = 1$. This effect is manifest in Eq. (2.33) where it is shown that the cylindrical term of Ref. [14] does not contribute to $\delta\hat{W}_4$. As a result the stability of the ideal $m = n = 1$ internal kink mode depends purely on toroidal effects even in the limit of infinite aspect ratio.

Since the Shafranov shift is a linear function of β_p, as shown in Eq. (2.23), it is not surprising that the stability of the internal kink mode depends strongly on the pressure. As found by Bussac *et al*, the toroidal coupling of the $m = 2$ mode produces a stabilising effect, and the mode is destabilised only for β_p above a threshold value. For a quadratic q profile δW_4^T is given by [15]:

$$\delta\hat{W}_4^T = (1 - q_0)\left((\beta_p^c)^2 - \beta_p^2\right), \tag{2.34}$$

with $\beta_p^c = \sqrt{13/144} \approx 0.3$. For $\beta_p \gtrsim \beta_p^c$, Eq. (2.34) predicts that the internal kink mode is unstable. To obtain β_p^c in plasmas with more realistic q profiles one must consult the general calculation [15], which can be found in Appendix A of this thesis. Using more realistic q profiles in the general calculation, the critical poloidal beta typically lies in the range $0.1 < \beta_p^c < 0.2$. Also, modified is the dependence of $\delta\hat{W}_4^T$ on β_p.

The effects of flux surface shaping also arise at $O(\varepsilon^4)$. The flux surfaces are described by the expansions of Eq. (2.25) and the resulting potential energy $\delta\hat{W}_4^S$ was first calculated by Edery *et al* [43] and also is defined in Appendix A. It was

shown that the elongation of flux surfaces is destabilising to the internal kink mode while triangular distortions are stabilising. The calculations of both $\delta\hat{W}_4^T$ and $\delta\hat{W}_4^S$ were confirmed collectively in a more detailed report by Connor and Hastie [52].

2.4.4 The Parallel Flow at the Rational Surface

When Rosenbluth [14] and Bussac [15] made growth rate calculations they wrongly assumed that the parallel flow could be neglected from the inertia. They were misled to believe that perturbations in the parallel direction are always an order smaller in the inverse aspect ratio than the perpendicular perturbations. The singular layer introduces a special case where $\xi_{||}/\xi_{\perp 0} \sim O(1)$. This special case is crucial to the internal kink mode because the inertia is dominated by the singular nature of the plasma flow at r_1. This section includes an analysis for the magnitude of $\xi_{||}$ located at a general rational surface defined by $q = m/n$.

If the growth rate is not very large, then, as shown Section 2.2.4, the ideal MHD perturbation is incompressible. It therefore follows that the parallel displacement is given by Eq. (2.16), which coupled with Eq. (2.27) gives

$$B\frac{\partial}{\partial l}\left(\frac{\boldsymbol{\xi}_{||}}{B}\right) = -\boldsymbol{\nabla}\cdot\boldsymbol{\xi}_{\perp_1}.$$

Now, $\partial/\partial l = \hat{\boldsymbol{e}}_{||}\cdot\boldsymbol{\nabla} = (\hat{\boldsymbol{e}}_{||}\cdot\boldsymbol{\nabla}\theta)\partial/\partial\theta + (\hat{\boldsymbol{e}}_{||}\cdot\boldsymbol{\nabla}\phi)\partial/\partial\phi$, where $\hat{\boldsymbol{e}}_{||} = \boldsymbol{B}/B$. Hence, since $\nabla = \hat{\boldsymbol{e}}_r\,\partial/\partial r + (\hat{\boldsymbol{e}}_\theta/r)\partial/\partial\theta + (\hat{\boldsymbol{e}}_\phi/R)\partial/\partial\phi$ and $q = rB/RB_\theta$, then

$$\frac{\partial}{\partial l} = \frac{1}{R}\left[\frac{1}{q}\frac{\partial}{\partial\theta} + \frac{\partial}{\partial\phi}\right]. \tag{2.35}$$

Using Eq. (2.30) and noting that the variation of the field strength along the field line is small compared to that of $\xi_{||}$ approximately gives

$$\frac{1}{R_0 q}\left[\frac{\partial}{\partial\theta} - inq\right]\xi_{||} = \frac{2(\boldsymbol{\xi}_{\perp_0}\cdot\boldsymbol{\nabla})B}{B_0}, \tag{2.36}$$

where $\partial\xi_{||}/\partial\phi = -in\xi_{||}$. The corresponding derivative in the poloidal angle remains because it is suspected that $\xi_{||}$ contains poloidal harmonics so that $\partial\xi_{||}/\partial\theta \neq im\partial\xi_{||}\partial\theta$.

Close to a singular layer, $\partial\xi_{r0}/\partial r >> \xi_{r0}/r$. Hence, from Eq. (2.27), $\xi_{\theta 0} >> \xi_{r0}$. Also upon substitution of $B = B_0(1 - \varepsilon\cos\theta)$, Eq. (2.36) now becomes

$$\left[\frac{\partial}{\partial\theta} - im\right]\xi_{||} = 2\,\xi_{\theta 0}\,q\sin\theta, \tag{2.37}$$

where the equation for the rational surface $m = nq$ has been substituted. The solution of Eq. (2.37) is

$$\xi_{||} = \xi_{||}^{(m+1)} + \xi_{||}^{(m-1)},$$

where

$$\begin{aligned}\xi_{||}^{(m+1)} &= -\xi_{\theta 0}(\theta)\,q\,e^{i\theta}\\ \xi_{||}^{(m-1)} &= -\xi_{\theta 0}(\theta)\,q\,e^{-i\theta},\end{aligned}$$

or

$$\xi_{||} = -2\,\xi_{\theta 0}(\theta)\,q\cos\theta. \tag{2.38}$$

Hence, $\xi_{||}$ comprises poloidal harmonics 0 and 2 for a principal mode $m = 1$.

Equation (2.38) demonstrates that close to the rational surface r_1 the parallel flow is the same order of magnitude as the leading order poloidal flow. The importance of the parallel flow is realised in the next section where an analysis for the growth rate is described.

2.4.5 Internal Kink Growth Rate

Thus far in this chapter the stabilisation of the internal kink has been assessed by minimising δW with respect to $\boldsymbol{\xi}$. This however has only provided information concerning the stability threshold of the internal kink mode and the structure of the eigenfunction $\boldsymbol{\xi}$. By contrast, calculations of the growth rate must necessarily contain the inertia in the minimisation procedure.

The minimisation of Eq. (2.32) produces singular poloidal and toroidal displacements at r_1. If one considers a regime where the growth rate, or rotation frequency, is finite, then ostensibly the leading order poloidal and toroidal velocities are also singular (since $\delta u_{\theta 0} = -\omega i \xi_{\theta 0}$ and $\delta u_\phi = -i\omega\xi_\phi$). However this is not so and it will be shown in this section that finite inertia removes the singular behaviour located at r_1.

For the growth rates of interest in this thesis, the characteristics of the plasma close to r_1 are very different to those at locations far from r_1. Although the poloidal and toroidal flows close to r_1 are not singular for $\omega \neq 0$, they are nevertheless much larger than those far from r_1, and as a consequence the inertia is dominated by the plasma close to r_1. Note that for the sake of allowing straightforward labelling of different regions of the plasma, many authors name the region local to r_1 as the 'singular layer' even when $\omega \neq 0$.

Due to the contrasting behaviour between the plasma in the singular layer and that of the plasma far from r_1, the dispersion relation is split into two components [14] as follows:

$$D = D^e + D^s \tag{2.39}$$

with,

$$\begin{aligned} D^e(\boldsymbol{\xi}^e) &= \delta W^e(\boldsymbol{\xi}^e) \\ D^s(\boldsymbol{\xi}^s) &= \delta W^s(\boldsymbol{\xi}^s) + \delta K^s(\boldsymbol{\xi}^s), \end{aligned} \tag{2.40}$$

where subscript s and e denotes 'singular' and 'external' respectively. Singular quantities correspond to the region $r_1 - \delta/2 \lesssim r \lesssim r_1 + \delta/2$ and external quantities to locations elsewhere in the plasma. Here, δ is an estimation of the singular layer width. The size of which is derived later.

The minimisation of δW presented earlier is now simply that of the external region. The leading order external displacement which was calculated by minimising

Eq. (2.32), is now defined as:

$$\xi^e_{r0} = \begin{cases} \xi_0\, e^{i(\theta-\phi-\omega t)} & \text{for } r \lesssim r_1 - \delta/2, \\ 0 & \text{for } r \gtrsim r_1 + \delta/2 \end{cases} \tag{2.41}$$

where ξ_0 is a constant. The singular radial displacement ξ^s_r must match asymptotically to Eq. (2.41) close to $r_1 - \delta/2$ and $r_1 + \delta/2$.

It remains to minimise D^s with respect to $\boldsymbol{\xi}^s$ using the boundary conditions defined in Eq. (2.41). First, however, it is necessary to consider the magnitude of the eigenvalue ω. For $|\omega| \sim \omega_{*pi}$, then for a typical equilibrium:

$$|\omega|/\omega_A \sim \varepsilon^2,$$

where $\omega_A = v_A/R_0$ and $v_A = B_0/(\rho\mu_0)^{1/2}$ is the Alfvén velocity, which implies that $\delta K^s \sim O(\varepsilon^4)$ such that $D^e/D^s \sim 1$. In this limit both $\overline{\delta W}$ and Eq. (2.26) are negligible to $O(\varepsilon^4)$ within the singular layer. That is $\boldsymbol{\nabla}\cdot\boldsymbol{\xi}^s = 0$ and $\xi^s_{\theta 0} = i\partial(r\xi^s_{r0})/\partial r$. Also, Eq. (2.30) is satisfied within the singular layer with $\xi^s_{\|} = -2\,\xi^s_{\theta 0}\, q\cos\theta$. Hence writing $\xi^s_r(r,\theta,\phi,t) = \hat{\xi}^s_r(r)e^{i(\theta-\phi-\omega t)}$ and recalling that $\xi^s_\theta \approx ir\partial\xi^s_r/\partial r >> \xi^s_r$ within the singular layer,

$$\delta K^s_4 = \pi R_0\,\gamma_I^2 \int dr\,\rho r \left(r\frac{d\hat{\xi}^s_r}{dr}\right)^2 \int_{-\pi}^{\pi} d\theta\,(1+4q^2\cos^2\theta), \tag{2.42}$$

where the appropriate limits of the radial integration are defined shortly and the subscript 'zero' has been dropped from the singular radial eigenfunction without loss of generality. Also, γ_I is the ideal MHD growth rate which, when ideal MHD applies, is defined by

$$\gamma_I^2 = -\omega^2. \tag{2.43}$$

The potential energy of Eq. (2.32) does not minimise to zero within the singular layer. Combining Eq. (2.32) with Eq. (2.42) and expanding about r_1 gives,

$$D^s_4 = \frac{2\pi^2 R_0 B_0^2}{\mu_0}\varepsilon_1^2 s_1^2 \int_{-\infty}^{\infty} dx \left[x^2 + \left(\gamma_I \frac{\sqrt{1+2q^2}}{s_1\omega_A}\right)^2\right]\left(\frac{d\hat{\xi}^s_r}{dx}\right)^2, \tag{2.44}$$

where $x = (r-r_1)/r_1$ is the local normalised radius, $s = (r/q)dq/dr$ is the shear and $s_1 = s(r_1)$. The integration limits ($\pm\infty$) are appropriate because an asymptotic match between the singular and external eigenfunctions is being sought.

Equation (2.44) is minimised with respect to ξ^s_r by the Euler-Lagrange equation,

$$\frac{d}{dx}\left[\left\{\left(\frac{\sqrt{3}\gamma_I}{s_1\omega_A}\right)^2 + x^2\right\}\left(\frac{d\hat{\xi}^s_r}{dx}\right)^2\right] = 0,$$

giving,

$$\frac{d\hat{\xi}^s_r}{dx} = \frac{C}{x^2 + \left(\frac{\sqrt{3}\gamma_I}{s_1\omega_A}\right)^2}. \tag{2.45}$$

Integrating Eq. (2.45) with respect to x and substituting the external solutions of Eq. (2.41) yields the constant of integration

$$C = -\xi_0 \Big/ \int_{-\infty}^{\infty} \frac{dx}{x^2 + \left(\frac{\sqrt{3}\gamma_I}{s_1\omega_A}\right)^2} = -\frac{2\xi_0}{\pi}\frac{\sqrt{3}\gamma_I}{s_1\omega_A}\,. \tag{2.46}$$

From Eqs. (2.45) and (2.46):

$$\frac{d\hat{\xi}_r^s}{dx} = -\frac{2\xi_0}{\pi}\left(\frac{\gamma_I\sqrt{3}}{\omega_A s_1}\right)\frac{1}{x^2 + \left(\frac{\gamma_I\sqrt{3}}{\omega_A s_1}\right)^2}, \tag{2.47}$$

where the radial dependence of $d\xi_r^s/dr$ is contained in x. Straightforward integration of Eq. (2.47) now gives,

$$\hat{\xi}_r^s = \xi_0\left[1 - \frac{2}{\pi}\arctan\left(x\frac{\omega_A s_1}{\gamma_I\sqrt{3}}\right)\right].$$

Note that at r_1

$$\frac{d\hat{\xi}_r^s}{dr} = -\frac{2\xi_0}{\pi r_1}\left(\frac{\omega_A s_1}{\gamma_I\sqrt{3}}\right). \tag{2.48}$$

As expected, for $\gamma_I = 0$ (i.e. zero inertia), Eq. (2.48) and hence the poloidal and toroidal displacements, are singular at r_1. It is now clear that finite inertia removes the singular poloidal and parallel momenta. Also the width of the singular layer relative to r_1 can be estimated by approximating the singular displacement such that its radial derivative is constant (see Fig 2.7), i.e.:

$$\frac{\delta}{r_1} \sim \frac{\xi_0}{(r_1 d\hat{\xi}_r^s/dr)}\bigg|_{r_1} = \frac{\sqrt{3}\pi\gamma_I}{2s_1\omega_A} \lesssim O(\varepsilon^2).$$

Hence, as discussed earlier, the layer width reduces to zero for negligible γ_I.

The eigenfunction of Eq. (2.47) can now substituted into Eq. (2.44). This gives

$$D_4^s = 4R_0\varepsilon_1^2 s_1^2\frac{B_0^2}{\mu_0}\xi_0^2\left(\frac{\sqrt{3}\gamma_I}{s_1\omega_A}\right)^2\int_0^{\infty}\frac{dx}{x^2 + \left(\frac{\sqrt{3}\gamma_I}{s_1\omega_A}\right)^2} = 2\pi R_0\varepsilon_1^2 s_1\frac{B_0^2}{\mu_0}\xi_0^2\frac{\sqrt{3}\gamma_I}{\omega_A},$$

where ω_A is evaluated at r_1. From Eqs. (2.39) and (2.40) the ideal internal kink mode dispersion relation is

$$\frac{\gamma_I}{\omega_A} = -\varepsilon_1^2\frac{\sqrt{3}\pi}{s_1}\delta\hat{W}_4^e, \tag{2.49}$$

where the '$\hat{}$' corresponds to the normalisation defined in Eq. (2.33). For equilibria with circular flux surfaces, Bussac's [15] expression for $\delta\hat{W}_4^e$ is often substituted into the ideal MHD dispersion relation defined above. It should be noted that Eq. (2.49) differs from the dispersion relation of Ref. [15] by the factor of $\sqrt{3}$ arising as a consequence of the correct inclusion of the parallel inertia.

It is important to mention that providing δW^e is real and positive, γ_I should formally be replaced with $|\gamma_I|$. Hence, as expected in ideal MHD, two equal and opposite solutions exist. The kink mode branch is the mode usually discussed in the context of sawteeth: it corresponds to positive γ_I. The ion mode branch has negative γ_I. In practice, however, the smallest amount of resistivity suppresses damped modes.

2.4.6 Growth Rates in Collisionless MHD

It was mentioned earlier that ideal and collisionless MHD predict identical stability boundaries. This is a consequence of the incompressibility of ideal MHD modes. The internal kink mode would have identical growth rates in both regimes if were it not for Glasser *et al*'s [16] discovery of the importance of parallel inertia.

In the collisionless MHD model the parallel flow is uncoupled from the equation of motion, and the energy principle is entirely independent of $\xi_{||}$ (see Eq. (2.18)). Consequently the inertia only contains the poloidal flow and the factor $\sqrt{3}$ is lost. Therefore the ideal growth rate of collisionless MHD is an enhancement of Eq. (2.49) given by

$$\frac{\gamma_I}{\omega_A} = -\varepsilon_1^2 \frac{3\pi}{s_1} \delta\hat{W},$$

where the subscript '4' and superscript 'e' is henceforth assumed. It is interesting to note that whilst Bussac's prediction of γ_I is not correct in ideal MHD, it is valid in collisionless MHD.

That ideal and collisionless MHD predict differing growth rates is curious, especially when one recalls that in collisionless MHD the parallel displacement is uniquely identified through $\boldsymbol{\nabla} \cdot \boldsymbol{\xi} = 0$, and so is identical to the ideal MHD quantity $\xi_{||} = -2\,\xi_{\theta 0}\, q \cos\theta$. In fact, the collisionless MHD model does not correctly account for the time scales of the collisionless internal kink mode. Using a drift kinetic treatment for the internal kink mode, it will be shown that thermal ions in the banana regime give rise to an inertial enhancement which is much larger than the enhancement arising from the parallel inertia in ideal MHD.

2.4.7 Additional Effects in the Layer

It was shown in the last section that the growth of the internal kink mode is sufficiently small that inertial effects are negligible in most of the plasma. Also, over most of the plasma the resistivity is negligible and the motion can be adequately described by ideal MHD. However, this is not necessarily the case at a resonant surface $m = nq$. It is prudent therefore to consider the growth rate of the resistive tearing mode.

To see why resistivity is important at the resonance layer, one must consider the resistive Ohm's law $\boldsymbol{E} + \boldsymbol{u} \times \boldsymbol{B} = \eta \boldsymbol{j}$, with η the resistivity. Linearising this with perturbations $\sim e^{(im\theta - in\phi + \gamma_R t)}$ and using Faraday's and Ampère's laws gives

$$\gamma_R \left[1 - \frac{iB_0}{Rq}(m - nq)\frac{\xi_r}{\delta B_r}\right] = \frac{\eta}{\mu_0 \delta B_r} \nabla^2 \delta B_r.$$

Hence, it can be seen that at the resonant surface, the $\boldsymbol{\delta u} \times \boldsymbol{B}$ contribution of Ohm's law vanishes and, in the neighbourhood of this surface the $\eta\,\delta j$ term becomes important in balancing the induced field δE.

Tearing modes require solving ideal equations over most of the plasma and incorporating resistive effects in a layer around the resonant surface. The $m = n = 1$ resistive growth rate, calculated at ideal MHD marginal stability ($\delta W = 0$), is [53]:

$$\gamma_R = \frac{1}{\tau_R^{1/3}\tau_H^{2/3}}$$

where $\tau_H = 1/(\omega_A s_1)$ and $\tau_R = \mu_0 r_1^2/\eta$. The resistive $m = n = 1$ mode, unlike other modes ($m \geq 2$), is always unstable. The $m = 1$ mode is fundamentally different because the leading order external eigenfunction is a step function.

The purely ideal and resistive analyses have been generalised into a single theory [19]. Defining $\Lambda = \gamma/\gamma_R$, the equation for the growth rate γ is given by

$$\gamma_I = \frac{8\gamma}{\Lambda^{9/4}} \frac{\Gamma\left[\left(\Lambda^{3/2}+5\right)/4\right]}{\Gamma\left[\left(\Lambda^{3/2}-1\right)/4\right]}\Bigg|_{r_1},$$

with γ_I the ideal growth rate given by Eq. (2.49) and Γ the standard Gamma Function [54]. The limit $\Lambda = 1$ gives the resistive growth rate $\gamma = \gamma_R$ and $\Lambda \to \infty$ gives the ideal limit $\gamma = \gamma_I$. $\Lambda \ll 1$, which corresponds to strong ideal stability, is often labelled as the tearing mode regime because the solution behaves similarly to more prevalent tearing modes with $m \geq 2$. One should also note that for all values of γ_I (positive and negative), $\gamma > 0$ and there is no stability threshold.

It has been highlighted that resistivity can be important at the resonance layer because the $\boldsymbol{u} \times \boldsymbol{B}$ component of Ohm's law vanishes. Other terms usually neglected from the generalised Ohm's law

$$\boldsymbol{E} + \boldsymbol{u} \times \boldsymbol{B} = \eta \boldsymbol{j} + \frac{1}{e n_e}(\boldsymbol{j} \times \boldsymbol{B} - \boldsymbol{\nabla} P_e), \tag{2.50}$$

are also significant at the layer. Rather than using the generalised one fluid Ohm's law, one may equivalently employ a two fluid description of the plasma within the vicinity of r_1. Assuming quasi-neutrality, the ion and electron equations of motion are,

$$m_i n_e \frac{d\boldsymbol{u_i}}{dt} = eZn_e[\boldsymbol{E} + \boldsymbol{u_i} \times \boldsymbol{B} - \eta \boldsymbol{j}] - \boldsymbol{\nabla} P_i \tag{2.51}$$

$$m_e n_e \frac{d\boldsymbol{u_e}}{dt} = -en_e[\boldsymbol{E} + \boldsymbol{u_e} \times \boldsymbol{B} - \eta \boldsymbol{j}] - \boldsymbol{\nabla} P_e, \tag{2.52}$$

where Z is the charge number. The equilibrium flows, assumed to be zero in the previous stability analysis, can now be calculated. Noting that the left hand sides of Eqs. (2.51) and (2.52) are much smaller than the right hand sides and also ignoring η, the equilibrium drifts are,

$$\boldsymbol{u}_{\perp i} = \boldsymbol{u}_E + \boldsymbol{u}_{*pi} \text{ and } \boldsymbol{u}_{\perp e} = \boldsymbol{u}_E + \boldsymbol{u}_{*pe}$$

with

$$\boldsymbol{u}_E = \frac{\boldsymbol{E}\times\boldsymbol{B}}{B^2} \ , \ \boldsymbol{u}_{*pi} = -\frac{\boldsymbol{\nabla}P_i\times\boldsymbol{B}}{eZn_eB^2} \text{ and } \boldsymbol{u}_{*pe} = \frac{\boldsymbol{\nabla}P_e\times\boldsymbol{B}}{en_eB^2}. \tag{2.53}$$

The equilibrium drift velocity $\boldsymbol{u}_E$ exists in plasmas with an equilibrium electric field. Providing $\boldsymbol{u}_E$ is not so large that it gives rise to centrifugal effects, the consequences of an equilibrium $\boldsymbol{E}$ in a pure fluid problem can be removed by transforming the plasma reference frame to one in which the electric field is zero, i.e. $\boldsymbol{u}_E$. This is possible because, as shown in Eq. (2.53), both the electron and ion fluid drifts move together. Hence, an equilibrium current due to finite $\boldsymbol{E}$ does not exist. Such an analysis is given a thorough treatment in Chapter 6 where it is shown that a collisionless plasma, unlike the collisional MHD plasma, is sensitive to an equilibrium $\boldsymbol{E}$.

The two other drifts $\boldsymbol{u}_{*pi}$ and $\boldsymbol{u}_{*pe}$ are the ion and electron velocities respectively. These drifts oppose one another and give rise to the diamagnetic current $\boldsymbol{j}_\perp = -(\boldsymbol{\nabla}P\times\boldsymbol{B})/B^2$, with $P = P_i + P_e$. This current is represented in ideal MHD by the force balance equation. The diamagnetic velocities do not enter the ideal MHD equations explicitly because they cannot be defined in a single fluid model. In the layer the mode frequency ω is Doppler shifted by the diamagnetic frequencies

$$\omega_{*pi} = -\frac{P_i'}{eZn_iB_0r} \text{ and } \omega_{*pe} = \frac{P_e'}{en_iB_0r}, \tag{2.54}$$

with $' \equiv d/dr$. Bussac *et al* [17] and later Ara *et al* [18] generalised the Coppi *et al* [19] resistive internal kink calculation to include diamagnetic effects:

$$\gamma_I^2 = -\omega(\omega-\omega_{*pi})\left[\frac{8}{\Lambda^{9/4}}\frac{\Gamma\left[\left(\Lambda^{3/2}+5\right)/4\right]}{\Gamma\left[\left(\Lambda^{3/2}-1\right)/4\right]}\right]^2\Bigg|_{r_1}, \tag{2.55}$$

where

$$\Lambda = -\frac{i[\omega(\omega-\hat{\omega}_{*pe})(\omega-\omega_{*pi})]^{1/3}}{\gamma_R},$$

with $\hat{\omega}_{*pe} = (1+0.71\eta_e)\omega_{*pe}$, $\eta_e = d\ln T_e/d\ln n_e$. Note that the modifications come from the inertial layer and all quantities are evaluated at $r = r_1$. The generalised dispersion relation allows for the possibility of complex eigenvalues, so that the growth rate of a mode is now $\gamma = \Im\{\omega\}$ and the oscillation frequency $\omega_r = \Re\{\omega\}$. A thorough discussion on the various thresholds and solutions contained in Eqs. (2.55) is given in Ref. [55].

The ideal limit (i.e non-resistive limit) now contains diamagnetic effects. It is obtained by taking $\Lambda >> 1$ in Eq. (2.55):

$$\gamma_I^2 = -\omega(\omega-\omega_{*pi}(r_1)), \tag{2.56}$$

and from Eq. (2.49) the ideal dispersion relation is given by

$$\frac{i\sqrt{\omega(\omega-\omega_{*pi})}}{\omega_A}\Bigg|_{r_1} = \varepsilon_1^2\frac{\sqrt{3}\pi}{s_1}\delta\hat{W}. \tag{2.57}$$

The eigenvalues are defined by $\omega = \omega_{*pi}/2 \pm (\omega_{*pi}^2/4 - \gamma_I^2)^{1/2}$. For $|\gamma_I| > \omega_{*pi}/2$, two complex solutions exist. The limit $|\gamma_I| \gg \omega_{*pi}/2$ corresponds to the ideal MHD kink mode and ion mode branches with $\gamma \approx \gamma_I$. However, if $|\gamma_I| < \omega_{*pi}/2$, a new regime exists. In such cases both modes are marginally stable ($\gamma = 0$) and each possess a pure oscillation frequency ω_r. One mode satisfies $0 < \omega_r < \omega_{*pi}/2$ and the other $\omega_{*pi}/2 < \omega_r < \omega_{*pi}$. Hence, up to the limit $|\gamma_I| = \omega_{*pi}/2$, the ideal modes are marginally stable for $\delta W > 0$. This demonstrates that diamagnetic effects can stabilise the internal kink mode. Often such stabilisation is described as a consequence of finite Larmor radius (FLR) corrections.

The dispersion relation contains rather different regimes when kinetic effects are included. Kinetic terms introduce the possibility that δW and hence γ_I are complex. In a detailed paper involving resistive and kinetic effects, Coppi *et al* [32] made a distinction between the two ideal and marginally stable modes by stating that the branch satisfying $0 < \omega_r < \omega_{*pi}/2$ corresponds to the sawtooth instability and the $\omega_{*pi}/2 < \omega_r < \omega_{*pi}$ branch to a fishbone instability. However, other authors, e.g. White *et al* [31], have shown that upon introducing kinetic terms, the ideal marginally stable sawtooth branch may correspond to $\omega_r > \omega_{*pi}$. An argument, which includes the kinetic effects of a highly energetic species, is presented in Chapters 4 and 5 agreeing with Ref. [31]. Also, the modification of Eq. (2.57) relative to a finite equilibrium electric field is treated in Chapter 6.

2.5 Summary

The purpose of this chapter has been to present a literature review of the kinetic stabilisation of the internal kink mode, and to describe in detail the 'fluid-like' behaviour of the instability. In particular, the ideal MHD growth rate has been derived in terms of the potential energy of the mode. Details have also been presented which illustrate the modifications to the dispersion relation resulting from finite diamagnetic effects, resistive effects, parallel inertia and the collisionless MHD limit.

It is now of interest to investigate the effects that collisionless populations of ions have on the internal kink mode stability. Chapters 3 and 4 contain details of the kinetic modifications to the internal kink mode dispersion relation. It will become clear that the collisionless MHD model described in the present chapter is strongly lacking in its ability to characterise the dynamics arising as a consequence of collisionless ions.

Chapter 3

Kinetic Additions to the Internal Kink Mode

The last chapter contained a description and review of MHD stability and the internal kink mode. This theoretical background can now be extended to include the effects of energetic particles. Such an analysis must account for the motion of single particles and their collective behaviour in a tokamak.

The level of detail contained in the last and present chapters is motivated by a growing demand in the fusion community for a detailed derivation of the kinetic internal kink mode. Theory which correctly accounts for the kinetic effects of collisionless ion populations requires a broad spectrum of techniques which must be coupled with the MHD stability analysis exhibited in Chapter 2. The present chapter attempts to put the kinetic internal kink mode in a coherent picture which details the modified stability boundary for thermal ions in the banana regime.

3.1 Energetic Particle Motion

In this section the primary aspects of individual energetic particle motion are considered. The equation of motion for a particle with charge eZ and mass m_i is

$$m_i \frac{d\boldsymbol{v}}{dt} = eZ(\boldsymbol{E} + \boldsymbol{v} \times \boldsymbol{B}), \tag{3.1}$$

where $\boldsymbol{v}$ is the velocity of the particle. The right hand side of Eq. (3.1) represents the force acting on the particle. For tokamaks, external forces such as gravity are negligible in comparison with the electromagnetic forces present.

3.1.1 Gyro Motion

Consider Eq. (3.1) with a uniform magnetic field but absent of an electric field. The parallel and perpendicular components are

$$\frac{d\boldsymbol{v}_{\parallel}}{dt} = 0 \text{ and } \frac{d\boldsymbol{v}_{\perp}}{dt} = \frac{eZ}{m_i}(\boldsymbol{v}_{\perp} \times \boldsymbol{B}). \tag{3.2}$$

For motion in the plane perpendicular to $\boldsymbol{B}$, Eq. (3.2) is differentiated with respect to time:

$$\frac{d^2\boldsymbol{v}_{\perp}}{dt^2} = -\omega_c^2 \boldsymbol{v}_{\perp}, \tag{3.3}$$

where $\omega_c = eZB/m_i$ is the cyclotron frequency, or gyro frequency. The radius of the circular orbit

$$r_c = \frac{v_{\perp}}{\omega_c} = \frac{m_i v_{\perp}}{eZB},$$

is referred to as the gyro radius or more frequently the Larmor radius. Also, from Eq. (3.2), it is clear that the particle velocity parallel to the magnetic field is constant.

3.1.2 The Conservation of the Magnetic Moment

The gyro motion of a charged particle in a magnetic field produces a circulating electric current. The magnetic field generated by this current at distances much larger than the Larmor radius, r_c, is a magnetic dipole. The corresponding magnetic moment is defined as:

$$\frac{m_i v_{\perp}^2}{2B}.$$

The analysis is simplified by removing the mass dependence from various definitions. For example, the kinetic energy is henceforth defined as $\mathcal{E} = v^2/2$ and the magnetic moment as

$$\mu = \frac{v_{\perp}^2}{2B} = \frac{\mathcal{E}_{\perp}}{B}. \tag{3.4}$$

The magnetic moment remains almost constant during the particle motion. It's invariance depends on the time scale and length-scale variation of $\boldsymbol{B}$. If the magnetic field varies in time, Faraday's law implies that this will lead to an induced electric field which can do work on the particle and thus change its energy. The change in energy over one cyclotron orbit time $\tau_c = 2\pi/\omega_c$ is

$$\Delta\mathcal{E}_{\perp} = \frac{eZ}{m_i} \oint \boldsymbol{E} \cdot d\boldsymbol{L} = -\frac{eZ}{m_i} \int_S \frac{\partial \boldsymbol{B}}{\partial t} \cdot d\boldsymbol{S},$$

where the contour integral follows the gyro-orbit and S corresponds to the surface area spanned by this loop. If the variation is so slow that B is effectively constant over one orbit, i.e. $\partial B/\partial r \ll B/r_c$ and $\partial B/\partial t \ll B/\tau_c$, then

$$\begin{aligned} \Delta\mathcal{E}_{\perp} &= \frac{eZ\pi r_c^2}{m_i}\frac{\partial B}{\partial t} = \frac{\mathcal{E}_{\perp}}{B}\tau_c \frac{\partial B}{\partial t} \\ &= \frac{\mathcal{E}_{\perp}}{B}\Delta B, \end{aligned}$$

Hence, referring to Eq. (3.4),

$$\Delta\left(\frac{\mathcal{E}_\perp}{B}\right) \equiv \Delta\mu = 0,$$

and thus μ remains invariant as B changes. However, in practice, due to the finite sizes of τ_c and r_c, the magnetic moment is not exactly conserved. For this reason μ is said to be an adiabatic invariant.

3.1.3 Energy Conservation in Equilibrium

If the plasma is in a state of equilibrium, the explicit time dependence of electromagnetic and fluid quantities vanish, i.e. $\partial/\partial t \equiv 0$. In such instances, it can be shown that the total energy assigned to each particle is conserved. Forming the dot product of Eq. (3.1) with $\boldsymbol{v}$ gives

$$\frac{d}{dt}\left(\frac{1}{2}m_i v^2\right) = eZ\boldsymbol{E}\cdot\boldsymbol{v}. \tag{3.5}$$

Letting $\boldsymbol{E} = -\boldsymbol{\nabla}\Phi$, where Φ is the electrostatic potential, and recalling that $d/dt = \boldsymbol{v}\cdot\boldsymbol{\nabla}$ during equilibrium, obtains

$$\frac{d}{dt}\left[\frac{1}{2}m_i v^2 + eZ\Phi\right] = 0.$$

Hence, the sum of the kinetic energy and the electric potential energy is conserved during equilibrium.

3.1.4 Guiding Centre Approximation

If the requirements for the adiabatic invariance of μ are satisfied, one can neglect the rapid gyro motion observed in Eq. (3.3). This reveals a simpler picture of the particle motion. Averaging Eq. (3.1) over one gyro orbit gives the guiding centre velocity [34]:

$$\boldsymbol{v}_g = v_{\|}\hat{\boldsymbol{e}}_{\|} + \boldsymbol{v}_E + \boldsymbol{v}_{md}, \tag{3.6}$$

where

$$\boldsymbol{v}_E = \frac{\boldsymbol{E}\times\boldsymbol{B}}{B^2} \text{ and } \boldsymbol{v}_{md} = \frac{m_i\boldsymbol{B}}{eZB^2}\times\left[v_{\|}^2\boldsymbol{\kappa} + \mu\boldsymbol{\nabla}B\right] \tag{3.7}$$

and the curvature vector $\boldsymbol{\kappa}$ is defined in Eq. (2.15). The first term in Eq. (3.6) represents the parallel velocity of the guiding centre along a field line. The other terms describe the perpendicular drift away from it. $\boldsymbol{v}_E$ represents the so called $\boldsymbol{E}\times\boldsymbol{B}$ drift; this is the drift away from the magnetic field lines due to the electric field. $\boldsymbol{v}_{md}$ corresponds to the drift due to the non-homogeneity in the magnetic field. This can be split up into two components as shown in Eq. (3.7). The first of these is commonly known as the curvature drift and the second the $\boldsymbol{\nabla}B$ drift. It will be shown in the subsequent sections that the drift velocity defined above plays a crucial role in determining the kinetic stability of the internal kink mode.

3.1.5 Particle Trapping

The guiding centre motion exhibited in Eqs. (3.6) and (3.7) essentially describes two classes of particles: passing and trapped. To leading order, passing particles follow magnetic field lines and complete a poloidal circuit on a unique flux surface. Some particles, however, do not pass into the inboard ($\theta = \pi$) side of the torus. Since the toroidal magnetic field is proportional to $1/R$, the field strength is smaller on the outboard ($\theta = 0$) side, and particles in this region which have a small pitch angle, $v_{\|}/v_{\perp}$, undergo a magnetic mirror reflection as they move into the region of higher field. In the absence of collisions these particles are trapped in the low field region, undergoing repeated reflections as they bounce backwards and forwards between turning points as depicted in Fig. 3.1. The trapped particle trajectory projected onto the r, θ plane traces out a shape resembling a banana. Consequently, trapped particles are said to complete banana orbits. The radial width of the banana is often assumed negligible in analytical work such as this, in which case the particle is approximately confined to a unique flux surface r.

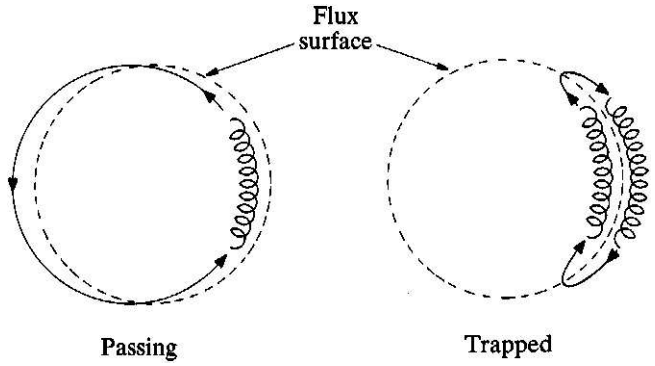

Figure 3.1: Showing the poloidal trajectories of typical passing and trapped particles respectively.

The turning points of a trapped particle correspond to the locations at which $v_{\|} = 0$. It is instructive to define the parallel velocity as follows:

$$v_{\|}^2 = 2\mathcal{E}(1 - \alpha B), \tag{3.8}$$

with $\mathcal{E} = v^2/2$ and $\alpha = \mu/\mathcal{E}$ a pitch angle variable. For an equilibrium absent of $\boldsymbol{E}$, both $\mathcal{E}$ and α are conserved quantities ($\mathcal{E}$ is not conserved if the equilibrium accommodates a finite electric field; such a case is not treated until Chapter 6). For trapped particles, the parallel velocity is reduced to zero at a point on a flux surface where the magnetic field strength is smaller than the maximum field strength. For a particular flux surface, the maximum magnetic field strength exists at $\theta = \pi$. Therefore, the condition for trapping is $\alpha B(\theta = \pi) > 1$. Also, since all particles,

trapped and passing, exist at some time in the region of low field ($\theta = 0$), it is convenient to discuss the trapping condition in terms of $v_{\|}(\theta = 0)$ and $v_{\perp}(\theta = 0)$. Exploiting the conservation of $\mathcal{E}$ and α, the trapping condition becomes

$$\frac{1+\varepsilon}{1-\varepsilon} > 1 + \left(\frac{v_{\|}(\theta=0)}{v_{\perp}(\theta=0)}\right)^2,$$

or, since ε is small, the trapping condition can be written in an approximate, but more informative manner:

$$\frac{v_{\|}(\theta=0)}{v_{\perp}(\theta=0)} < \sqrt{2\varepsilon}. \tag{3.9}$$

Hence, for an isotropic distribution function such as a Maxwellian, the fraction of trapped particles is of the order $\varepsilon^{1/2}$. In a large tokamak such as JET, the fraction of isotropically distributed collisionless particles trapped at the $q = 1$ surface approaches around one third. This number diminishes to zero towards the centre. For a highly anisotropic population of energetic ions such as a minority population heated with ICRH, the trapping condition above is met by most ions at r_1. It will become clear that the kinetic modification of the internal kink mode stability boundary comes solely from the trapped population. Hence, the impact of ICRH on the stability of the internal kink mode is particularly important.

3.1.6 The Bounce Time

The time a particle takes to complete a closed orbit is given by $\tau = \oint dt$. If the particles approximately follow magnetic field lines, one can write $dt = dl/v_{\|}$. Hence, using the identity $dl = d\theta\,/(\hat{\boldsymbol{e}}_{\|} \cdot \boldsymbol{\nabla})\theta$ yields

$$dt = \frac{dl}{v_{\|}} = qR\frac{d\theta}{v_{\|}}. \tag{3.10}$$

The θ dependence of R is very weak compared with that of $v_{\|}$. Hence, an approximate relation for the orbit time is

$$\tau = qR_0 \oint \frac{d\theta}{v_{\|}(\theta)}. \tag{3.11}$$

Now consider $v_{\|}(\theta)$. From Eq. (3.8) and using $B = B_0(1 - \varepsilon\cos\theta)$ one can write

$$v_{\|}(\theta) = 2\left[\mu B_0 \varepsilon \left(k^2 - \sin^2(\theta/2)\right)\right]^{1/2}, \tag{3.12}$$

where

$$k^2 = \frac{1 + \alpha B_0(\varepsilon - 1)}{2\varepsilon\alpha B_0} \tag{3.13}$$

is a new pitch angle variable. Hence

$$\tau = \frac{qR_0}{\sqrt{\mu B_0 \varepsilon}} \oint \frac{dx}{\sqrt{k^2 - \sin^2 x}}, \tag{3.14}$$

where $x = \theta/2$. The form of τ is fundamentally different depending on whether $k^2 > 1$ or $k^2 < 1$. It is clear from Eq. (3.12) that $k^2 < 1$ is the trapping condition. Similarly, $k^2 > 1$ corresponds to passing particles and $k^2 = 1$ to the unlikely possibility that a particle might be trapped at the trapped - passing boundary of $\theta = \pi$.

The orbit time of passing particles is straightforward to calculate. Direct integration of Eq. (3.14) around a passing loop ($0 \leq \theta \leq 2\pi$) gives

$$\tau_p = \frac{2\sqrt{2}qR_0}{\sqrt{\mathcal{E}}\,[1 + \alpha B_0(\varepsilon - 1)]^{1/2}}\,K(1/k^2), \tag{3.15}$$

where,

$$K(j^2) = \int_0^{\pi/2} \frac{dx}{\sqrt{1 - j^2 \sin^2 x}} \tag{3.16}$$

is a complete elliptic integral of the first kind [54].

For trapped particles, a new integral variable X is introduced. It is defined

$$k \sin X = \sin x. \tag{3.17}$$

Using $dx = k \cos X\, dX \Big/ \sqrt{1 - k^2 \sin^2 X}$ and $k^2 - \sin^2 x = k^2 \cos^2 X$, the change of variable introduces an integral of the type:

$$\oint \frac{dX}{\sqrt{1 - k^2 \sin^2 X}} \equiv \oint \frac{dx}{\sqrt{k^2 - \sin^2 x}}.$$

The contour integration must be considered carefully. Since the banana width is assumed negligible we are permitted to only integrate between the limits $0 \leq \theta \leq \theta_b$, with θ_b the bounce angle, so that $\oint d\theta = 4\int_0^{\theta_b} d\theta$. Now, since $v_{\|} = 0$ at $\theta = \theta_b$, it is clear from Eq. (3.12) that $x_b = \arcsin k$. Hence from Eq. (3.17), a bounce point in X corresponds to $X_b = \pi/2$. Thus

$$\tau_b = \frac{4qR_0}{\sqrt{\mu B_0 \varepsilon}}\,K(k^2). \tag{3.18}$$

Consequently a deeply trapped particle (corresponding to $k = 0$ and $\theta = 0$) bounces at a frequency

$$\omega_b(k^2 = 0) = \frac{2\pi}{\tau_b(k^2 = 0)} = \left(\frac{\varepsilon}{2}\right)^{1/2} \frac{v_{\perp}(\theta = 0)}{qR_0}. \tag{3.19}$$

3.1.7 The Longitudinal Invariant and the Precession Drift

The longitudinal invariant $\mathcal{J}$ is an adiabatic invariant for magnetically trapped particles. The importance of $\mathcal{J}$ is that trapped particles are constrained to drift on the surface described by

$$\mathcal{J}(\psi, \mathcal{E}, \mu) = \oint v_{\|}(l, \psi, \mathcal{E}, \mu)\, dl = \text{constant},$$

with ψ a flux variable and $v_{||} = \sqrt{2[\mathcal{E} - \mu B(\psi, l)]}$. Using $\mathcal{J}$, much can be learned about the particle trajectory without the need to integrate the equation of motion of the gyrating particle or the guiding centre.

The longitudinal invariant provides access to a tractable calculation for the magnetic drift velocity averaged over a single banana orbit:

$$\langle \boldsymbol{v}_{md} \rangle = \oint \boldsymbol{v}_{md}\, dt/\tau_b.$$

The bounce averaged velocity in the r, θ plane is of course zero, but a finite toroidal velocity exists, i.e. $\langle \boldsymbol{v}_{md} \rangle = \langle v_{md} \rangle \boldsymbol{e}_\phi$. Rosenbluth and Sloan [56] showed that the toroidal precession frequency of a particle is given by

$$\langle \omega_{md} \rangle = \frac{\langle v_{md} \rangle}{R} = \frac{m_i}{Ze} \frac{\partial \mathcal{J}}{\partial \psi} \left(\frac{\partial \mathcal{J}}{\partial \mathcal{E}} \right)^{-1},$$

where r is related to the flux variable ψ through $rB_0 dr = q(r) d\psi$. From Eq. (3.11), it is straight forward to identify $\tau_b = \partial \mathcal{J}/\partial \mathcal{E}$. Hence, substituting Eq. (3.10) gives,

$$\langle \omega_{md} \rangle = -\frac{m_i q}{ZeB_0 \varepsilon} \left[\mu q \oint \frac{\partial B}{\partial r} \frac{d\theta}{\sqrt{2(\mathcal{E} - \mu B)}} - \frac{\partial q}{\partial r} \oint d\theta \sqrt{2(\mathcal{E} - \mu B)} \right] \Bigg/ \tau_b, \qquad (3.20)$$

where the first term of Eq. (3.20) arrives as a consequence of the $\boldsymbol{\nabla} B$ drift and the second the curvature drift.

If one substitutes $\partial B/\partial r = -(B_0/R_0)\cos\theta$, the precession drift can be written,

$$\langle \omega_{md} \rangle = \frac{m_i q^2}{Zer} \sqrt{\frac{\mu}{\varepsilon B_0}} \left[\oint \frac{dx(1 - 2\sin^2 x)}{\sqrt{k^2 - \sin^2 x}} + 4s \oint dx \sqrt{k^2 - \sin^2 x} \right] \Bigg/ \tau_b,$$

where $s = (r/q)dq/dr$ is the magnetic shear and $\theta = 2x$. Following the analysis used in the calculation of τ_b one can show that

$$\oint \frac{dx(1 - 2\sin^2 x)}{\sqrt{k^2 - \sin^2 x}} = 4\left[2E(k^2) - K(k^2)\right] \qquad (3.21)$$

$$\oint dx \sqrt{k^2 - \sin^2 x} = 4\left[E(k^2) - (k^2 - 1)K(k^2)\right], \qquad (3.22)$$

where

$$E(j^2) = \int_0^{\pi/2} dx \sqrt{1 - j^2 \sin^2 x}$$

is a complete elliptic integral of the second kind [54]. Hence substituting Eq. (3.18) for τ_b, the precession drift finally becomes

$$\langle \omega_{md} \rangle = \frac{2 m_i q}{Zer R_0} \mu \left[F_1 + 2s F_2 \right], \qquad (3.23)$$

with

$$F_1 = \frac{E(k^2)}{K(k^2)} - \frac{1}{2} \text{ and } F_2 = \frac{E(k^2)}{K(k^2)} + (k^2 - 1). \qquad (3.24)$$

This definition of $\langle \omega_{md} \rangle$ will often feature in the kinetic extensions of the internal kink mode potential energy. However, in Chapter 6, Eq. (3.23) is modified to account for the Shafranov shifting of flux surfaces.

3.2 The Linearised Drift Kinetic Equation

Section 3.1 dealt with some aspects of single particle behaviour. It is now necessary to provide an account on the collective behaviour of energetic particles. Because of the large number of particles involved, this description has to be statistical. This is carried out using a distribution function $f(\boldsymbol{x}, \boldsymbol{v}, t)$ which measures the probability density in the six dimensional space $(\boldsymbol{x}, \boldsymbol{v})$ at time t. The behaviour of $f(\boldsymbol{x}, \boldsymbol{v}, t)$ is described by the kinetic equation. Alternatively, the drift kinetic equation provides a simplified description in which the space - velocity dimensions are reduced to five. It describes the evolution of f under conditions where the time variation is slow compared to the gyro-period τ_c and gradual in space compared to the gyro-radius r_c of the particle orbits.

The distribution function is a function of position $\boldsymbol{q}$, canonical momentum $\boldsymbol{p}$ and time. From Louville's theorem it follows that in the absence of collisions, the number of particles are conserved. Using Hamilton's equations one can show that the divergence of the phase flow is zero, giving

$$\frac{df}{dt} \equiv \frac{\partial f}{\partial t} + \dot{\boldsymbol{q}} \cdot \frac{\partial f}{\partial \boldsymbol{q}} + \dot{\boldsymbol{p}} \cdot \frac{\partial f}{\partial \boldsymbol{p}} = 0. \tag{3.25}$$

Because Eq. (3.25) arrives as a consequence of Hamilton's equations, $\boldsymbol{q}$ and $\boldsymbol{p}$ can be interchanged trivially between different coordinate systems. The most common representation of Eq. (3.25) in plasmas whose force $F = m\dot{\boldsymbol{v}}$ acting on the particles is predominantly electromagnetic is the Vlasov equation:

$$\frac{df}{dt} + \boldsymbol{v} \cdot \frac{\partial f}{\partial \boldsymbol{x}} + \frac{Ze}{m_i}(\boldsymbol{E} + \boldsymbol{v} \times \boldsymbol{B}) \cdot \frac{\partial f}{\partial \boldsymbol{v}} = 0. \tag{3.26}$$

Alternatively, if one assumes that the particles' gyro-motion can be neglected, the distribution function can be written as $f(\boldsymbol{x}_g, \mathcal{E}, \mu)$, with x_g the guiding centre position and $\mathcal{E}$ the gyro-averaged kinetic energy. Hence, from Eq. (3.25), the drift kinetic equation can now be defined as:

$$\frac{\partial f}{\partial t} + \frac{d\boldsymbol{x}_g}{dt} \cdot \frac{\partial f}{\partial \boldsymbol{x}_g} + \frac{d\mathcal{E}}{dt}\frac{\partial f}{\partial \mathcal{E}} = 0, \tag{3.27}$$

where the five variables upon which f depends evolve according to:

$$\frac{d\boldsymbol{x}_g}{dt} = v_\parallel \hat{\boldsymbol{e}}_\parallel + \frac{\boldsymbol{B}}{eZB^2} \times \left[m_i v_\parallel^2 \boldsymbol{\kappa} + m_i \mu \boldsymbol{\nabla} B - eZ\boldsymbol{E}\right] \tag{3.28}$$

$$\frac{d\mu}{dt} = 0 \tag{3.29}$$

$$\frac{d\mathcal{E}}{dt} = \frac{m_i}{Ze}\frac{d\boldsymbol{x}_g}{dt} \cdot \boldsymbol{E} + \mu \frac{\partial B}{\partial t}. \tag{3.30}$$

Equations (3.28) and (3.29) follow from Eqs. (3.6) and (3.4) respectively. The remaining equation, (3.30), describes the rate of change of the gyro-averaged energy and it is obtained as follows. The particle velocity is split into two components

$\boldsymbol{v} = \boldsymbol{\mathcal{V}} + \boldsymbol{v}_c$, where $\boldsymbol{v}_c$ corresponds to the circulating gyro orbit velocity. Equation (3.5) gives

$$\frac{d\mathcal{E}}{dt} = \frac{Ze}{m_i}\boldsymbol{v}_g \cdot \boldsymbol{E} + \frac{Ze}{m_i\tau_c}\oint \boldsymbol{v}_c \cdot \boldsymbol{E}dt,$$

where $\boldsymbol{v}_g = \oint \boldsymbol{\mathcal{V}}dt/\tau_c$ is the guiding velocity defined in Eq. (3.6). If one notes that $\boldsymbol{v}_c dt = d\boldsymbol{L}$, where $\boldsymbol{L}$ is a length following the gyro-orbit, then

$$\oint \boldsymbol{v}_c \cdot \boldsymbol{E}dt = -\int_S \frac{\partial \boldsymbol{B}}{\partial t} \cdot d\boldsymbol{S}$$

and Eq. (3.30) follows on applying the steps of Section 3.1.2.

Solutions of the evolving distribution function are obtained by linearly perturbing Eq. (3.27). Details of this can, for example, be found in Ref. [57].

Assuming the equilibrium electric field is zero, the solution to Eq. (3.27) is [57]:

$$\delta f = \frac{Ze}{m_i}\left(\delta\Phi\frac{\partial}{\partial\mathcal{E}} - \mu\frac{\delta B_\parallel}{\omega_c}\frac{\partial}{\partial\mu}\right) f + \delta h, \tag{3.31}$$

where δh is a solution of the kinetic equation,

$$v_\parallel\frac{\partial\delta h}{\partial l} - i(\omega-\omega_{md})\delta h - i\frac{Ze}{m_i}\frac{\partial f}{\partial\mathcal{E}}(\omega-\omega_*)\left[\delta\Phi - v_\parallel\delta A_\parallel + \frac{v_\perp^2}{2\omega_c}\delta B_\parallel\right] = 0, \tag{3.32}$$

and ω_* is the non-local (energy dependent) diamagnetic frequency. ω_* operates on electromagnetic perturbations, such that:

$$\omega_*\delta\Phi = i\frac{(\hat{\boldsymbol{e}}_\parallel \times \boldsymbol{\nabla} f)\cdot\boldsymbol{\nabla}\delta\Phi}{\omega_c\partial f/\partial\mathcal{E}}. \tag{3.33}$$

The perturbed fields have the form $\delta\Phi = \delta\hat{\Phi}(r)\exp(i\mathcal{R} - i\omega t)$, where $\mathcal{R} = m\theta - n\phi$. The equilibrium distribution function is invariant to the position of particles on a flux surface. Since flux surfaces are defined by a unique r, $\boldsymbol{\nabla} f = (\partial f/\partial r)\hat{\boldsymbol{e}}_r$ and:

$$\omega_* = -\frac{m_i}{eZB}\frac{\partial f}{\partial r}\left(\frac{\partial f}{\partial\mathcal{E}}\right)^{-1}(\hat{\boldsymbol{e}}_\parallel \times \hat{\boldsymbol{e}}_r)\cdot\boldsymbol{\nabla}\mathcal{R}. \tag{3.34}$$

The poloidal and toroidal dependence of δh has yet to be calculated. At this stage we write $\delta h = \delta\hat{h}(r)\exp(i\mathcal{S} - i\omega t)$, where $\mathcal{S} = \mathcal{S}(\theta,\phi)$.

The other 'frequency operator' defined in the drift kinetic equation is the magnetic drift frequency ω_{md}. It operates on δh, such that $\omega_{md}\delta h = \boldsymbol{v}_{md}\cdot\boldsymbol{\nabla}\delta h$. Since the leading order magnetic drift velocity $\boldsymbol{v}_{md}$ does not include a radial drift (i.e. it is assumed that the banana width is zero), the magnetic drift frequency can be defined

$$\omega_{md} = \boldsymbol{v}_{md}\cdot\boldsymbol{\nabla}\mathcal{S}.$$

The electromagnetic disturbances are assumed to be purely of MHD origin. Hence, the perturbed electric field is determined by Ohm's law:

$$\begin{aligned}\delta E_\perp &= -i\omega\boldsymbol{\xi}_\perp \times \boldsymbol{B} \\ \delta E_\parallel &= 0.\end{aligned} \tag{3.35}$$

The generalisation $\delta E_{\|} \neq 0$ has been included in the drift kinetic equation elsewhere and details can be found in Ref. [25].

The perturbed electrostatic potential, $\delta\Phi$, is related to $\boldsymbol{\xi}_\perp$ through Eq. (3.35):

$$\boldsymbol{\nabla}\delta\Phi = -i\omega\boldsymbol{\xi}_\perp \times \boldsymbol{B}. \tag{3.36}$$

Also, the perturbed parallel vector potential accounts for the vanishing of $\delta E_{\|}$:

$$\omega\delta A_{\|} = -i\partial\delta\Phi/\partial l. \tag{3.37}$$

$\boldsymbol{\delta B}$ is related to $\boldsymbol{\xi}_\perp$ through $\boldsymbol{\delta B} = \boldsymbol{\nabla} \times (\boldsymbol{\xi}_\perp \times \boldsymbol{B})$, and a small amount of algebra gives

$$\delta B_{\|} = -B\left[\boldsymbol{\nabla}\cdot\boldsymbol{\xi}_\perp + \frac{(\boldsymbol{\xi}_\perp\cdot\boldsymbol{\nabla})B}{B} + \boldsymbol{\xi}_\perp\cdot\boldsymbol{\kappa}\right].$$

Finally, introducing

$$\delta f_k = \frac{Ze}{m_i}\left[1-\frac{\omega_*}{\omega}\right]\delta\Phi\frac{\partial f}{\partial\mathcal{E}} + \delta h,$$

and referring to Eq. (3.31) yields

$$\delta f = \frac{Ze}{m_i}\left[\frac{\omega_*\delta\Phi}{\omega}\frac{\partial f}{\partial\mathcal{E}} - \frac{\mu\delta B_{\|}}{\omega_c}\frac{\partial f}{\partial\mu}\right] + \delta f_k.$$

Furthermore, Eqs. (3.36), (3.37) and (3.7), the kinetic equation of (3.32) in terms of δf_k can be written as:

$$v_{\|}\frac{\partial\delta f_k}{\partial l} - i(\omega-\omega_{md})\delta f_k + i(\omega-\omega_*)\frac{\partial f}{\partial\mathcal{E}}\left[\mu\delta B_{\|} - v_{\|}^2\boldsymbol{\xi}_\perp\cdot\boldsymbol{\kappa} - \mu\boldsymbol{\xi}_\perp\cdot\boldsymbol{\nabla}B\right] = 0.$$

The form of δf and the kinetic equation can be simplified further as follows. From Eqs. (3.33) and (3.36):

$$\frac{Ze}{m_i}\frac{\omega_*\delta\Phi}{\omega}\frac{\partial f}{\partial\mathcal{E}} = -\boldsymbol{\xi}_\perp\cdot\nabla f.$$

It is appropriate to assume that the kinetic modifications of δW do not alter the form of $\boldsymbol{\xi}$. A demonstration showing that only the core fluid component of δW influences the functional form of $\boldsymbol{\xi}$ will be given later. Hence, assuming $\beta \sim O(\varepsilon^2)$ and referring to Eq. (2.30), obtains

$$\frac{\boldsymbol{\xi}_{\perp 0}\cdot\boldsymbol{\nabla}B}{B} = \boldsymbol{\xi}_{\perp 0}\cdot\boldsymbol{\kappa} = -\frac{1}{2}\boldsymbol{\nabla}\cdot\boldsymbol{\xi}_{\perp 1} \text{ and } \delta B_{\|} = 0.$$

Consequently, the perturbed distribution function can now be defined

$$\delta f = \delta f_f + \delta f_k, \tag{3.38}$$

with

$$\delta f_f = -\boldsymbol{\xi}_\perp\cdot\boldsymbol{\nabla}f$$

and a simplified kinetic equation characterising δf_k:

$$v_{\|}\frac{\partial\delta f_k}{\partial l} - i\delta f_k(\omega-\omega_{md}) - i(\omega-\omega_*)\frac{\partial f}{\partial\mathcal{E}}\left[v_{\|}^2+\mu B\right]\frac{\boldsymbol{\xi}_{\perp 0}\cdot\boldsymbol{\nabla}B}{B} = 0.$$

The subscript 'f' in the term δf_f denotes 'fluid'. This is because δf_f describes the convective perturbation of MHD. The additional perturbation which is not described by MHD is δf_k. Here the subscript 'k' denotes kinetic.

3.3 Internal Kink Stability Boundary for Energetic Thermal Ions

The general form for δf has now been derived. In this section the perturbed distribution function is chosen to describe the collisionless effects of thermal ions. Suitable regimes where the thermal ions are collisionless and the electrons are collisional are discussed in Chapter 6. In the present chapter the extent of the kinetic modifications are limited to describe the ideal internal kink stability boundary. Such an analysis requires only consideration of the external region, which exists outside the singular layer of the $q = 1$ rational surface. The principles obtained in this chapter are employed in an original analysis in Chapter 4 where the kinetic modifications are extended to the singular layer.

The appropriate equilibrium distribution function, f_i, is the Maxwellian. Consequently, equilibrium quantities such as the ion pressure are isotropic. However, the perturbed pressure arising from the kinetic effects of thermal ions is not in general isotropic. To account for the pressure anisotropy we employ Chew *et al*'s [58] double adiabatic model (see also Taylor and Hastie, [59]):

$$\underline{\underline{P}} = P_\perp \underline{\underline{I}} + (P_\parallel - P_\perp)\hat{\boldsymbol{e}}_\parallel \hat{\boldsymbol{e}}_\parallel = \begin{pmatrix} P_\perp & 0 & 0 \\ 0 & P_\perp & 0 \\ 0 & 0 & P_\parallel \end{pmatrix}$$

where $\underline{\underline{I}}$ is the unit dyadic.

From Eq. (3.38) the perturbed ion distribution function is defined

$$\delta f_i = \delta f_{fi} + \delta f_{ki}$$

with

$$\delta f_{fi} = -\boldsymbol{\xi}_\perp \cdot \boldsymbol{\nabla} f_i \tag{3.39}$$

and δf_{ki} is a solution of:

$$v_\parallel \frac{\partial \delta f_{ki}}{\partial l} - i(\omega - \omega_{mdi})\delta f_{ki} - i(\omega - \omega_{*i})\frac{\partial f_i}{\partial \mathcal{E}}\left[v_\parallel^2 + \mu B\right]\frac{\boldsymbol{\xi}_{\perp 0} \cdot \boldsymbol{\nabla} B}{B} = 0. \tag{3.40}$$

The total perturbed ion pressure tensor $\underline{\underline{\delta P}}_i$ is obtained by evaluating the second velocity moments of δf_i. In particular the fluid component is evaluated by taking the second moment of Eq. (3.39) to give:

$$\delta P_{fi} = -\boldsymbol{\xi}_\perp \cdot \boldsymbol{\nabla} P_i. \tag{3.41}$$

This term is identical to that of MHD and combined with the electron contribution gives $\delta P_f = -\boldsymbol{\xi}_\perp \cdot \boldsymbol{\nabla} P$.

Recall that the plasma momentum is carried by the ions. Since the ions are assumed to be collisionless, fluid motion is only defined perpendicularly to the magnetic field in agreement with the collisionless MHD model. Hence it follows that the total force operator can be written as:

$$\boldsymbol{\delta F} = \boldsymbol{\delta j} \times \boldsymbol{B} + \boldsymbol{j} \times \boldsymbol{\delta B} + \boldsymbol{\nabla}(\boldsymbol{\xi}_\perp \cdot \boldsymbol{\nabla} P) - \boldsymbol{\nabla} \cdot \underline{\underline{\delta P}}_{ki}, \tag{3.42}$$

with

$$\underline{\underline{\delta P}}_{ki} = \delta P_{\perp ki}\underline{\underline{I}} + (\delta P_{\parallel ki} - \delta P_{\perp ki})\hat{\boldsymbol{e}}_{\parallel}\hat{\boldsymbol{e}}_{\parallel}.$$

Forming the dot product of Eq. (3.42) with $\boldsymbol{\xi}_{\perp}^{*}$ and integrating over space yields

$$\delta K_{\perp}(\boldsymbol{\xi}_{\perp}, \boldsymbol{\xi}_{\perp}^{*}) + \delta W_{\perp}(\boldsymbol{\xi}_{\perp}, \boldsymbol{\xi}_{\perp}^{*}) = 0,$$

with $\delta K_{\perp}$ given by Eq. (2.18), and $\delta W_{\perp}$ the sum

$$\delta W_{\perp} = \delta W_{\perp f} + \delta W_{ki}. \tag{3.43}$$

It follows from Eq. (3.41) that $\delta W_{\perp f}$ is described by Eq. (2.12). It will be shown later that

$$\delta W_{ki} = \frac{1}{2}\int d^3x\, \boldsymbol{\xi}_{\perp}^{*} \cdot (\boldsymbol{\nabla} \cdot \underline{\underline{\delta P}}_{ki}) \tag{3.44}$$

does not affect the minimisation of $\delta W_{\perp}$ and subsequent identification of $\boldsymbol{\xi}_{\perp}$. Consequently, we are at liberty to use Bussac's [15] expression for $\delta W_{\perp f}$.

In the following sections, the procedures for calculating δW_{ki} in the external region are derived. The results of this will provide an equation describing the stability boundary of the internal kink mode for thermal ions in the banana regime.

3.3.1 Solution to δf_{ki} in the External Region

In this section the solution to δf_{ki} in the external region is derived. For convenience we write $g \equiv \delta f_{ki}^{e}$, where e denotes external. Equation (3.40) can be expanded in orders of $\omega/\omega_b \ll 1$, where $\omega_b = 2\pi/\tau_b$ is the bounce frequency and τ_b is the bounce time (see Eq. (3.18)). The perturbed kinetic distribution function is expanded as $g = g_0 + g_1$ where

$$\begin{aligned} g_0 &= \hat{g}_0(r)\exp(iS - i\omega t) \\ g_1 &= \hat{g}_1(r,\theta)\exp(iS - i\omega t), \end{aligned}$$

and $g_1/g_0 \sim \omega/\omega_b$. The leading order solution of Eq. (3.40) is

$$\frac{\partial g_0}{\partial l} = 0.$$

Hence, using Eq. (2.35) and noting that the ϕ dependence of g is identical to that of the MHD perturbations implies that:

$$S = q\theta - \phi.$$

The leading order external displacement must now be considered. It was shown in Chapter 2 that ξ_{r0}^{e} corresponds to the top-hat function and from Eq. (2.27), $\xi_{\theta 0}^{e} = i\xi_{r0}^{e}$, where $\xi_{r0}^{e} = \xi_0 \exp(i\theta - i\phi - i\omega t)$. Hence, using $B = B_0(1 - \varepsilon\cos\theta)$, it is clear that

$$\frac{\boldsymbol{\xi}_{\perp 0} \cdot \boldsymbol{\nabla} B}{B} = -\frac{\xi_0}{R_0}\exp(-i\phi - i\omega t). \tag{3.45}$$

To the next order, Eq. (3.40) is:

$$\frac{v_{||}}{R_0 q}\frac{\partial \hat{g}_1}{\partial \theta} - i\hat{g}_0(\omega - \omega_{mdi}) = -i2(\omega - \omega_{*i})\mathcal{E}\frac{\partial f_i}{\partial \mathcal{E}}\left(1 - \frac{\alpha B_0}{2}\right)\frac{\xi_0}{R_0}\exp(-iq\theta). \quad (3.46)$$

To obtain the leading order distribution function $\hat{g}_0$ we must first annihilate $\hat{g}_1$. Since $\omega/\omega_b << 1$ this can be achieved by orbit averaging Eq. (3.46). For passing ions the periodicity property $\oint \frac{\partial x}{\partial \theta} d\theta = 0$ is used. Denoting the passing average $\langle x \rangle_p = \oint x(R_0 q/v_{||})d\theta/\tau_p$, with $\tau_p = \oint (R_0 q/v_{||})d\theta$ the orbit time of passing particles (or transit time), Eq. (3.46) becomes

$$(\omega - \langle \omega_{mdi} \rangle_p)\hat{g}_0 = 2(\omega - \omega_{*i})\mathcal{E}\frac{\partial f_i}{\partial \mathcal{E}}\left(1 - \frac{\alpha B_0}{2}\right)\frac{\xi_0}{R_0}\langle \exp(-iq\theta) \rangle_p .$$

Consider Eq. (3.14) for the orbit time. Since a passing orbit is defined around a loop with $0 \leq \theta \leq 2\pi$,

$$\langle \exp(-iq\theta) \rangle_p = \int_{-\pi/2}^{\pi/2} dx \left(\frac{\cos(2qx)}{\sqrt{1 - k^2 \sin^2 x}}\right) \Bigg/ \int_{-\pi/2}^{\pi/2} \frac{dx}{\sqrt{1 - k^2 \sin^2 x}} ,$$

where $x = \theta/2$ and $k^2 > 1$. The $-i \sin q\theta$ term of $\exp iq\theta$ averages to zero. Also, providing $1 - q$ is small, $< \cos(q\theta) >_p$ is negligible. Hence, we deduce that $\hat{g}_0 \approx 0$ for passing ions.

For trapped ions, Eq. (3.46) is operated with

$$\int_{\theta_b^-}^{\theta_b^+} \frac{d\theta R_0}{v_{||}}$$

separately for $v_{||} > 0$ and $v_{||} < 0$. Quantities evaluated with $v_{||} > 0$ are labelled with a '+'. Conversely, quantities evaluated with $v_{||} < 0$ are labelled with a '$-$' (note that θ_b^+ and θ_b^- are the trapped particle bounce points and are independent of whether $v_{||} > 0$ or $v_{||} < 0$).

The following properties are noted. Since at any one location (e.g. θ_b^+ or θ_b^-) the number of particles with $v_{||} > 0$ must equal the number of particles with $v_{||} < 0$, it follows that

$$\begin{aligned} \delta f_i^+(\theta_b^+) &= \delta f_i^-(\theta_b^+) \\ \delta f_i^+(\theta_b^-) &= \delta f_i^-(\theta_b^-). \end{aligned} \quad (3.47)$$

Thus, $\hat{g}_1^+(\theta_b^+) = \hat{g}_1^-(\theta_b^+)$ and $\hat{g}_1^+(\theta_b^-) = \hat{g}_1^-(\theta_b^-)$. For $v_{||} > 0$:

$$\hat{g}_1^+(\theta_b^+) - \hat{g}_1^+(\theta_b^-) - i\hat{g}_0 \int_{\theta_b^-}^{\theta_b^+} \frac{d\theta R_0 q}{|v_{||}|}\left[\omega - \int_{\theta_b^-}^{\theta_b^+} \frac{d\theta R_0 \omega_{mdi}^+}{|v_{||}|} \Bigg/ \int_{\theta_b^-}^{\theta_b^+} \frac{d\theta R_0}{|v_{||}|}\right] =$$
$$-i2(\omega - \omega_{*i})\mathcal{E}\frac{\partial f_i}{\partial \mathcal{E}}\left(1 - \frac{\alpha B_0}{2}\right)\frac{\xi_0 q}{R_0}\int_{\theta_b^-}^{\theta_b^+} \frac{d\theta R_0 \exp(-iq\theta)}{|v_{||}|}. \quad (3.48)$$

Similarly, for $v_{\|} < 0$

$$\hat{g}_1^-(\theta_b^+) - \hat{g}_1^-(\theta_b^-) + i\hat{g}_0 \int_{\theta_b^-}^{\theta_b^+} \frac{d\theta R_0 q}{|v_{\|}|} \left[\omega - \int_{\theta_b^-}^{\theta_b^+} \frac{d\theta R_0 \omega_{mdi}^-}{|v_{\|}|} \Big/ \int_{\theta_b^-}^{\theta_b^+} \frac{d\theta R_0}{|v_{\|}|} \right] =$$
$$+i2(\omega - \omega_{*i})\mathcal{E}\frac{\partial f_i}{\partial \mathcal{E}} \left(1 - \frac{\alpha B_0}{2}\right) \frac{\xi_0 q}{R_0} \int_{\theta_b^-}^{\theta_b^+} \frac{d\theta R_0 \exp(-iq\theta)}{|v_{\|}|}. \quad (3.49)$$

Subtracting Eqs. (3.48) and (3.49), and noting that a bounce average over ω_{mdi}^+ is identical to ω_{mdi}^-, gives

$$\hat{g}_0 = 2\frac{\omega - \omega_{*i}}{\omega - \langle \omega_{mdi} \rangle} \left(1 - \frac{\alpha B_0}{2}\right) \mathcal{E}\frac{\partial f_i}{\partial \mathcal{E}} \frac{\xi_0}{R_0} \langle \cos q\theta \rangle ,$$

where the angled brackets denote averages over trapped particle space and again the average of the $\sin(-q\theta)$ term of $\exp(-iq\theta)$ is zero. It is convenient to write $\langle \cos q\theta \rangle$ as:

$$\langle \cos q\theta \rangle = \frac{I_q}{K_b}$$

with

$$K_b = \frac{1}{2\pi} \int_{\theta_b^-}^{\theta_b^+} \frac{d\theta}{\sqrt{1 - \alpha B}} , \quad I_q = \frac{1}{2\pi} \int_{\theta_b^-}^{\theta_b^+} \frac{d\theta \cos q\theta}{\sqrt{1 - \alpha B}}. \quad (3.50)$$

Hence, neglecting the much smaller contribution from the passing particles, the perturbed kinetic distribution of energetic thermal ions in the external region is given by:

$$\delta f_{ki}^e = 2\frac{\omega - \omega_{*i}}{\omega - \langle \omega_{mdi} \rangle} \left(1 - \frac{\alpha B_0}{2}\right) \frac{\xi_0 I_q}{R_0 K_b} \mathcal{E}\frac{\partial f_i}{\partial \mathcal{E}} \exp(iq\theta - i\phi - i\omega t). \quad (3.51)$$

3.3.2 δW_{ki} in the External Region

The last section obtained δf_{ki}^e. It is now a simple matter to obtain the perturbed pressure components from it using the definitions:

$$\delta P_{\|ki}^e = m_i \int dv^3 v_{\|}^2 \delta f_{ki}^e \text{ and } \delta P_{\perp ki}^e = m_i \int dv^3 \frac{v_{\perp}^2}{2} \delta f_{ki}^e, \quad (3.52)$$

where the integration is evaluated over all velocity space. The volume element in velocity space can be written in terms of $v_{\|}$ and $v_{\perp}$ as follows:

$$dv^3 = 2\pi v_{\perp}\, dv_{\perp}\, dv_{\|}.$$

It is convenient to define the velocity integration in terms of the constants of motion $\mathcal{E}$ and $\alpha = \mu/\mathcal{E}$:

$$\int dv^3 = 4\pi \int_0^{\infty} d\mathcal{E}\, \mathcal{E} \int_0^{1/B_{\min}} d\alpha \frac{B}{|v_{\|}|}, \quad (3.53)$$

where $v_{\|} = \sqrt{2\mathcal{E}(1-\alpha B)}$. Hence, substituting Eq. (3.51) into Eq. (3.52) yields

$$\left\{ \begin{array}{c} \delta P^e_{\|ki} \\ \delta P^e_{\perp ki} \end{array} \right\} = 2^{7/2}\pi m_i B \frac{\xi_0}{R_0} \int_{1/B\max}^{1/B_{\min}} d\alpha \left(1 - \frac{\alpha B_0}{2}\right)(1-\alpha B)^{1/2} \frac{I_q}{K_b} \left\{ \begin{array}{c} 1 \\ \frac{\alpha B}{2(1-\alpha B)} \end{array} \right\}$$
$$\times \int_0^\infty d\mathcal{E}\, \mathcal{E}^{3/2} \frac{\partial f_i}{\partial \mathcal{E}} \left[\frac{\omega - \omega_{*i}}{\omega - \langle \omega_{mdi} \rangle}\right] \exp(iq\theta - i\phi - i\omega t). \quad (3.54)$$

where $B_{\min} = B_0(1-\varepsilon)$ and $B_{\max} = B_0(1+\varepsilon)$. The pitch angle limit $\alpha = 1/B_{\min}$ corresponds to those particles so deeply trapped on a flux surface r that $v_{\|} = 0$ at all times, i.e. $\theta_b^+ \approx \theta_b^- \approx 0$. The limit $\alpha = 1/B_{\max}$ to those particles with reflection points at the trapped - passing boundary, i.e. $\theta_b^+ \approx \theta_b^- \approx \pi$.

Now consider Eq. (3.44) which describes the kinetic potential energy. The following identities simplify the analysis:

$$\boldsymbol{\xi}_\perp \cdot \left[\boldsymbol{\nabla} \cdot \left(\delta P_\perp \underline{\underline{I}}\right)\right] = \boldsymbol{\xi}_\perp \cdot \boldsymbol{\nabla} \delta P_\perp$$
$$\boldsymbol{\xi}_\perp \cdot \left[\boldsymbol{\nabla} \cdot \left[\left(\delta P_{\|} - \delta P_\perp\right) \hat{\boldsymbol{e}}_{\|} \hat{\boldsymbol{e}}_{\|}\right]\right] = \boldsymbol{\xi}_\perp \cdot \boldsymbol{\kappa} \left(\delta P_{\|} - \delta P_\perp\right).$$

Integrating $\int dx^3\, \boldsymbol{\xi}^*_{\perp 0} \cdot \boldsymbol{\nabla} \delta P^e_{\perp ki}$ by parts and noting that $\boldsymbol{\xi} = 0$ at the plasma edge results in

$$\delta W^e_{ki} = -\frac{1}{2} \int d^3x \left[\delta P^e_{\perp ki} (\boldsymbol{\nabla} \cdot \boldsymbol{\xi}^{e*}_{\perp 0}) - (\delta P^e_{\|ki} - \delta P^e_{\perp ki}) \boldsymbol{\xi}^{e*}_{\perp 0} \cdot \boldsymbol{\kappa}\right]. \quad (3.55)$$

This can be simplified using Eqs. (2.30) and (3.45):

$$\delta W^e_{ki} = -\frac{1}{2} \int d^3x \left(\delta P^e_{\|ki} + \delta P^e_{\perp ki}\right) \frac{\xi_0}{R_0} \exp(i\phi + i\omega t). \quad (3.56)$$

From Eq. (3.54) the sum of the kinetic pressure components can be written:

$$\delta P^e_{\|ki} + \delta P^e_{\perp ki} = 2^{7/2}\pi m_i B \frac{\xi_0}{R_0} \int_{1/B\max}^{1/B_{\min}} d\alpha \left(1 - \frac{\alpha B_0}{2}\right)^2 \frac{1}{\sqrt{1-\alpha B}} \frac{I_q}{K_b}$$
$$\times \int_0^\infty d\mathcal{E}\, \mathcal{E}^{5/2} \frac{\partial f_i}{\partial \mathcal{E}} \left[\frac{\omega - \omega_{*i}}{\omega - \langle \omega_{mdi} \rangle}\right] \exp(iq\theta - i\phi - i\omega t), \quad (3.57)$$

where $1 - \alpha B/2$ has been replaced with $1 - \alpha B_0/2$. This is a good approximation for trapped ions since $\alpha B \approx 1$. Terms involving the trapping condition $1 - \alpha B$ are not approximated; the θ dependence of these terms are crucial.

The volume element

$$dx^3 = 2\pi \frac{R^2}{R_0} r\, dr\, d\theta \quad (3.58)$$

is now required to evaluate Eq. (3.56). Because δW^e_{ki} involves only the top-hat eigenfunction ξ^e_{r0}, the r integration is only required over the range $0 < r < r_1$. The θ integration is only performed over trapped particle space (hence ignoring passing particles and their effects on kinetic stability), i.e. the limits of integration are reduced

from $-\pi, \pi$ to θ_b^-, θ_b^+. Equations (3.56), (3.57) and (3.50) give the kinetic potential energy term

$$\delta W_{ki}^e = -2^{9/2}\pi^3 m_i B_0 R_0 \left(\frac{\xi_0}{R_0}\right)^2 \int_0^{r_1} dr\, r \int_{1/B_{\max}}^{1/B_{\min}} d\alpha \left(1 - \frac{\alpha B_0}{2}\right)^2 \frac{I_q^2}{K_b} \times \int_0^\infty d\mathcal{E}\, \mathcal{E}^{5/2} \frac{\partial f_i}{\partial \mathcal{E}} \left[\frac{\omega - \omega_{*i}}{\omega - \langle\omega_{mdi}\rangle}\right]$$

first derived by Chen *et al* [28] where it was applied to energetic neutral beam ions.

The pitch angle integration is made tractable by changing to the pitch angle variable k^2 defined in Eq. (3.13). Hence, recalling that for trapped particles $\alpha B_0 \approx 1$, one can write

$$d\alpha = -\frac{2r}{B_0 R_0}\, dk^2$$

and subsequently,

$$\delta W_{ki}^e = -2^{7/2}\pi^3 m_i \left(\frac{\xi_0}{R_0}\right)^2 \int_0^{r_1} dr\, r^2 \int_0^1 dk^2\, \frac{I_q^2}{K_b} \int_0^\infty d\mathcal{E}\, \mathcal{E}^{5/2} \frac{\partial f_i}{\partial \mathcal{E}} \left[\frac{\omega - \omega_{*i}}{\omega - \langle\omega_{mdi}\rangle}\right], \tag{3.59}$$

where the pitch angle integration covers all trapped particles, from those deeply trapped with $k^2 = 0$ to those marginally trapped with $k^2 = 1$. Also, following the analysis of Section 3.1.6, I_q and K_b can be defined in terms of the new pitch angle k^2:

$$K_b(k^2) = \frac{1}{\pi}\sqrt{\frac{2}{\varepsilon}} K(k^2)\ , \quad I_q(r, k^2) = \frac{1}{\pi}\sqrt{\frac{2}{\varepsilon}} \int_0^{\frac{\pi}{2}} \frac{\cos[2q \sin^{-1}(\sqrt{k^2}\sin\phi)]}{\sqrt{1 - k^2 \sin^2\phi}} d\phi \tag{3.60}$$

I_q cannot be described in terms of Elliptic Integrals unless one expands about $q = 1$. This expansion is treated in Chapter 4 which describes the fast ion response. The bounce averaged magnetic drift frequency $\langle\omega_{mdi}\rangle$ can be defined in terms of $\mathcal{E}$, k^2 and r by referring to Eq. (3.23) and noting that for trapped ions, $\mu \approx \mathcal{E}/B_0$. Hence,

$$\langle\omega_{mdi}\rangle = \frac{2m_i q(r)}{Zer B_0 R_0} \mathcal{E} \left[F_1(k^2) + 2s(r) F_2(k^2)\right], \tag{3.61}$$

where $F_1(k^2)$ and $F_2(k^2)$ are defined in Eq. (3.24).

We should now consider the size δW_{ki}^e in terms of the inverse aspect ratio. The high frequency limit ($\omega \gg \omega_{*i}$ and $\omega \gg \langle\omega_{mdi}\rangle$) of Eq. (3.59) corresponds to the Kruskal - Oberman regime [22]. Such a limit was employed in Ref. [24] and the resulting internal kink dispersion relation is shown in Eq. (2.2). In this analysis $\mu_1 \approx 1.1$ is obtained by approximating I_q, K_b and the pitch angle integration. The factor $\sqrt{2\varepsilon}$ represents the trapped fraction of thermal ions in the banana regime. The relative size of Bussac's [15] fourth order fluid potential energy term δW_f and the Kruskal - Oberman limit of Eq. (3.59) is:

$$\frac{\delta W_f}{\delta W_{ki}^e} \sim \frac{\varepsilon_1^{3/2}}{\beta_i}, \tag{3.62}$$

where β_i is defined in Eq. (2.3). Now, since $\beta \sim \varepsilon_1^2$, then $\varepsilon_1^2 \lesssim \beta_i \lesssim \varepsilon_1$. The exact order of β_i relative to β depends on the pressure profile. In any case, Eq. (3.62) indicates that δW_{ki}^e and Bussac's [15] fourth order fluid term are approximately the same order.

It is now clear that the minimisation of fluid terms δW_0 and δW_2, and subsequent identification of $\boldsymbol{\xi}_0$, is not affected by kinetic effects. Moreover, to fourth order in inverse aspect ratio, δW_{ki}^e only depends on $\boldsymbol{\xi}_0$. The higher order corrections $\delta W_{ki}^e(\boldsymbol{\xi}_1, \boldsymbol{\xi}_2)$ cannot compete with the fluid terms. Thus, Bussac's minimised fluid potential energy is still valid.

In an ideal plasma with $\omega > \omega_{*pi}$, the sign of the total external potential energy describes the stability boundary of the internal kink mode for a plasma with thermal ions in the banana regime. Instability corresponds to

$$\delta W_f + \Re\{\delta W_{ki}^e\} < 0. \tag{3.63}$$

More detailed information, namely the dispersion relation and subsequent growth rates, are derived in Chapter 4.

3.4 Summary

The stability boundary of the internal kink mode has been extended to include the effects of energetic thermal ions. Using drift kinetic theory this has been achieved by calculating the perturbed distribution function in the external region and subsequently the modifications to the MHD energy principle. The review chapters of 1, 2 and 3, provide a basis for the original analysis contained in Chapter 4. Here the kinetic effects of thermal ions are considered in the singular layer and a modified dispersion relation is obtained. Furthermore, the analysis is extended to describe the kinetic effects of ICRH heated minority ions.

Chapter 4

Extensions to the Internal Kink Mode and Applications to Energetic Thermal ions and Minority ions Heated with ICRH

In the previous chapter the ideal internal kink mode stability boundary for thermal ions in the banana regime was obtained. There it was shown that the kinetic effects are identical to those first identified by Chen *et al* [28] for NBI populations.

In this chapter the kinetic modifications to the energy principle are extended to the singular layer, and as a result, a self-consistent dispersion relation is obtained. The stability boundary is modified in such a way that it can describe the internal kink mode stability for plasmas with ICRH minority ions. Different regimes, corresponding to differing heating conditions, are then examined as a preclude to analysing specific JET discharges in Chapter 5.

4.1 Internal Kink Stability with Thermal Ions in the Banana Regime

Equation (3.63) is a rather restrictive gauge of internal kink mode stability for the following reasons. First it requires $\omega > \omega_{*pi}$, second it does not provide information regarding the growth rate, and third it requires that resistive effects are negligible. Moreover, the fact that δW^e_{ki} is a function of ω means that in general δW^e_{ki} cannot be

evaluated without first solving a dispersion relation in ω.

Dispersion relations describing the internal kink stability for kinetic thermal ions have been employed elsewhere [44, 45]. However, in the analysis of Fogaccia and Romanelli [44], or for example, Antonsen and Bondeson [45], kinetic effects in the singular layer were neglected. In this chapter these additional kinetic effects are evaluated for the first time by following a procedure similar to that used for the external region, i.e. δf^s_{ki} and δW^s_{ki} are evaluated.

Before calculating the kinetic terms in the singular layer, the relevant frequency regime must be identified. In Ref. [47], a regime was employed with $\omega \lesssim \omega_{ti}$, where $\omega_{ti} = 2\pi/\tau_p|_{k^2\to\infty}$ is the transit frequency of passing thermal ions and τ_p the passing orbit time defined in Eq. (3.15). Using this ordering Romanelli *et al* [47] evaluated the term in the dispersion relation corresponding to the kinetic effects of thermal ions in the singular layer. However, in this thesis the relevant ordering is $\omega \sim \omega_{*pi} \ll \omega_{ti}$. Furthermore, to be consistent with the analysis of Chapter 3, the drift kinetic equation will be expanded in small ω/ω_{bi} and ω/ω_{pi}, where $\omega_{bi} = 2\pi/\tau_b$ is the bounce frequency and $\omega_{pi} = 2\pi/\tau_p$ the passing orbit frequency. Subsequently, the calculations derived in the following sections serves to correct an analysis in which Mikhailovskii [46] assumed the relevant scaling $\omega/\omega_{ti} \ll 1$. In a similar vein to that of Ref. [47] it is also assumed that ion-ion collisions are negligible. Such a regime requires $\omega_{*pi} \gg \nu_{ii}$, with ν_{ii} the frequency of ion-ion collisions. Comparisons between the various competing frequencies will be discussed in greater detail in Chapter 6.

4.1.1 Solution to δf_{ki} in the Singular Layer

The analysis of the singular layer differs from that of the external region because of the following distinguishing characteristics:
1) $\xi^s_\theta \approx ir\partial\xi^s_r/\partial r \gg \xi^s_r$.
2) $\omega_{mdi}(r_1)/\omega_{*i}(r_1) \sim \varepsilon_1$.
The first of these follows from the discontinuity of the 'top-hat' eigenfunction at r_1 and from $\boldsymbol{\nabla}\cdot\boldsymbol{\xi}^e_{\perp 0} = 0$. The second follows from considering the relative sizes of ω_{mdi} and ω_{*i} at the layer. For simplicity we begin by considering the most deeply trapped ions ($k^2 = 0$) with kinetic energy $m_i\mathcal{E} = 5T_i/2$. For such ions

$$\frac{\langle\omega_{mdi}\rangle}{\omega_{*i}} = -\frac{5}{2R_0}\frac{P_i}{P_i'},$$

where $' \equiv \partial/\partial r$. Describing the pressure profile as the parabolic form $P_i \propto 1-(r/a)^2$ yields

$$\frac{\langle\omega_{mdi}\rangle}{\omega_{*i}} = \frac{5}{4}\left(\frac{a}{R_0}\right)\left(\frac{a}{r}\right)\left(1-\left(\frac{r}{a}\right)^2\right). \tag{4.1}$$

Hence $\langle\omega_{mdi}\rangle/\omega_{*i} \gg 1$ for $r \ll r_1$, and $\langle\omega_{mdi}\rangle/\omega_{*i} \sim a/R_0$ for $r = r_1 \approx a/2$. Less deeply trapped ions and many passing ions give rise to a smaller ratio than that defined in Eq. (4.1). Hence, since $\omega \sim \omega_{*pi} \sim \omega_{*i}$, the magnetic drift terms contained in the drift kinetic equation are ignored in the singular layer.

The kinetic equation describing energetic thermal ions is now applied to the singular layer. First consider the last term in Eq. (3.40). Since $\xi_\theta^s \gg \xi_r^s$, it follows that $\boldsymbol{\xi}_\perp^s \cdot \boldsymbol{\nabla} B = (\xi_\theta^s/r)\partial B/\partial\theta$. Also, from the conservation of μ and $\mathcal{E}$ it follows that $(v_\parallel^2 + \mu B)\partial B/\partial\theta = -B^2 v_\parallel \partial(v_\parallel/B)/\partial\theta$. Hence in the singular layer,

$$(v_\parallel^2 + \mu B)\frac{\boldsymbol{\xi}_\perp^s \cdot \boldsymbol{\nabla} B}{B} = -B v_\parallel \frac{\xi_\theta^s}{r}\frac{\partial}{\partial\theta}\left(\frac{v_\parallel}{B}\right). \tag{4.2}$$

The poloidal displacement takes the form $\xi_\theta^s = \hat{\xi}_\theta^s(r)\exp(i\theta - i\phi - i\omega t)$. In concordance with the external region, the θ dependence of δf_{ki}^s is not in general identical to that of $\boldsymbol{\xi}$. Identifying $h \equiv \delta f_{ki}^s$, we are at liberty to let

$$h = \hat{h}(r,\theta)\exp(i\theta - i\phi - i\omega t). \tag{4.3}$$

Hence, from Eqs. (2.35), (4.2), (4.3) and using $\omega_{*i} \sim \omega \gg \omega_{mdi}$, Eq. (3.40) becomes

$$\frac{v_\parallel}{Rq}\left[\frac{\partial}{\partial\theta} + i(1-q)\right]\hat{h} - i\omega\hat{h} = i(\omega - \omega_{*i})\frac{\partial f_i}{\partial\mathcal{E}}\frac{\hat{\xi}_\theta^s}{r}\frac{v_\parallel}{R}\frac{\partial}{\partial\theta}(Rv_\parallel), \tag{4.4}$$

where we have used the relation $B\partial R/\partial\theta = -R\partial B/\partial\theta$, that results from the $1/R$ dependence of B.

Since $q \approx 1$ in the singular layer, the $1-q$ term on the left hand side of Eq. (4.4) is neglected. In accordance with the external region, the kinetic equation is expanded in orders of $\omega/(2\pi/\tau)$. The leading order kinetic equation is

$$\frac{v_\parallel}{Rq}\frac{\partial\hat{h}_0}{\partial\theta} = i(\omega - \omega_{*i})\frac{\partial f_i}{\partial\mathcal{E}}\frac{\hat{\xi}_\theta^s}{r}\frac{v_\parallel}{R}\frac{\partial}{\partial\theta}(Rv_\parallel)$$

and therefore, the leading order solution is

$$\hat{h}_0 = i(\omega - \omega_{*i})\frac{q\hat{\xi}_\theta^s}{r}\frac{\partial f_i}{\partial\mathcal{E}}Rv_\parallel + \overline{h}_0,$$

where $\overline{h}_0$ is independent of θ.

To determine $\overline{h}_0$ we proceed to the next order:

$$\frac{v_\parallel}{Rq}\frac{\partial\hat{h}_1}{\partial\theta} = i\omega\hat{h}_0, \tag{4.5}$$

which, in conjunction with the leading order solution gives

$$\frac{v_\parallel}{Rq}\frac{\partial\hat{h}_1}{\partial\theta} = -\omega(\omega - \omega_{*i})\frac{q\hat{\xi}_\theta^s}{r}\frac{\partial f_i}{\partial\mathcal{E}}Rv_\parallel + i\omega\overline{h}_0, \tag{4.6}$$

A solution for $\overline{h}_0$ is obtained by annihilating $\hat{h}_1$ separately for passing and trapped ions.

Transit averaging Eq. (4.6) over passing particle space annihilates $\hat{h}_1$ directly to give

$$\overline{h}_0(\text{pass}) = -i(\omega - \omega_{*i})\frac{q\hat{\xi}_\theta^s}{r}\frac{\partial f_i}{\partial\mathcal{E}}\oint_p d\theta\, R^2 \Big/ \oint_p \frac{d\theta\, R}{v_\parallel}$$

Now consider trapped ions by following the procedure employed in the external region. Defining

$$\Lambda = -\omega(\omega - \omega_{*i})\frac{q\,\hat{\xi}_\theta^s}{r}\frac{\partial f_i}{\partial \mathcal{E}}R,$$

the first order kinetic equations for $v_\| > 0$ and $v_\| < 0$ are respectively

$$\frac{\left|v_\|\right|}{Rq}\frac{\partial \hat{h}_1^+}{\partial \theta} = -\Lambda\left|v_\|\right| + i\omega\hat{h}_0^+$$
$$-\frac{\left|v_\|\right|}{Rq}\frac{\partial \hat{h}_1^-}{\partial \theta} = \Lambda\left|v_\|\right| + i\omega\hat{h}_0^-.$$

Operating on these equations with $\int_{\theta_b^-}^{\theta_b^+}\frac{d\theta\,qR}{\left|v_\|\right|}$ for both $v_\| > 0$ and $v_\| < 0$ respectively obtains,

$$\hat{h}_1^+(\theta_b^+) - \hat{h}_1^+(\theta_b^-) = -\Lambda\int_{\theta_b^-}^{\theta_b^+} d\theta\,R + i\omega q\overline{h}_0^+\int_{\theta_b^-}^{\theta_b^+}\frac{d\theta\,R}{\left|v_\|\right|} \tag{4.7}$$

$$-\left[\hat{h}_1^-(\theta_b^+) - \hat{h}_1^-(\theta_b^-)\right] = \Lambda\int_{\theta_b^-}^{\theta_b^+} d\theta\,R + i\omega q\overline{h}_0^-\int_{\theta_b^-}^{\theta_b^+}\frac{d\theta\,R}{\left|v_\|\right|}. \tag{4.8}$$

Equation (3.47) indicates that $\hat{h}_1^+(\theta_b^+) = \hat{h}_1^-(\theta_b^+)$, $\hat{h}_1^+(\theta_b^-) = \hat{h}_1^-(\theta_b^-)$ and $\overline{h}_0^+ = \overline{h}_0^- = \overline{h}_0$. Hence, summing Eqs (4.7) and (4.8) gives

$$\overline{h}_0(\text{trap}) = 0$$

Therefore, the leading order kinetic distribution function is

$$\hat{h}_0 = i(\omega - \omega_{*i})\frac{q\,\hat{\xi}_\theta^s}{r}\frac{\partial f_i}{\partial \mathcal{E}}Rv_\|\mathcal{X}, \tag{4.9}$$

with

$$\mathcal{X} = \begin{cases} 1 & \text{trapped ions} \\ 1 - \left(\oint_p d\theta\,R^2\right)\Big/\left(Rv_\|\oint_p\frac{d\theta\,R}{v_\|}\right) & \text{passing ions.}\end{cases}$$

We note at this point that $\hat{h}_0$ is odd in $v_\|$. This means that $\hat{h}_0$ is capable of describing the parallel ion fluid velocity

$$\delta u_{i\|} = \frac{2\pi}{n_i}\int_{-\infty}^{\infty} dv_\perp\,v_\perp\int_{-\infty}^{\infty} dv_\|\,\left(v_\|h_0\right) \tag{4.10}$$

and subsequently the parallel inertia.

4.1.2 δW_{ki} in the singular Layer

It is now necessary to evaluate the extent to which kinetic effects in the layer modify the internal kink stability. This is achieved through evaluating δW^s_{ki}, the kinetic potential energy, at the singular layer.

It follows from Eqs. (3.55) and (2.30) that δW^s_{ki} can be defined as:

$$\delta W^s_{ki} = \frac{1}{2}\int dx^3 \left(\delta P^s_{\parallel ki} + \delta P^s_{\perp ki}\right) \frac{\boldsymbol{\xi}^{s*}_{\perp}\cdot\boldsymbol{\nabla} B}{B}$$

with

$$\delta P^s_{\parallel ki} + \delta P^s_{\perp ki} = m_i \int dv^3 \left[v^2_{\parallel} + \mu B\right] h.$$

Note that δW^s_{ki} is non-zero when h is even in $v_{\parallel}$. The largest even component of h is h_1. Hence, from Eqs. (4.2), (3.53) and (3.58),

$$\delta W^s_{ki} = -m_i 4\pi^2 R_0 B_0^2 \int_s dr \int_0^{\infty} d\mathcal{E}\, \mathcal{E} \int_0^{1/B_{\min}} d\alpha \oint d\theta\, \xi^{s*}_{\theta} h_1 \frac{\partial}{\partial\theta}\left(\frac{v_{\parallel}}{B}\right),$$

where the contour integration in θ is defined appropriately for either passing or trapped ions in conjunction with the integration over α. Integrating the poloidal integral by parts and noting that $\xi^{s*}_{\theta} h_1 = \hat{\xi}^s_{\theta}\hat{h}_1$ gives

$$\delta W^s_{ki} = m_i 4\pi^2 R_0 B_0^2 \int_s dr\, \hat{\xi}^s_{\theta} \int_0^{\infty} d\mathcal{E}\, \mathcal{E} \int_0^{1/B_{\min}} d\alpha \oint d\theta \left(\frac{v_{\parallel}}{B}\right) \frac{\partial \hat{h}_1}{\partial\theta}.$$

Referring to Eq. (4.5), note that δW^s_{ki} can be written in terms of the leading order distribution function $\hat{h}_0$. Hence, substituting Eq. (4.9) obtains

$$\delta W^s_{ki} = -m_i \pi R_0 B_0 \gamma_I^2 \int_s dr\, \frac{(q\hat{\xi}^s_{\theta})^2}{r} \oint d\theta \left(\frac{R}{B}\right)^2 \left[4\pi B \int_0^{\infty} d\mathcal{E}\, \mathcal{E} \frac{\partial f_i}{\partial \mathcal{E}} \int_0^{1/B_{\min}} d\alpha\, v_{\parallel} - 4\,\pi \left(\frac{B}{R}\right) \int_0^{\infty} d\mathcal{E}\, \mathcal{E} \frac{\partial f_i}{\partial \mathcal{E}} \int_0^{1/B_{\max}} d\alpha \frac{\oint_p d\theta\, R^2}{\oint_p d\theta\, R/v_{\parallel}}\right], \quad (4.11)$$

where subscript 'p' denotes passing space and the ideal relation $\gamma_I^2 = -\omega(\omega - \omega_{*pi})$ has been used. The pressure weighted diamagnetic frequency appears as a consequence of the energy integration. To see this more clearly one can write

$$\omega_{*pi} = \left(\int_0^{\infty} d\mathcal{E}\, \mathcal{E}^{3/2} f_i\, \omega_{*i}\right) \Big/ \int_0^{\infty} d\mathcal{E}\, \mathcal{E}^{3/2} f_i\ ,$$

which easily reduces to Eq. (2.54) upon identifying f_i with the Maxwellian distribution

$$f_i = n_i \left(\frac{m_i}{2\pi T_i}\right)^{3/2} \exp\left(\frac{-m_i\mathcal{E}}{T_i}\right).$$

The first term in the square brackets of Eq. (4.11) is evaluated over all particle space and referring to Eq. (3.53) it is clear that it is proportional to the ion density

$$n_i = \int dv^3\, f_i.$$

The remaining term is much more complicated. Progress is made by transforming to a new pitch angle variable $y = 1/k^2$, where k^2 is defined in Eq. (3.13). It can now be seen that the integral $\oint_p d\theta\, R/v_{\|}$ gives rise to an elliptic integral of the first kind $K(y)$. Also evaluating the energy integral and substituting $\rho = m_i n_i$ one can show that

$$\delta W^s_{ki} = 2\pi^2 R_0 \gamma_I^2 \int_s dr\, r (q\hat{\xi}^s_\theta)^2 \rho \frac{1}{\varepsilon^2} \left[\underbrace{\int_{-\pi}^{\pi} \frac{d\theta\, R^4}{2\pi R_0^4}}_{1+3\varepsilon^2} - \underbrace{\left(\int_{-\pi}^{\pi} \frac{d\theta\, R^2}{2\pi R_0^2} \right)^2}_{1+\varepsilon^2} \mathcal{Q} \right] \tag{4.12}$$

where

$$\mathcal{Q} = \frac{3\pi}{\sqrt{2}} \int_0^1 \frac{dy\, \varepsilon^{3/2}}{[y(1-\varepsilon) + 2\varepsilon]^{5/2} K(y)} \tag{4.13}$$

Referring to Eq. (2.42) one might naively believe that $\delta K^s / \delta W^s_{ki} \sim \varepsilon^2$. That is the kinetic potential energy in the singular layer is much larger than the fluid inertia and thus provides a very large inertial enhancement. However, it will become clear that cancellation occurs in Eq. (4.12) and for this reason $\mathcal{Q}$ must be evaluated carefully.

Defining $\lambda = 2\varepsilon/(1-\varepsilon)$ and integrating (4.13) by parts obtains

$$\mathcal{Q} = -\frac{\pi}{2} \frac{1}{(1-\varepsilon)} \left(\left[\frac{\lambda^{3/2}}{(y+\lambda)^{3/2} K(y)} \right]_0^1 + \mathcal{I} \right),$$

where

$$\mathcal{I} = \int_0^1 \frac{dy\, \lambda^{3/2}\, K(y)'}{(y+\lambda)^{3/2} K(y)^2},$$

and $K(y)' = dK(y)/dy$. Since $1/K(1) = 0$ and $1/K(0) = 2/\pi$ then

$$\mathcal{Q} = \frac{1}{1-\varepsilon} \left(1 - \frac{\pi}{2} \mathcal{I} \right).$$

$\mathcal{I}$ cannot yet be evaluated explicitly in terms of the parameter λ. Progress is made by writing

$$\mathcal{I} \equiv \lambda^{3/2} \left[\int_0^1 \left(\frac{K(y)'}{K(y)^2} - \mathcal{S}(y) \right) \frac{dy}{(y+\lambda)^{3/2}} + \int_0^1 \frac{dy\, \mathcal{S}(y)}{(y+\lambda)^{3/2}} \right], \tag{4.14}$$

where $\mathcal{S}$ is chosen in such a way that the second integral can be evaluated analytically and, if one takes $\lambda = 0$, the first integral converges at $y = 0$. Hence $\mathcal{S}(0) = K(0)'/K(0)^2$ and its local dependence on y is obtained using the expansion

$$K(y) = \frac{\pi}{2} \left[1 + \frac{1}{4} y + \frac{9}{64} y^2 + ... \right].$$

Truncating $\mathcal{S}$ beyond y^2 gives

$$\mathcal{S} = \frac{1}{2\pi} \left[1 + \frac{5}{8} y \right],$$

and so the second integral of Eq. (4.14) is

$$\lambda^{3/2}\int_0^1 \frac{dy\,\mathcal{S}(y)}{(y+\lambda)^{3/2}} = \frac{2}{\pi}\left[\varepsilon - \frac{3\sqrt{2}}{8}\varepsilon^{3/2}\right] + O(\varepsilon^2).$$

The first integral of Eq. (4.14) can be simplified by noting that the integrand is zero for $y = 0$ and very small for $y \sim \lambda$. Hence,

$$\mathcal{I} = \frac{2}{\pi}\left[\varepsilon - \frac{3\sqrt{2}}{8}\varepsilon^{3/2} + (2\varepsilon)^{3/2}\int_0^1 \left(\frac{K(y)'}{K(y)^2} - \mathcal{S}(y)\right)\frac{dy}{y^{3/2}}\right] + O(\varepsilon^2)$$

In its present form the remaining integral still cannot be integrated accurately within the precision of numerical routines. The difficulty now lies in the vicinity of $y = 1$. However, using the result

$$\lim_{y\to 1}\{K(y)\} = \frac{1}{2}\ln\left(\frac{16}{1-y}\right),$$

one can write

$$\int_0^1 \left(\frac{K(y)'}{K(y)^2} - \mathcal{S}(y)\right)\frac{dy}{y^{3/2}} = \lim_{y\to 1}\left[\int_0^{1-\delta}\left(\frac{K(y)'}{K(y)^2} - \mathcal{S}(y)\right)\frac{dy}{y^{3/2}} + \frac{2}{\ln(16/\delta)}\right]. \quad (4.15)$$

which, in practice, can be evaluated accurately to 3 decimal places for $\delta = 1\times 10^{-3}$. The result leads to the approximate solution

$$\mathcal{I} = \frac{2}{\pi}\left[\varepsilon + 1.6\varepsilon^{3/2}\right] + O(\varepsilon^2).$$

We now observe that terms in $\mathcal{Q}$ of order ε cancel to leave :

$$\mathcal{Q} = 1 - 1.6\varepsilon^{3/2} + \mathcal{Q}_2\varepsilon^2,$$

where $\mathcal{Q}_2 \sim 1$. Upon substituting $\mathcal{Q}$ into Eq. (4.12) it is clear that the leading order term is also cancelled to give

$$\delta W^s_{ki} = 2\pi^2 R_0\gamma_I^2\int_s dr\, r(q\hat{\xi}^s_\theta)^2\rho\frac{1}{\varepsilon^2}\left[1.6\varepsilon^{3/2} + 2\varepsilon^2 - \mathcal{Q}_2\varepsilon^2\right]. \quad (4.16)$$

The dispersion relation at the singular layer is given by

$$D^s = \delta K^s_{\perp i} + \delta W^s_{ki} + \delta W^s_{fi}.$$

Referring to the perpendicular component of Eq. (2.42) it is now straightforward to show that

$$\delta K^s_{\perp i} + \delta W^s_{ki} = 2\pi^2 R_0\gamma_I^2\int_s dr\,\rho r\left(r\frac{\partial\hat{\xi}^s_r}{\partial r}\right)^2(1+\Delta),$$

where

$$\Delta = q^2\left(\frac{1.6}{\sqrt{\varepsilon}} + 2 - \mathcal{Q}_2\right)$$

The leading order term of Δ is $q^2 1.6/\sqrt{\varepsilon}$, and represents a correction to the original inertial enhancement calculated by Mikhailovskii [46]. Reference [46] contains a simplified analysis in which perturbations in the long-mean-free-path limit are wrongly assumed to be isotropic. As a result, solving Eq. (4.13) of Ref. [46] yields $\Delta = 0.45/\sqrt{\varepsilon}$. If in addition one wishes to include the contribution arising from the poloidal inertia (identified with the '1' in $(1 + \Delta)$ above) one must also keep terms of order ε^2 appearing inside the square brackets of Eq. (4.16), i.e. the factors $\mathcal{Q}_2$ and 2 in Δ. The term $2q^2$ corresponds to the inertial enhancement observed in ideal MHD, i.e. the parallel inertia. Clearly, if one wishes to maintain this term together with that arising from the poloidal inertia one must also calculate $\mathcal{Q}_2$. Hastie [60] has shown that, to the required order of accuracy, $\mathcal{Q}_2$ necessarily contains effects of the Shafranov shift, and where applicable flux surface shaping. The resulting pitch angle integrals are too complicated to include here. The result, valid at r_1, is

$$\Delta = \left(0.5 + \frac{1.6}{\sqrt{\varepsilon_1}}\right), \tag{4.17}$$

and following the analysis contained in Section 2.4.5 it is now straightforward to show that

$$D^s = 2\pi R_0 \varepsilon_1^2 s_1 \frac{B_0^2}{\mu_0} \xi_0^2 \frac{\gamma_I \sqrt{1+\Delta}}{\omega_A}. \tag{4.18}$$

It is interesting to contrast the singular dispersion relations of ideal MHD, collisionless MHD and drift kinetic theory. In ideal MHD it was shown that a small inertial enhancement exists as a consequence of the parallel inertia, i.e. in the above formalism, $\Delta = 2$. In collisionless MHD the parallel inertia does not enter the dispersion relation, and thus $\Delta = 0$. It has been demonstrated in this section that the enhancement in the kinetic regime does not arrive from the parallel inertia, but rather, from the kinetic potential energy δW^s_{ki}. In principle, however, one can calculate $\delta K^s_{\|}$. The analysis used to obtain both $\delta K^s_{\|}$ and δW^s_{ki} is very similar. Indeed, until $\delta K^s_{\|}$ had been evaluated accurately it was thought that they were identical. The consequence of this would have been that the inertial enhancement observed in drift kinetic theory would have the same underlying source as in ideal MHD, i.e. the parallel inertia. However, this is not the case and the qualitative information that might be hoped for does not follow. Referring to Eq. (4.10), and following the analysis used in the calculation for δW^s_{ki}, it can now be shown that

$$\delta K^s_{\|} = -2\pi^2 R_0 (\omega - \omega_{*pi})^2 \int_s dr\, \rho r \left(r \frac{\partial \hat{\xi}^s_r}{\partial r}\right)^2 q^2 (2 + (1.6)^2 \varepsilon - 4(1.6)\varepsilon^{3/2}).$$

Hence, in the limit $\omega/\omega_{*pi} \gg 1$ the leading order term in $\delta K^s_{\|}$ corresponds exactly to the parallel inertia observed in ideal MHD. It is clear that the terms arising as a result of the kinetic effects of thermal ions are an order of magnitude smaller. This is in fact contrary to the ordering of terms in δW^s_{ki}.

4.1.3 The Dispersion Relation

The kinetic modifications of the internal kink mode have been derived in Chapter 3 and in the previous sections. In this section the various modifications are brought together to form a dispersion relation that is capable of describing the stability of the internal kink mode with thermal ions in the banana regime. From Eqs. (2.40) and (3.43), the dispersion relation of the external region is

$$D^e = \delta W_f^e + \delta W_{ki}^e,$$

where δW_f^e is the minimised MHD potential energy (e.g. Bussac's) and δW_{ki}^e is defined in Eq. (3.59). The ideal dispersion relation corresponding to the singular region is given in Eq. (4.18). Hence, the total dispersion relation $D = D^s + D^e = 0$ in the ideal limit is

$$-i\left.\frac{\sqrt{\omega(\omega-\omega_{*pi})}}{\omega_A}\right|_{r_1} + \varepsilon_1^2 \frac{3\pi}{s_1\sqrt{1+\Delta}}\left[\delta\hat{W}_f + \delta\hat{W}_{ki}(\omega)\right] = 0, \tag{4.19}$$

where the superscript 'e' has been dropped from $\delta\hat{W}_f$ and $\delta\hat{W}_{ki}$.

Although it has been possible to modify the internal kink mode dispersion relation to include kinetic effects, it is not a trivial matter to identify the exact kink mode growth rate from Eq. (4.19) for a given equilibrium. This stems from the fact that δW_{ki} is a function of ω and complicated root-finding routines must be used to identify distinct solutions. Furthermore, referring to Eq. (3.59) it is clear that a pole exists at $\omega = \langle\omega_{mdi}\rangle$. Hence, even if the mode is purely oscillatory ($\gamma = \Im\{\omega\} = 0$), $\delta\hat{W}_{ki}$ has an imaginary part arising as a consequence of the $\omega = \langle\omega_{mdi}\rangle$ resonance. Of course in general both ω and $\delta\hat{W}_{ki}$ are complex.

Authors have found various means of simplifying the kinetic potential energy. These usually involve simplifying the pitch angle dependence of $\langle\omega_{mdi}\rangle$ and making assumptions about the magnitude of ω with respect to the ion diamagnetic frequency or magnetic drift frequency. In Chapter 5 simplifications are made concerning the kinetic potential energy arising from an ICRH heated minority population. Here it is found that most ions conform to $\langle\omega_{mdh}\rangle \gg \omega$ and $\omega_{*i} \gg \omega$. This allows analytical integration over $\mathcal{E}$ and a simplified evaluation of the remaining pitch angle and radial integrals. Other authors have employed simplified minority ion distribution functions, some of which have been discussed briefly in the Historical Review.

In Chapter 6, Eq. (4.19) is extended further to include the effects of the equilibrium electric field. In this chapter the form of $\delta\hat{W}_{ki}$ is not simplified and the ideal dispersion relation is solved exactly.

4.2 Internal Kink Stability with ICRH Heated Minority Ions

The last section presented a study relating to the effects of energetic thermal ions on the internal kink mode. The results from this are now used to construct the theory

required to describe the effects that minority ions have on the mode. This thesis concentrates on energetic minority ions heated with ICRH. Such heating typically introduces anisotropic velocity distributions which further complicates the analysis. Four cases are discussed in the following sections, each with differing ICRH heating characteristics. For simplicity it is assumed that the thermal ions are collisional, although, it is a straightforward matter to include the kinetic effects of thermal ions if required.

4.2.1 ICRH Heating with $P_{\perp h} \sim P_{\parallel h} \sim P_c$

If the minority ions are heated in such a way that their contribution to the plasma pressure is isotropic (i.e. $P_{\perp h} \sim P_{\parallel h} \sim P_h$) and competes with the core pressure $P_c = P_e + P_i$, the analysis is easily modified as follows. The hot minority ions enter the problem in exactly the same way as collisionless thermal ions. For the fluid contribution, one cannot distinguish between the electrons, the thermal ions or the energetic minority ions; they all have associated with them a pressure which collectively combine to form the total plasma pressure $P = P_c + P_h$. Hence, in the case of Bussac's stability calculation, the fluid term is approximately given by

$$\delta\hat{W}_f = (1 - q_0)\left((\beta_p^c)^2 - \beta_p^2\right),$$

where β_p is defined in Eq. (2.1) with P the total plasma pressure $P = P_c + P_h$.

It is important to note that $\delta\hat{W}_f$ depends non linearly on the total pressure. This means that the hot ion contribution to the fluid stability is coupled with the stability of the core plasma, i.e. one cannot write $\delta\hat{W}_f = \delta\hat{W}_{fc} + \delta\hat{W}_{fh}$. However, if $P_h \sim \varepsilon P_c$, the potential energy contribution of the hot ions to the fluid stability is additive.

The remaining perturbed pressure component is δP_{kh}. Referring to Eq. (3.59) and applying it to the hot minority ions in the external region gives

$$\delta W_{kh}^e = -2^{7/2}\pi^3 m_h \left(\frac{\xi_0}{R_0}\right)^2 \int_0^{r_1} dr\, r^2 \int_0^1 dk^2\, \frac{I_q^2}{K_b} \int_0^\infty d\mathcal{E}\, \mathcal{E}^{5/2} \frac{\partial f_h}{\partial \mathcal{E}} \left[\frac{\omega - \omega_{*h}}{\omega - \langle\omega_{mdh}\rangle}\right],$$

where m_h is the hot ion mass, f_h the distribution function and ω_{*h} and $\langle\omega_{mdh}\rangle$ are the hot ion diamagnetic and magnetic drift frequencies respectively.

The minority ions also have have associated with them a kinetic potential energy contribution in the singular layer. However, the analysis presented in 3.3.3 and 3.3.4 cannot be applied to a highly energetic population heated with ICRH. Such ions have much larger Larmor radii than those of thermal ions in the banana regime and thus will not be confined to the comparatively narrow singular layer for a significant time. In any case, kinetic effects in the layer do not alter the ideal stability boundary, which only requires the sign of potential energy of the external region. Dropping the 'e' notation, one can write,

$$\delta W(\omega) = \delta W_f + \delta W_{kh}(\omega), \tag{4.20}$$

where instability corresponds to $\Re\{\delta W(\omega)\} < 0$ in an ideal regime with $\omega > \omega_{*pi}$.

As Eq. (4.20) stands, it is non-trivial to evaluate the sign of $\Re\{\delta W\}$. This is because δW_{kh} is a function of ω and thus formally the sign of δW can only be obtained after having identified ω from the internal kink dispersion relation. However, in high power ICRH discharges, $\omega_{*h} \gg \omega$ and $\langle\omega_{mdh}\rangle \gg \omega$ for most minority ions. Hence for such discharges, the dependence of δW_{kh} on ω is weak and the resulting $\omega = 0$ solution provides a good approximation. Referring to Eqs (3.34), (3.60), (3.61) and (3.24) one can show that

$$\delta W_{kh}(0) = -2^{7/2}\pi^3 m_h R_0 \left(\frac{\xi_0}{R_0}\right)^2 \int_0^{r_1} dr\, r^2 \int_0^1 dk^2 \frac{I_q^2}{I_c + sI_s} \int_0^\infty d\mathcal{E}\, \mathcal{E}^{3/2} \left.\frac{\partial f_h}{\partial r}\right|_{\alpha,\mathcal{E}}, \tag{4.21}$$

where

$$I_c \equiv I_q|_{q=1} = \frac{1}{\pi}\sqrt{\frac{2}{\varepsilon}}[2E(k^2) - K(k^2)] \ , \ I_s = \frac{4}{\pi}\sqrt{\frac{2}{\varepsilon}}[E(k^2) + (k^2-1)K(k^2)] \tag{4.22}$$

and $\partial/\partial r|_{\alpha,\mathcal{E}}$ is a partial derivative evaluated for constant α and $\mathcal{E}$ so that

$$\left.\frac{\partial f_h}{\partial r}\right|_{\alpha,\mathcal{E}} = \frac{\partial f_h}{\partial r} - \frac{1}{2r}(2k^2-1)\frac{\partial f_h}{\partial k^2},$$

and for an isotropic distribution function this is simply $\partial f_h/\partial r$.

Neglecting kinetic effects in the layer, the ideal dispersion relation in the limit $\omega \ll \omega_{*h}$ is

$$-i\,\frac{\sqrt{\omega(\omega-\omega_{*pi})}}{\omega_A} + \varepsilon_1^2 \frac{\sqrt{3}\pi}{s_1}\left[\delta\hat{W}_f + \delta\hat{W}_{kh}(0)\right] = 0. \tag{4.23}$$

Even in the limit $\omega = 0$, δW_{kh} still has both real and imaginary parts. The imaginary part of $\delta W_{kh}(0)$ arises as a consequence of the Landau resonance of barely precessing ions with the mode. Such ions have a pitch angle k^2 defined by $I_c(k^2) + sI_s(k^2) = 0$. It is clear from Eq. (4.23) that whilst the real part of δW identifies the pure growth rate γ, the imaginary part of $\delta W_{kh}(0)$ identifies a pure mode rotation ω_r. Indeed finite $\Im\{\delta W_{kh}(0)\}$, particularly at ideal marginal stability, can maintain $\omega > \omega_{*pi}$.

Whilst Coppi *et al* [32] recognised the importance of $\Re\{\delta W_{kh}(0)\}$, they ignored the Landau resonance of barely precessing ions with the mode, i.e. they took $\Im\{\delta W_{kh}(0)\} = 0$. In so doing, Coppi *et al* [32] stated that at marginal stability the ideal branches of both the sawtooth and the fishbone exist in gaps in the Alfvén continuum $0 < \omega_r < \omega_{*pi}$. Furthermore neglecting $\Im\{\delta W_{kh}(0)\}$ led Coppi *et al* [32] to believe that $\omega \ll \gamma_R$ when the internal kink mode is close to marginal stability. This falsely indicated that resistive effects must be included and hence the sign of $Re\{\delta W\}$ alone cannot provide a meaningful representation of stability.

4.2.2 ICRH Heating with $P_{\perp h} \sim \varepsilon P_c$

This section deals with a regime where $P_{\perp h}/P_c \sim \varepsilon$, and a general level of anisotropy such as $P_{\|h}/P_{\perp h} \sim 1$ or $P_{\|h}/P_{\perp h} \sim \varepsilon$. The fact that the hot ion equilibrium pressure

is much less than that of the core plasma means that the dependence of β_p on P_h is negligible. In such a regime Bussac's representation of the fluid stability is independent of the hot ions. One can clearly see this by recalling that the fourth order ideal kink stability is driven purely by toroidal effects. Upon examining Eq. (2.23), the dependence of the gradient of the Shafranov shift on hot ion pressure is negligible, i.e., if $P_{\perp h} \sim \varepsilon P_c$, hot ions do not contribute to toroidal effects. Nevertheless, hot minority ions do give rise to other fluid terms and these are quantified below.

In a regime where $P_{\perp h} \sim \varepsilon P_c$, the hot ions do not contribute significant kinetic or fluid effects in the singular layer. The following analysis is therefore only valid in the external region. From Eq. (3.38),

$$\delta f_h = \delta f_{fh} + \delta f_{kh},$$

where $\delta f_{fh} = -\boldsymbol{\xi}_\perp \cdot \boldsymbol{\nabla} f_h$ and δf_{kh} is the kinetic hot ion perturbation. Energy moments of δf_h gives the pressure tensor $\underline{\underline{P_h}} = \underline{\underline{P_{fh}}} + \underline{\underline{P_{kh}}}$. As before, the kinetic potential energy term δW_{kh} is obtained from $\underline{\underline{P_{kh}}}$. It follows from $P_{\perp h} \sim \varepsilon P_c$ that the perturbed hot ion pressure terms are uncoupled from the perturbed $\boldsymbol{j} \times \boldsymbol{B}$ terms. Therefore the hot fluid potential energy δW_{fh}, like δW_{kh}, is additive to the dispersion relation and is given by

$$\delta W_{fh} = \frac{1}{2} \int d^3x \, \boldsymbol{\xi}_\perp^* \cdot (\boldsymbol{\nabla} \cdot \underline{\underline{\delta P}}_{fh}),$$

where $\underline{\underline{\delta P}}_{fh} = -\boldsymbol{\xi}_\perp \cdot \boldsymbol{\nabla} \underline{\underline{P}}_h$. Using Eq. (2.30) and integrating by parts it can be shown that

$$\delta W_{fh} = -\frac{1}{2} \int d^3x \left(\boldsymbol{\xi} \cdot \boldsymbol{\nabla} (P_{\|h} + P_{\perp h}) - (P_{\|h} + P_{\perp h} + C) \frac{\boldsymbol{\xi} \cdot \boldsymbol{\nabla} B}{B} \right) \frac{\boldsymbol{\xi}^* \cdot \boldsymbol{\nabla} B}{B}, \quad (4.24)$$

where

$$C = 4\pi m_h \int_{-\infty}^{\infty} d\mathcal{E} \int_0^{\infty} d\mu \, \frac{B(\mu B)^2}{|v_\||} \frac{\partial f_h}{\partial \mathcal{E}}. \quad (4.25)$$

In most hot plasmas $P|\boldsymbol{\nabla} B|/(B|\boldsymbol{\nabla} P|) \lesssim \varepsilon$. Hence the hot fluid potential energy is approximately

$$\delta W_{fh} = -\frac{m_h}{2} \int d^3x \, \frac{\boldsymbol{\xi}^* \cdot \boldsymbol{\nabla} B}{B} \int dv^3 \, (v_\|^2 + \mu B) \boldsymbol{\xi} \cdot \boldsymbol{\nabla} f_h.$$

Now, substituting Eqs. (2.27) and (2.41) for $\boldsymbol{\xi}$ and following the analysis used for the kinetic contribution gives

$$\begin{aligned} \delta W_{fh} &= 2^{7/2} \pi^2 m_h R_0 \left(\frac{\xi_0}{R_0} \right)^2 \int_0^{r_1} dr \, r \int_0^{\infty} d\mathcal{E} \, \mathcal{E}^{3/2} \\ &\quad \times \int_0^{1/B_{\min}} d\alpha \, \left. \frac{\partial f_h}{\partial r} \right|_{\alpha \mathcal{E}} \oint d\theta \left(1 - \frac{\alpha B}{2} \right) \frac{B \cos\theta}{\sqrt{1 - \alpha B}}. \end{aligned}$$

It is of interest to separate the terms arising from trapped and passing ions. The total contribution of the trapped minority ions, which includes both kinetic and fluid

effects is

$$\delta W_{ht} = 2^{7/2}\pi^3 m_h R_0 \left(\frac{\xi_0}{R_0}\right)^2 \int_0^{r_1} dr\, r^2 \int_0^1 dk^2 \left(I_c - \frac{I_q^2}{I_c + sI_s}\right) \int_0^\infty d\mathcal{E}\, \mathcal{E}^{3/2} \left.\frac{\partial f_h}{\partial r}\right|_{\alpha,\mathcal{E}}, \tag{4.26}$$

where the subscript 't' denotes trapped, and Eq. (4.21) has been used for the kinetic contribution $\delta W_{kh}(0)$. Consider now the competing terms of Eq. (4.26). Taylor expanding I_q to first order in $1-q$ gives $I_q = I_c + (1-q)I_s$. Hence, in the limit where $s \ll 1$, the leading order kinetic and trapped fluid terms of Eq. (4.26) cancel with one another. In fact, it will be shown in Chapter 5 that $\Re\{\delta W_{ht}\}$ scales with $(1-q-s/2)\beta_h$, where β_h is defined similarly to that of Eq. (2.5).

If the hot ion energy distribution is highly anisotropic (e.g. $P_{\|h} \sim \varepsilon P_{\perp h}$) the fluid contribution δW_{hp} arising from the hot passing ions will be negligible. Otherwise, if $P_{\|h} \sim P_{\perp h}$, δW_{hp} can be evaluated in terms of pitch angle integration in $y = 1/k^2$. Such a calculation is detailed in Ref. [39].

The potential energy in a regime where $P_{\perp h} \sim \varepsilon P_c$ and $\omega \ll \langle \omega_{mdh} \rangle$ is therefore

$$\delta W = \delta W_c + \delta W_{ht} + \delta W_{hp}.$$

Since the hot ions do not contribute kinetic effects in the layer, the dispersion relation corresponds with that of Eq. (2.49), where $\delta \hat{W}_4^e$ is identified with δW above. In an ideal regime with $\omega > \omega_{*pi}$, instability of the internal kink mode is guaranteed for $\Re\{\delta W\} < 0$. Alternatively, if resistive effects are thought to be important, one can solve the dispersion relation with γ_I given by Eq. (2.55).

4.2.3 ICRH Heating with $P_{\perp h} \sim P_c$ and Moderate Anisotropy

In this section a regime is discussed where the hot ion pressure competes in magnitude with the core pressure and a small but finite anisotropy can exist. A highly anisotropic plasma in which, for example, $P_\|/P_\perp \sim \varepsilon$, introduces a strong θ dependence in $P_\perp$. It will be shown in Chapter 5 that $P_{\perp h}$ has the form

$$P_{\perp h}(r,\theta) = P_{\perp h}(r)\left[1 + \varepsilon \frac{P_{\perp h}(r)}{P_{\|h}(r)} F(r,\theta)\right]$$

where $F \sim 1$ and is strongly dependent on θ. In this section we consider the case where $\varepsilon P_\perp/P_\| \ll 1$ such that the dependence of pressure quantities on θ can be ignored. This limit was first considered in Ref. [42] where the additions to the MHD energy principle were obtained.

Consider now Eq. (4.24). The term that describes the leading order hot ion fluid stability is

$$-\frac{1}{2}\int d^3x\, \boldsymbol{\xi} \cdot \boldsymbol{\nabla}(P_{\|h} + P_{\perp h}) \frac{\boldsymbol{\xi}^* \cdot \boldsymbol{\nabla} B}{B}.$$

Since $P_{\perp h} \sim P_c$ this term must be incorporated with the core potential energy. Bussac's [15] toroidal potential energy term δW^T is therefore defined in terms of β_p with $P = P_c + (P_{\perp h} + P_{\|h})/2$. Also, if one wishes to include the effects of flux surface

shaping [43, 52], the corresponding potential energy term δW^S is additive to the total fluid potential energy.

The remainder of Eq. (4.24) is

$$\frac{1}{2}\int d^3x\,(P_{\|h}+P_{\perp h}+C)\frac{\boldsymbol{\xi}\cdot\boldsymbol{\nabla}B}{B}\frac{\boldsymbol{\xi}^*\cdot\boldsymbol{\nabla}B}{B}. \tag{4.27}$$

This term is not absorbed into the core potential energy term because, as discussed in the last section, it is an order of magnitude smaller than the leading order contribution. Integrating Eq. (4.27) by parts yields the total normalised fluid contribution

$$\delta\hat{W}_f = \delta\hat{W}^T + \delta\hat{W}^S + \frac{1}{6}\beta_C,$$

where β_C is defined in the same way as β_p except that the pressure is replaced with $(P_{\perp h}+P_{\|h}+C)/2$. In the isotropic limit, $P_{\perp h}+P_{\|h}+C=0$, and hence we recover the regime observed in Section 4.2.1.

The total perturbed potential energy of the external region in a regime where $P_{\perp h}\sim P_c$, and a small amount of anisotropy exists is:

$$\delta\hat{W} = \delta\hat{W}^T + \delta\hat{W}^S + \frac{1}{6}\beta_C + \delta\hat{W}_{kh}, \tag{4.28}$$

where one can use Eq. (4.21) for the definition of $\delta\hat{W}_{kh}$ in the limit $\omega \ll \langle\omega_{mdh}\rangle$. Equation (4.28) will be used in Chapter 5 to assess the stability of the internal kink mode for certain sawtoothing ICRH discharges. In these discharges the level of anisotropy is considered moderate and thus evaluation of Eq. (4.28) is provides an accurate measure of internal kink mode stability.

4.2.4 ICRH Heating with $P_{\perp h}\sim P_c$ and High Anisotropy

In some high power ICRH discharges at JET in which $P_{\perp h}\sim P_c$, the pressure anisotropy takes the form $P_{\|h}/P_{\perp h}\sim\varepsilon$. For such discharges neither of the representations of δW obtained in the previous two sections provide a reliable measure of internal kink stability. At present an exact analytical formulation for δW does not exist in regimes where $P_{\perp h}\sim P_c$ and $P_{\|h}/P_{\perp h}\sim\varepsilon$. Rather, in this section we use the knowledge gained from the previous sections to derive an expression containing the most important effects.

First consider the toroidal fluid stability. Bussac's calculation for δW^T is a quadratic function of the gradient of the Shafranov Shift:

$$\delta W^T = \delta W_A + \Delta'\delta W_B + (\Delta')^2\delta W_C.$$

This equation comes naturally from an analysis which takes account of the Shafranov shift of flux surfaces. Subsequently, δW^T can be written in terms of β_p after having employed Eq. (2.23) - an identity relating Δ' to β_p in an isotropic plasma.

Since the ICRH heating is high, the appropriate form for the kinetic potential energy δW_{hk} is defined in Eq. (4.21). It can easily be shown that in such a regime δW_{hk}

is large and positive. For conditions close to marginal stability, the toroidal potential energy must be equally destabilising. It is now proposed that in a highly anisotropic plasma the toroidal stability is again strongly influenced by Δ'. Furthermore, it is assumed that the leading order dependence of δW^T on Δ' in a plasma that is strongly unstable to toroidal effects is the same as that of an isotropic plasma:

$$\delta\hat{W}^T = \frac{(c^{(2)}+3)(b^{(2)}+3)}{12(c^{(2)}-b^{(2)})}\left(\frac{\Delta'}{\varepsilon_1}\right)^2, \tag{4.29}$$

where $b^{(2)}$ and $c^{(2)}$ involve only the q profile and are defined in Appendix A.

Equation (4.29) requires that the total Δ' contains the additional contributions arising from ions heated with high power ICRH. Fortunately Madden and Hastie [61] have calculated hydromagnetic equilibria for tokamaks in which the pressure is highly anisotropic. Expanding the perpendicular pressure as a Fourier cosine series in θ, Madden and Hastie obtained a second order differential equation for the generalised Shafranov shift Δ. Integrating Eq. (29) of Ref. [61] once with respect to r yields

$$\Delta' = \varepsilon_1\left[\beta_{pc} + \overline{\beta_{ph}} + A + \sigma + \frac{1}{4}\right] \tag{4.30}$$

where β_{pc} is the poloidal beta corresponding only to the core plasma and $\overline{\beta_{ph}}$ is the poloidal beta defined in terms of the hot perpendicular pressure averaged in θ, i.e.,

$$\overline{\beta_{ph}} = -\frac{2\mu_0}{B_0^2\varepsilon_1^2 r_1^2}\int_0^{r_1} r^2\frac{d(\overline{P_{\perp h}}+P_{\|h})/2}{dr}dr \text{ where } \overline{P_{\perp h}} = \frac{1}{2\pi}\int_{-\pi}^{\pi} P_{\perp h}\,d\theta. \tag{4.31}$$

Also, A is an anisotropic term proportional to the Fourier coefficient of $\cos 2\theta$:

$$A = \frac{\mu_0}{2B_0^2\varepsilon_1^2}P_{\perp h}^{(2)}(r_1) \text{ where } P_{\perp h}^{(2)}(r_1) = \frac{1}{\pi}\int_{-\pi}^{\pi} P_{\perp h}(r_1,\theta)\,\cos(2\theta)\,d\theta. \tag{4.32}$$

Not all of the hot ion fluid effects are contained in δW^T. Other important contributions arising from the trapped population are expected to compete with δW_{kh}. Contributions arising from hot passing ions are not expected to be significant on account of the level of anisotropy. Taking these points into account, the dominant effects are expected to be contained in the normalised potential energy

$$\delta\hat{W} = \delta\hat{W}^T + \delta\hat{W}_{ht} \tag{4.33}$$

with $\delta\hat{W}^T$ and $\delta\hat{W}_{ht}$ defined by Eqs. (4.29) and (4.26) respectively and Δ' by Eq. (4.30).

In Chapter 5, equation (4.33) is applied to JET sawtoothing discharges in which the anisotropy is high. At multiple times during each pulse, Δ' and $\delta\hat{W}_{ht}$ are calculated from measurements of the energetic ions and thermal plasma and compared with the sawtooth period. As before, the stability calculations are purely ideal and stability transitions are assumed to correspond with $\delta W = 0$.

4.3 Summary

A dispersion relation has been obtained for plasmas with thermal ions in the banana regime. The newly modified dispersion relation arrives as a result of a kinetic treatment which is employed consistently in the singular layer and the external region. This dispersion relation will be extended in Chapter 6 to include the effects of the equilibrium electric field and plasma rotation on the internal kink mode.

Also derived is an energy principle capable of describing the ideal internal kink mode stability of plasmas heated with ICRH. Various regimes have been discussed, some of which will be used in the following chapter for comparisons with sawtoothing discharges in JET.

Chapter 5

Modelling Sawtooth Destabilisation of ICRH Experiments in JET

The success of experiments using minority ion cyclotron resonant heating (ICRH) to control sawtooth activity in JET [8] and TFTR [9] has given rise to considerable interest in the nature of the stabilisation mechanism, and its relation to the distribution function of the heated ions. This chapter is dedicated to modelling the internal kink stability of recent ICRH heated deuterium - tritium (DT) sawtoothing discharges. In answer to some of the limiting factors outlined in Ref. [36] the contributions of the RF heated ions to the kink mode stability are evaluated using a realistic but analytically tractable distribution function [39]. In addition, suitable models are employed for the evolving safety factor which are based on novel experimental observations [62, 63].

A detailed investigation is presented in which consistent trends emerge from the rich variety of discharges analysed. The chapter is organised as follows. The minority ion distribution function f_h is introduced in Section 5.1 and is subsequently applied to the minority ion internal kink calculations of Chapter 4. The potential energy of the hot ions is defined in terms of f_h and various simplifications are carried out in Section 5.2. The parameters required to characterise δW are taken from JET ICRH sawtoothing data. The first of two studies is presented in Section 5.3 where it is found that the level of anisotropy is slight; the formalism developed in Section 4.2.3 is used to compare the data of sawtoothing discharges with internal kink stability. Section 5.4 is dedicated to a second study in which a more significant level of anisotropy is observed. Here the formalism presented in Section 4.2.4 is used in conjunction with the JET data. Finally, Section 5.5 contains a summary and a discussion on implications of the results.

5.1 Model of ICRH Minority Ion Distribution Function

In Section 3.2 it was assumed that the equilibrium distribution function depends only on $\mathcal{E}$, μ and r. In fact, the additional spatial dependence of f_h on θ is disallowed due to the vanishing of a term involving $\boldsymbol{B} \cdot \boldsymbol{\nabla} f_h$ in the drift kinetic equation [25]. It is therefore not legitimate to construct on each flux surface a bi-Maxwellian in $v_{\|}$ and $v_{\perp}$, because defining such a distribution in terms $\mathcal{E}$ and μ introduces a θ dependence through $v_{\perp}^2 = 2\mu B(r,\theta)$ and $v_{\|}^2 = 2(\mathcal{E} - \mu B(r,\theta))$. To remove the poloidal dependence of the bi-Maxwellian, it is assumed that f_h is governed by $v_{\perp}$ and $v_{\|}$ at the location on a flux surface where the greatest RF power exists [39].

In all the discharges analysed in this chapter the peak RF power is approximately located at $R = R_0$, i.e. $\theta = \pm\pi$. Evaluating the bi-Maxwellian distribution function at $\theta = \pi$ and writing it in terms of $\mathcal{E}$, μ and r obtains:

$$f_h(r,\mathcal{E},\mu) = 2n_h(r)G(r)\left(\frac{m_h}{2\pi T_{\perp h}(r)}\right)^{3/2} \exp\left[-m_h\left(\frac{\mu B_0}{T_{\perp h}(r)} + \frac{|\mathcal{E} - \mu B_0|}{T_{\|h}(r)}\right)\right]. \quad (5.1)$$

The normalisation factor $G(r)$ is evaluated using

$$n_h = \oint d\theta \int dv^3\, f_h,$$

which in conjunction with Eq. (3.53) gives [39]:

$$1/G(r) = \frac{1}{2\pi}\int_0^{1/B_{\min}} \frac{d\alpha}{(\alpha B_0 + (T_{\perp h}/T_{\|h})|1 - \alpha B_0|)^{3/2}} \oint \frac{d\theta\, B}{\sqrt{1 - \alpha B}}. \quad (5.2)$$

The integrals are simplified by splitting the pitch angle integration of $1/G$ into trapped and passing space. Using the pitch angle variable $y = 1/k^2$, where k^2 is defined in Eq. (3.13), one can show that [39]:

$$1/G(r) = \frac{2}{\pi}\sqrt{2\varepsilon}\int_0^1 dy\, K(y)\left[\frac{1}{\left(1 + \varepsilon\frac{T_{\perp h}}{T_{\|h}}|2y - 1|\right)^{3/2}} + \frac{1}{\left(y + \varepsilon\frac{T_{\perp h}}{T_{\|h}}(2 - y)\right)^{3/2}}\right],$$

where the elliptic integral of the first kind $K(y)$ arrives from the poloidal integration, whilst the first term in the square bracket corresponds to trapped ions and the other to passing ions.

It is important to show that Eq. (5.1) provides a realistic representation of a minority ion distribution heated with ICRH. To do this surfaces of constant f_h in $v_{\perp}$ and $v_{\|}$ are compared with surfaces previously obtained by solving a steady state Fokker-Planck equation that describes ICRH [64]. Since all particles, trapped and passing, pass through $\theta = 0$, it is convenient to evaluate surfaces of constant f_h in terms of $v_{\|}(\theta = 0)$ and $v_{\perp}(\theta = 0)$. Moreover, note that the trapping condition of Eq. (3.9) is also defined in terms of the perpendicular and parallel velocities evaluated at $\theta = 0$. Referring to Eq. (5.1) it is clear that the surfaces of constant f_h in terms of $v_{\|}(0)$ and $v_{\perp}(0)$ are given by

$$\frac{v_{\perp}^2(0)}{1 - \varepsilon} + \frac{T_{\perp h}}{T_{\|h}}\left|v_{\|}^2(0) - \frac{\varepsilon v_{\perp}^2(0)}{1 - \varepsilon}\right| = \mathcal{C}^2, \quad (5.3)$$

where $\mathcal{C}$ is a constant. Different loci are obtained depending on whether the argument of the modulus is positive or negative. If $v_{\|}(0)/v_{\perp}(0) \lesssim \varepsilon^{1/2}$, Eq. (5.3) describes a hyperbola whose centre lies at the origin. If $v_{\|}(0)/v_{\perp}(0) \gtrsim \varepsilon^{1/2}$, Eq. (5.3) describes either an ellipse or a hyperbola depending on whether $1 - \varepsilon T_{\perp h}/T_{\|h}$ is respectively positive or negative. The position that the two conics meet is approximately defined by $v_{\|}(0)/v_{\perp}(0) = \sqrt{\varepsilon}$. Particles with this pitch angle are trapped and their reflection points are $\pm\pi$. Referring to Fig. 5.1 (a) it is clear that these particles give rise to the most distinctive characteristics in f_h. It can be seen that the surfaces of Eq. (5.1) correspond to strong deviations from loci forming nested ellipses which are surfaces of constant f_h for a simple bi-Maxwellian. Shown in Fig 5.1 (b) is a solution of the Fokker-Planck equation taken from Ref. [64]. To depict clearly the similarity between the distribution function of Eq. (5.3) and that of Ref. [64], the surfaces of Fig. 5.1 (a) are evaluated at the unique flux surface corresponding to $\varepsilon = 0.14$, where it is assumed that the level of anisotropy is given by $T_{\|h}/T_{\perp h} = 0.17$ [41]. Also shown in Fig 5.1 (a) and (b) is the trapped - passing boundary, which, as defined in Eq. (3.9), corresponds to $v_{\|}(0)/v_{\perp}(0) = \sqrt{2\varepsilon}$. Both Figs 5.1 (a) and (b) exhibit sharply defined characteristics at $v_{\|}(0)/v_{\perp}(0) = \sqrt{\varepsilon}$, corresponding to particles with banana tips at the position of maximum heating. Hence, despite the simplicity of Eq. (5.1) we infer that it provides a realistic representation of the distribution of ions heated with ICRH.

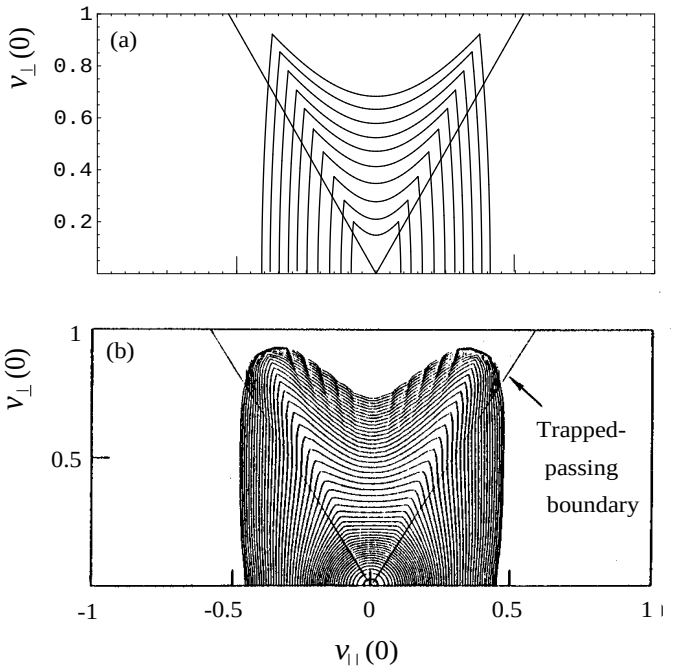

Figure 5.1: ICRH distribution function contours verses velocity coordinates $v_{\|}$ and $v_{\perp}$ evaluated at the outboard mid-plane ($\theta = 0$). (a): Contours of constant f_h, with f_h given by Eq. (5.1) for the unique parameter values $\varepsilon = 0.14$ and $T_{\|h}/T_{\perp h} = 0.17$. (b): Contours obtained from a steady-state Fokker Planck calculation in an ICRH heated plasma [64].

In the following sections the crucial parameters for characterising the hot ion population of recent JET discharges are either measured or modelled using the PION code [65], which calculates self-consistently the ICRH power deposition and the energetic ion distribution. One such parameter is the hot ion density $n_h(r)$, which is usually only measured at the edge. A degree of uncertainty surrounds the deposition of n_h with r, and for simplicity it will be assumed that the concentration

$$n_h/n_e$$

is constant throughout all the plasma.

The tail temperatures $T_{\perp h}$ and $T_{\|h}$ are also rather uncertain in many experiments. A measurement of the central hot ion temperature $T_{\perp h}(0)$ can, in some cases, be obtained using neutral particle analyser (NPA) experiments [66] and in others modelled using PION. However, the radial dependence of the perpendicular tail temperature is not known to a high degree of certainty. For this application the Stix formula is applied [40]:

$$T_{\perp h}(r) = \frac{\tau_s(r)\rho_{RF}(r)}{2n_h(r)}, \tag{5.4}$$

where τ_s is the classical Spitzer slowing down time and ρ_{RF} is the local RF power density coupled to the minority ions. The Spitzer slowing down time is proportional to $T_e^{3/2}/n_e$. Consequently, if ρ_{RF} is modelled in a plasma with maximum heating located close to the centre such that [39]

$$\rho_{RF} \propto \exp\left(-\frac{r^2}{D^2}\right),$$

with D a constant, then one obtains an approximate expression for the minority ion tail temperature deposition:

$$T_{\perp h}(r) = T_{\perp h}(0)\frac{\breve{T}_e^{3/2}(r)}{\breve{n}_e^2(r)}\exp\left(-\frac{r^2}{D^2}\right), \tag{5.5}$$

where $T_e(r) = T_{e0}\breve{T}_e(r)$ and $n_e(r) = n_{e0}\breve{n}_e(r)$.

In some of the discharges discussed later in this chapter the parallel tail temperature is also characterised using the PION code. However, an approximate guide to $T_{\|h}$ is discussed in Ref. [40]. Restricting attention to the central temperature, Stix suggested that:

$$T_{\|}(0) = 3.7T_{e0}(2A^{1/2}Z_{\text{eff}})^{2/3}, \tag{5.6}$$

where A is the minority ion mass number (e.g. $A = 2$ for deuterons) and Z_{eff} is the effective charge number in a plasma with more than one population of ions (typically $Z_{\text{eff}} \approx 4$ in JET). For simplicity and the lack of information to confidently guide otherwise, it is assumed that the level of anisotropy is constant with respect to r, i.e. $T_{\|h}(r) = [T_{\|h}(0)/T_{\perp h}(0)]T_{\perp h}(r)$.

McClements *et al* [41] used Eq. (5.6) to identify the parallel temperature and subsequently the anisotropy. In this thesis Eq. (5.6) will be used as a quantitative addition to PION thereby assisting in the reduction of uncertainty regarding the parallel dynamics of ICRH minority heating.

5.2 Modelling δW in ICRH Plasmas

In Section 5.1 a realistic but analytically tractable distribution function was defined. The kinetic and fluid potential energy terms described in Sections 4.2.3 and 4.2.4 can now be written in terms of f_h. The following sections describe analytical methods used to simplify the kinetic and fluid terms. Seeking analytical reductions wherever possible provides additional qualitative understanding and ultimately allows for the rapid numerical evaluation of internal kink stability.

5.2.1 Kinetic Contribution to δW

In Section 4.2.1 it was shown that δW_{kh}, and subsequently the ideal dispersion relation, is greatly simplified in limit $\omega \ll \langle\omega_{mdh}\rangle$. For analysing JET ICRH discharges in this chapter the $\omega \ll \langle\omega_{mdh}\rangle$ limit is always justified. Consider the triple integral of Eq. (4.21). The derivatives of f_h with respect to r and k^2 can be removed by integrating δW_{kh} by parts, and furthermore the energy integral is uncoupled from the radial and pitch angle integrals. From Eqs. (5.1) and (3.13) one can show that

$$f_h \propto \exp\left[\frac{-m_h\mathcal{E}}{T_{\perp h}}\left(1+\varepsilon\frac{T_{\perp h}}{T_{\|h}}|2k^2-1|\right)\right],$$

and thus the energy integral

$$\int_0^\infty f_h\mathcal{E}^{3/2}\,d\mathcal{E}$$

can be evaluated easily using the identity $\int_0^\infty \mathcal{E}^{3/2}\exp(-b\mathcal{E})\,d\mathcal{E} = 3\sqrt{\pi}/(4b^{5/2})$.

The pitch angle integration provides a means of separating the real and imaginary parts of δW_{kh}. The imaginary part arises as a consequence of the pole $I_c + sI_s = 0$, where I_c and I_s are defined in Eq. (4.22). In the limit $s \ll 1$, the pole occurs approximately at the unique pitch angle $k_c^2 = 0.83$ for which $I_c(k_c^2) = 0$. The imaginary component of the integral is evaluated by expanding the denominator of the integrand as: $I_c + sI_s = (k^2 - k_c^2)d/dk^2(I_c + sI_s)$. Subsequently, upon assuming $s \ll 1$ and $q - 1 \ll 1$, then

$$\Im\left\{\int_0^1 dk^2\, f_h\frac{I_q^2}{I_c+sI_s}\right\} \propto (1-q-s)^2 f_h(k_c^2),$$

where we have used $I_q = I_c + (1-q)I_s$, which at the pole becomes $I_q(k_c^2) = (1 - q - s)I_s(k_c^2)$. The remaining radial integration must be evaluated numerically. The details for this can be found in Ref. [39].

Upon considering the imaginary component of the ideal dispersion relation one can obtain an estimate of the mode rotation frequency $\omega_r = \Im\{\omega\}$ at marginal stability:

$$\frac{\sqrt{\omega_r(\omega_r - \omega_{*pi})}}{\omega_A} = \varepsilon_1^2\frac{\sqrt{3}\pi}{s_1}\Im\{\delta\hat{W}_{kh}\}, \tag{5.7}$$

where for most heating scenarios $\Im\{\delta\hat{W}_{kh}\}$ is large enough to allow a mode to exist with $\omega_r > \omega_{*pi}$. Indeed the figures depicted in Ref. [39] indicate that the real and imaginary components of δW_{kh} are a similar order of magnitude. Nevertheless, other authors [32] have assumed that $\Im\{\delta\hat{W}_{kh}\} = 0$ in the $\omega \ll \langle\omega_{mdh}\rangle$ limit. As mentioned earlier, including the imaginary part of δW in the dispersion relation can shift an ideal mode out of the gap in the Alfvén continuum, and also provide a stronger case for neglecting resistive effects. A thorough discussion on this topic is presented in Section 5.5.

The real part of δW_{kh} is obtained by evaluating the principal part of the pitch angle integral, which expanding in small $1-q$ and s has the form:

$$\int_0^1 dk^2\, f_h(k^2,r)\left[I_c(k^2,r) + 2\left(1 - q(r) - \frac{s(r)}{2}\right) I_s(k^2,r)\right]. \tag{5.8}$$

However, the pitch angle and radial integrals of $\Re\{\delta W_{kh}\}$ cannot be uncoupled from one another and hence the remaining double nested integrals have to be evaluated numerically.

In Sections 4.2.2 and 4.2.4 regimes were discussed in which the hot ions contribute significantly to particular fluid potential energy terms which are in addition to toroidal destabilising terms. One such fluid term corresponds to that of I_c contained in the pitch angle integral of Eq. (4.26) which describes the total trapped (hot fluid and kinetic) potential energy δW_{ht}. The trapped fluid contribution exactly cancels the kinetic term identified with I_c in Eq. (5.8) above. The remaining kinetic contributions of Eq. (4.26) give rise to the following scaling:

$$\Re\{\delta\hat{W}_{ht}\} \sim \left(1 - q - \frac{s}{2}\right)\frac{\beta_h}{\varepsilon_1^{1/2}},$$

where

$$\beta_h = -\frac{2\mu_0}{B_0^2\varepsilon_1^2 r_1^{3/2}}\int_0^{r_1} r^{3/2}\frac{dP_{\perp h}}{dr}dr.$$

The exact details concerning the numerical integration of $\Re\{\delta W_{kh}\}$ are described in Ref. [39]. However, it should now be clear that the kinetic contributions are evaluated with a high degree of accuracy, where particular attention has been paid to the pitch angle integrals.

5.2.2 Modelling Δ' and β_C

Section 4.2.4 proposed that the toroidal stability of an anisotropic plasma is strongly influenced by the key parameter Δ' - the gradient of the Shafranov shift. Evaluation of Δ' requires the hot ion pressure components $P_{\perp h}$ and $P_{\|h}$. These pressure components are obtained by taking moments of the equilibrium distribution function, and in a highly anisotropic plasma are strongly dependent on the poloidal angle. This section outlines the procedure for obtaining $P_{\perp h}$ and $P_{\|h}$, and through function modelling, a rapid numerical computation for Δ'. Furthermore, for moderately

anisotropic plasmas, the quantity β_C described in Section 4.2.3 is obtained in terms of simple computations for $P_{\|h}$, $P_{\perp h}$ and C.

The hot ion pressure components are most easily calculated by writing Eq. (5.1) as:

$$f_h = 2n_h G \left(\frac{m_h}{2\pi T_{\perp h}}\right)^{3/2} \exp\left[-m_h\left(\frac{v_\perp^2}{2\tilde{T}_{\perp h}} + \frac{v_\|^2}{2T_{\|h}}\right)\right].$$

The definition of $\tilde{T}_{\perp h}$ depends on the sign of $\mathcal{E} - \mu B_0$:

$$\frac{1}{\tilde{T}_{\perp h}} = \begin{cases} \frac{1}{T_{\perp h}}\left(\frac{B_0}{B} + \frac{T_{\perp h}}{T_{\|h}}\left(1 - \frac{B_0}{B}\right)\right) & \text{for } \mathcal{E} - \mu B_0 > 0 \\ \frac{1}{T_{\perp h}}\left(\frac{B_0}{B} - \frac{T_{\perp h}}{T_{\|h}}\left(1 - \frac{B_0}{B}\right)\right) & \text{for } \mathcal{E} - \mu B_0 < 0. \end{cases} \tag{5.9}$$

On the inboard side of the plasma (where $R < R_0$, or $\pi/2 < \theta < 3\pi/2$, such that $B > B_0$) it can be shown that $\mathcal{E} - \mu B_0 > 0$ for any combination of $v_\|^2$ and $v_\perp^2$. Subsequently, one can easily calculate the pressure components

$$\begin{aligned} P_{\|h} &= 4\pi m_h \int_0^\infty dv_\| \, v_\|^2 \int_0^\infty dv_\perp \, v_\perp f_h \\ P_{\perp h} &= 2\pi m_h \int_0^\infty dv_\| \int_0^\infty dv_\perp \, v_\perp^3 f_h, \end{aligned}$$

via the identity $\int_0^\infty x^{n+1} \exp(-ax^2)\, dx = \Gamma(n)/a^n$.

On the outboard side (where $R > R_0$, or $-\pi/2 < \theta < \pi/2$, such that $B < B_0$) the situation is more complicated. The difficulty lies at the threshold $\mathcal{E} - \mu B_0 = 0$, which upon substituting $B = B_0(1 - \varepsilon\cos\theta)$ corresponds to

$$v_\|^2 = v_\perp^2 \left(\frac{1}{1 - \varepsilon\cos\theta} - 1\right).$$

At $\theta = 0$, the threshold is approximately defined by $v_\|^2 = \varepsilon v_\perp^2$, and as shown in Fig. 5.1, surfaces of constant f_h are discontinuous at this pitch angle. Similar discontinuities exist throughout the entire outboard side. To tackle this the pressure components are evaluated using:

$$\int_0^\infty dv_\perp \int_0^\infty dv_\| = \int_0^\infty dv_\| \left[\int_0^{\frac{v_\|}{\sqrt{B_0/B - 1}}} dv_\perp + \int_{\frac{v_\|}{\sqrt{B_0/B-1}}}^\infty dv_\perp\right],$$

and subsequent analytical solutions to the perpendicular velocity integrals are obtained with the aid of: $2a\int x\, \exp(-ax^2)\, dx = -\exp(-ax^2)$ and $2a^2 \int x^3 \exp(-ax^2)\, dx = -(ax^2 + 1)\exp(-ax^2)$.

On the inboard side one obtains:

$$\begin{aligned} P_{\|h} &= 2n_h G T_{\|h} \left(\frac{T_{\|h}}{T_{\perp h}}\right)^{1/2} \frac{1}{1 - \lambda\cos\theta} \\ P_{\perp h} &= 2n_h G T_{\perp h} \left(\frac{T_{\|h}}{T_{\perp h}}\right)^{1/2} \left(\frac{1}{1 - \lambda\cos\theta}\right)^2, \end{aligned}$$

and on the outboard side:

$$\begin{aligned} P_{\|h} &= 2n_h G T_{\|h}\left(\frac{T_{\|h}}{T_{\perp h}}\right)^{1/2}\left[\frac{1-(\lambda\cos\theta)^{3/2}}{1-\lambda\cos\theta}+\frac{(\lambda\cos\theta)^{3/2}}{1+\lambda\cos\theta}\right] \\ P_{\perp h} &= n_h G T_{\perp h}\left(\frac{T_{\|h}}{T_{\perp h}}\right)^{1/2}\left[\frac{(3+\lambda\cos\theta)(\lambda\cos\theta)^{1/2}}{(1+\lambda\cos\theta)^2}\right. \\ &\qquad \left.+\frac{(1-(\lambda\cos\theta)^{1/2})^2((\lambda\cos\theta)^{1/2}+2)}{(1-\lambda\cos\theta)^2}\right], \end{aligned}$$

where

$$\lambda = \varepsilon\frac{T_{\perp h}}{T_{\|h}}.$$

If the level of anisotropy is so high that $T_{\|h}/T_{\perp h} \sim \varepsilon$, then by definition $\lambda \sim 1$, and hence it is clear that $P_{\|h}$ and $P_{\perp h}$ are strongly dependent on θ. The ordering $\lambda \sim 1$ reflects the level of anisotropy for some of the later ICRH discharges detailed in this chapter.

The appropriate limit for the formalism described in Section 4.2.3 is $\lambda = 0$. Together with $P_{\|h}$ and $P_{\perp h}$ one can also evaluate C, where C is defined by Eq. (4.25):

$$P_{\|h}(\lambda=0) = 2n_h G T_{\|h}\left(\frac{T_{\|h}}{T_{\perp h}}\right)^{1/2} \tag{5.10}$$

$$P_{\perp h}(\lambda=0) = 2n_h G T_{\perp h}\left(\frac{T_{\|h}}{T_{\perp h}}\right)^{1/2} \tag{5.11}$$

$$C(\lambda=0) = -4n_h G\frac{T_{\perp h}^2}{T_{\|h}}\left(\frac{T_{\|h}}{T_{\perp h}}\right)^{1/2}, \tag{5.12}$$

and hence in the isotropic limit ($T_{\perp h} = T_{\|h}$), one obtains $\beta_C = 0$ as expected. However, upon substituting Eqs. (5.10), (5.11) and (5.12) for the case where $T_{\perp h} \gtrsim T_{\|h}$, one finds that $\beta_C \neq 0$. The toroidal effects associated with β_C together with kinetic effects and core toroidal effects all contribute to Eq. (4.28), which in Section 5.3, is used to compare the ideal internal kink stability threshold with moderately anisotropic sawtoothing discharges.

To evaluate Δ' one can see from Eq. (4.30) that the quantities $\overline{P_{\perp h}}$ and $P_{\perp h}^{(2)}(r_1)$ must first be considered. We seek to facilitate the evaluation of Δ' by ensuring that numerical calculations are limited to radial integration only. To assist in this the pitch angle integrals of Eq. (5.2) are fitted to a polynomial in λ. By evaluating the pitch angle integrals numerically within the range $0 \leq \lambda \lesssim 3$, and comparing with the polynomial fit, G can be determined with an error of less than 1 percent:

$$G = \left(\frac{T_{\perp h}}{T_{\|h}}\right)^{1/2} G_N,$$

where, for $0 \leq \lambda \lesssim 3$,

$$G_N = 0.49528 + 0.1097\lambda - 0.00598\lambda^2.$$

Note that in addition to Δ', this definition of G can be substituted into β_C.

The poloidal integrals of $\overline{P_{\perp h}}$ and $P^{(2)}_{\perp h}(r_1)$ are also fitted to a polynomial in λ. For maximum error bars of less than one percent:

$$\begin{aligned} \overline{P_{\perp h}} &= 2G_N n_h T_{\perp h} \overline{F} \\ P^{(2)}_{\perp h} &= 2G_N n_h T_{\perp h} F^{(2)}, \end{aligned}$$

with

$$\begin{aligned} \overline{F} &= 1.01361 - 0.45243\lambda + 0.16633\lambda^2 - 0.03439\lambda^3 + 0.00291\lambda^4 \\ F^{(2)} &= 0.007 - 0.33466\lambda + 0.20686\lambda^2 - 0.05951\lambda^3 + 0.00661\lambda^4, \end{aligned}$$

which is again valid for $0 \leq \lambda \lesssim 3$. According to Ref. [61], the poloidal dependence of $P_{\|h}$ is negligible. Hence the definition

$$P_{\|h} = 2n_h G_N \left(\frac{T_{\|h}(0)}{T_{\perp h}(0)} \right) T_{\perp h}$$

is used in $\overline{\beta_{ph}}$. Finally, $\overline{\beta_{ph}}$, A and σ of Eqs. (4.31), (4.32) and (2.24) are easily evaluated via numerical integration in the minor radius. Defining the normalised quantities $\hat{n}_h = n_h \times 10^{-19}$ and $\hat{T}_{\perp h} = T_{\perp h}/1$ keV, it is straightforward to show that:

$$\begin{aligned} \overline{\beta_{ph}} &= -\frac{4.026 \times 10^{-3}}{B_0^2 \varepsilon_1^2 r_1^2} \int_0^{r_1} dr\, r^2 \frac{d}{dr} \left[\hat{n}_h \hat{T}_{\perp h} G_N \left(\overline{F} + \frac{T_{\|h}(0)}{T_{\perp h}(0)} \right) \right] \\ A &= \frac{2.013 \times 10^{-3}}{B_0^2 \varepsilon_1^2} \hat{n}_h \hat{T}_{\perp h} G_N F^{(2)} \Big|_{r_1}, \end{aligned}$$

where the radial dependence enters G_N, $\overline{F}$ and $F^{(2)}$ through λ.

Using Eq. (4.30), the gradient of the Shafranov shift can now be calculated easily for regimes where the plasma is highly anisotropic. This computation of Δ' is used in Section 5.4 to characterise the toroidal stability of JET sawtoothing discharges.

5.3 The Sawtooth Trigger in JET ICRH Discharges and the Evolution of q

Already in this chapter potential energy terms suitable for describing the ideal internal kink mode stability of ICRH discharges have been defined. This analysis is now used to correlate marginal stability with the sawtooth crash events of JET DTE1 ICRH experiments.

Rather than attempting to obtain evidence of a pressure driven trigger, this section investigates the possible link between the sawtooth trigger and the evolving q profile. This differs from previous attempts [67, 68, 69] to correlate characteristics of the q profile with the trigger because in the current study the ideal limit is assumed. To

undertake such an investigation we choose to analyse two particular shots chosen from a class of DTE1 ICRH discharges [70]. Both constitute tritium rich plasmas with relatively high concentrations of minority ions: one with minority deuterium (D) and the other Helium (He^3). In both discharges the ICRH power is relatively low, which when coupled with the high concentrations of either D or He^3 minority ions, gives rise to relatively small tail temperatures which are only moderately anisotropic. Conversely, as discussed in Section 5.4, low concentrations of minority protons heated with high power RF give rise to very high perpendicular tail temperatures and a high degree of anisotropy. However, the appropriate regime in the present study is described in Section 4.2.3 and in particular the relevant hot ion pressure quantities are defined by Eqs. (5.10) - (5.12).

5.3.1 Ramping Phase Model

To correlate the ideal kink mode stability with the sawtooth trigger we choose to only consider the effects of the safety factor. During the quiescent period of the sawtooth cycle it is well known that both the pressure and the q profile evolve. For simplicity and clarity, core and minority pressure contributions are held constant whilst the effect of the evolving q profile is analysed. One might argue that this is a particularly good approximation in the case of giant sawteeth where the ramping up of the pressure is greatly reduced in the later stages of the quiescent period. Conversely however, a pressure driven sawtooth trigger is given consideration in Section 5.4.

Experiments in a number of tokamaks including JET [12] have demonstrated that q_0 remains below unity during the whole sawtooth cycle. On TFTR the motional stark effect MSE [71] has shown with particular clarity the ramping down of q_0 during the quiescent period of the sawtooth [62]. Figure 5.2, taken from Ref. [62] demonstrates that q_0 changes by between 10 and 20 percent during the sawtooth cycle, and in addition suggests that an approximate model of the ramping down might be linear in time.

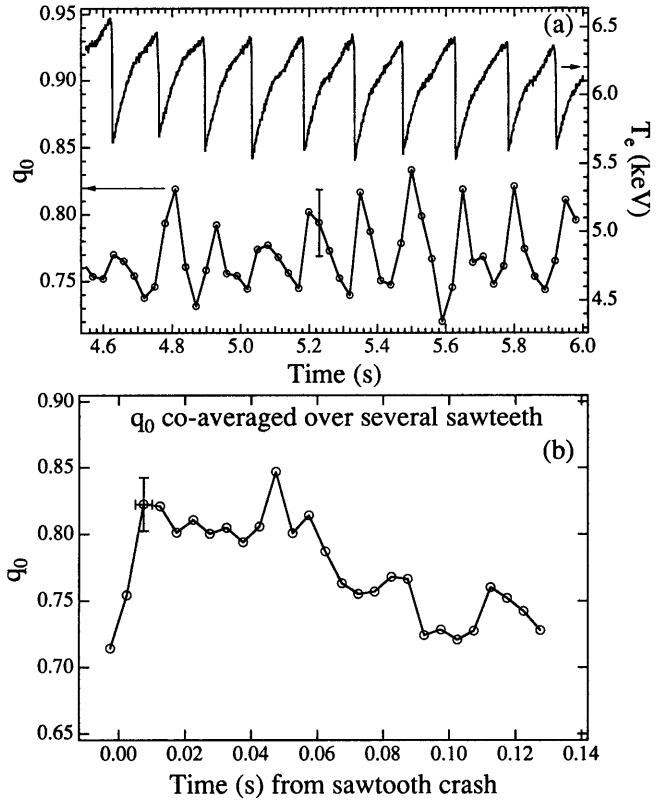

Figure 5.2: (a) q_0 measurements using MSE during sawtoothing on the TFTR tokamak. (b) q_0 evolution during the Sawtooth ramp, obtained by averaging over 9 consecutive Sawtooth events [62].

In addition to q_0, characterisation of the evolving q profile can be supplemented by information regarding the $q = 1$ radius. Pellet injection in JET quite frequently results in the creation of a high density closed tube of plasma (the Snake) [63] on the $q = 1$ surface when a pellet of sufficient size reaches the core. Snakes are long lived phenomena aligned to the closed magnetic field lines of the $q = 1$ surface. They often survive many sawtooth crashes, with the thermal and density redistribution taking place around them. Figure 5.3 shows the evolution of X-ray flux and inferred values of r_1 during a sawtooth cycle. At each sawtooth event, the radial position of the Snake suddenly decreases by up to 40 percent [63], and then increases slowly during the subsequent ramp phase of the sawtooth.

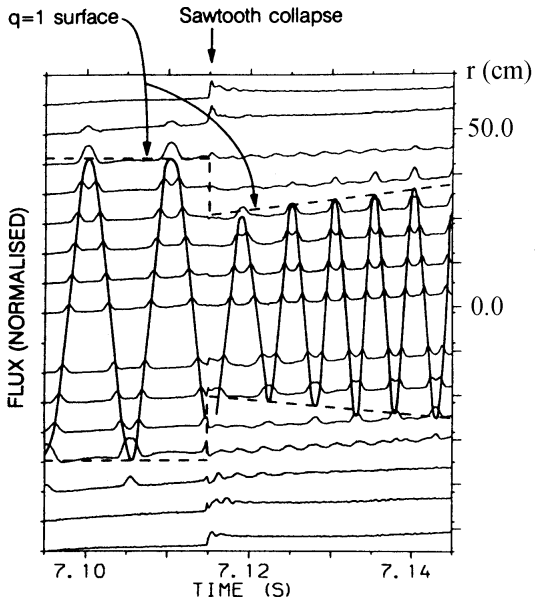

Figure 5.3: X-ray-flux plot for the vertical-camera signals showing the inward shift of the snake during a sawtooth collapse in JET. The solid line follows the point of maximum emission and the dashed line the inferred radius of the $q = 1$ surface [63].

In the forthcoming analysis the following q profile is assumed:

$$q = q_0(1 + c(r/a)^{2d})^{1/d}, \tag{5.13}$$

with a the plasma boundary. This description for q admits a very flat profile inside r_1 and a steep increase to the boundary value q_a. The q profile can be characterised in terms of a, q_0, q_a and r_1 via a solution of

$$1 - q_0 + \left(q_0 - q_a^d\right)\left(\frac{r_1}{a}\right)^{2d} = 0$$

for d which then gives $c = q_a^d/q_0 - 1$.

JET does not currently have an accurate diagnostic for measuring the safety factor in the core. Consequently, the evolution of q_0 and r_1 during the sawtooth cycle of the discharges described in this thesis are not known to a high degree of certainty. To counter this, in the following section δW is calculated for a whole range of possible combinations of r_1 and q_0 using the above model for q.

5.3.2 Results

The two sawtoothing discharges depicted in Fig. 5.4 are considered in this investigation. Each vertical line in Fig. 5.4 represents a time at which parameters characterising

the core plasma and energetic ion population were either measured or modelled using the PION code [65].

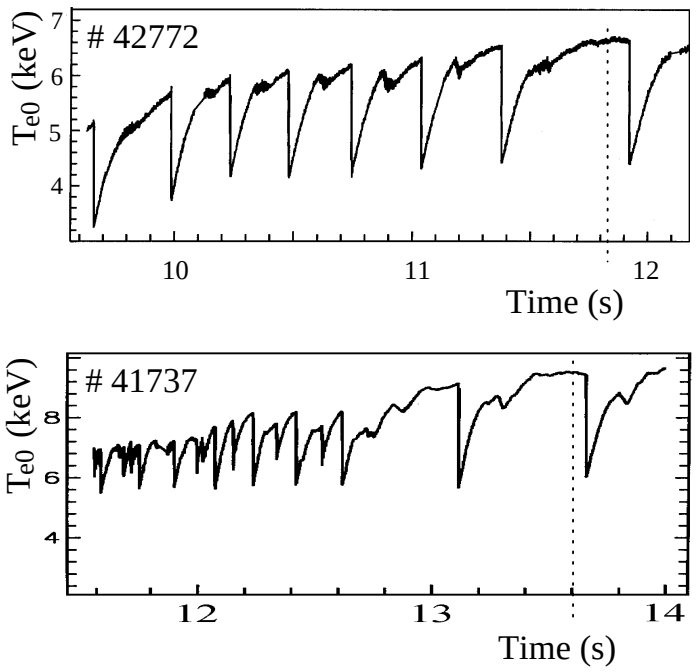

Figure 5.4: Showing the evolving central electron temperature of discharges 42772 and 41737 from the JET DTE1 campaign. The vertical dotted lines represent times at which parameters characterising the core plasma and energetic ion population were either measured or modelled.

Discharge 42772 comprises a tritium rich plasma with 9 percent minority heated deuterium [(D)T]. The RF power was approximately 4 MW and the central hot ion perpendicular tail temperature approximately $T_{\perp h}(0)$ =110 keV with anisotropy $T_{\|h}/T_{\perp h} \gtrsim 1/2$. Discharge 41737 comprises an equal mixture of deuterium and tritium with 6 percent minority heated helium [(He^3)DT]. The RF power was 4.5 MW and the perpendicular tail temperature approximately $T_{\perp h} = 220$ keV with $T_{\|h}/T_{\perp h} \gtrsim 1/2$.

The measured and modelled parameters for the bulk and minority plasma are used in code which evaluates the separate components and collective response of Eq. (4.28). For convenience however, the hot ion term involving β_C is absorbed into the more dominant toroidal term $\delta\hat{W}^T$. The normalised potential energy components depicted in Figs. 5.5 and 5.6 are evaluated for the parameters inferred from discharges 42772 and 41737 respectively and plotted against r_1 and q_0. Note that Figs. 5.5 and 5.6 only depict the real components of $\delta\hat{W}_{kh}$ and $\delta\hat{W}$, and for convenience the notation '$\Re\{\}$' is henceforth neglected.

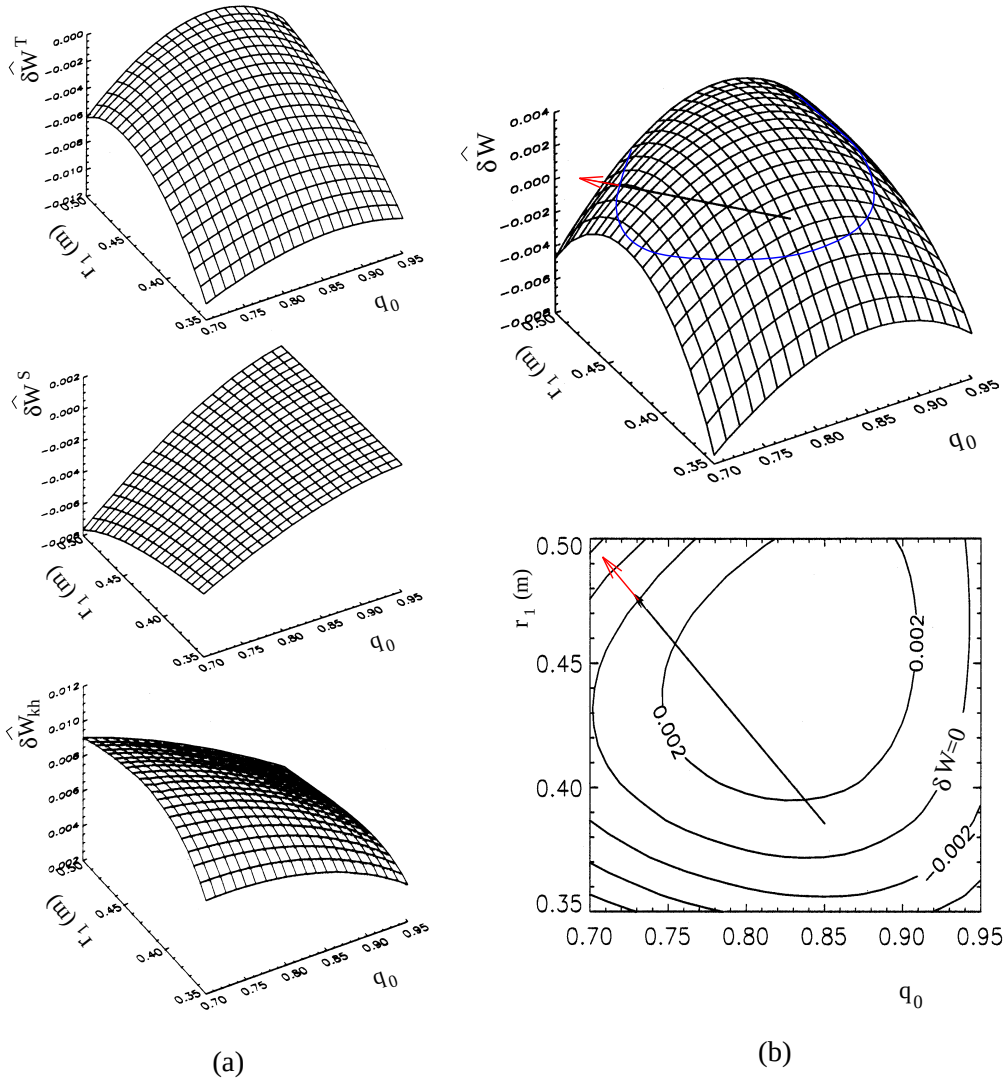

Figure 5.5: Computations of the toroidal $\delta\hat{W}^T$, shaping $\delta\hat{W}^S$, hot kinetic $\delta\hat{W}_{kh}$ and total potential energy $\delta\hat{W}$ against r_1 and q_0 for parameters inferred from discharge 42772. (a) Showing separately $\delta\hat{W}^T$, $\delta\hat{W}^S$, $\delta\hat{W}_{kh}$. (b) Illustrating the real component of the total potential energy in both a surface plot and a contour plot. Marginal stability ($\delta W = 0$) is clearly marked on the surface plot by the blue contour. The arrow represents a possible trajectory of r_1 and q_0 during the sawtooth-free period. Destabilisation of the kink mode is indicated by a change in the colour of the arrow from black to red. Note that the maximum $q = 1$ radius considered is $r_1 = 0.5m$, which is not far exceeding the maximum radius of Fig. 5.3. In JET $r_1 = 0.5$ corresponds to the normalised radius $r_1/a \approx 0.4$.

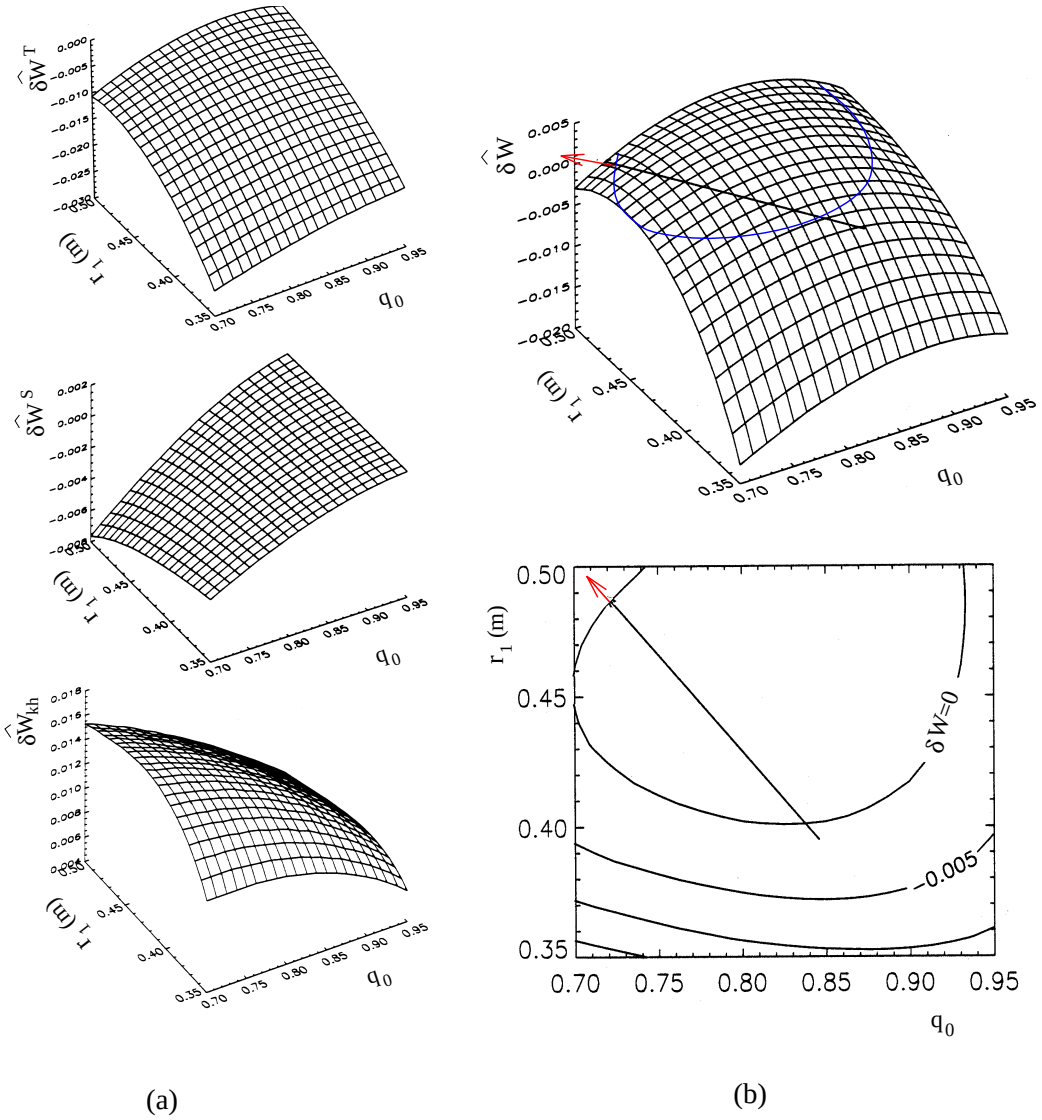

Figure 5.6: Computations of $\delta\hat{W}^T$, $\delta\hat{W}^S$, $\delta\hat{W}_{kh}$ and $\delta\hat{W}$ against r_1 and q_0 for parameters inferred from discharge 41737. See Fig. 5.5 for additional information.

To assist in qualitative understanding, a trajectory in r_1-q_0 space is depicted. As discussed in Section 5.3.1, it is expected that during the quiescent period, r_1 and q_0 will evolve in a course similar to that shown in Figs. 5.5 and 5.6. Assuming this to be the case, the following observations are found to be consistent in discharges 42772 and 41737. A modest rise in $\delta\hat{W}_{kh}$ is accompanied by much larger increases in $|\delta\hat{W}^T|$ and $|\delta\hat{W}^S|$, the result being that $\delta\hat{W}$ changes sign from positive to negative. Thus, the analysis is consistent with a scenario in which the ideal internal kink mode

becomes unstable at a time corresponding roughly to the end of the sawtooth-free period. A similar observation was also made by McClements *et al* [41] in a brief account concerning the effects of the q profile on δW. McClements explained that, in addition to $\delta\hat{W}^T$, one might expect that the shaping term $\delta\hat{W}^S$ of Eq. (A.3) should increase with r_1 since flux surface cross sections become progressively less circular toward the plasma boundary (see Fig. 2.6).

This investigation illustrates the effects of the evolving q profile on the ideal internal kink mode stability. The regime suitable for evaluating the marginal ideal kink mode stability of JET ICRH discharges 42772 and 41737 requires flux surface shaping effects and inclusion of the effects of hot ions on toroidal effects. The kinetic terms are shown to contribute considerable stabilisation. However, by including the evolution of q and neglecting the pressure evolution, the ideal fluid terms are found to dominate changes in the internal kink mode stability during the sawtooth quiescent period. It is shown that the effects of the evolving safety factor on the ideal stability could be an important contribution to the sawtooth trigger mechanism. These results appear to be consistent with the observation that an increased inversion radius introduces stronger sawtooth activity [36, 37].

5.4 Sawtooth Evolution during JET ICRH Pulses

The last section presented ideal stability calculations based on the evolving q profile during the quiescent phase of a unique sawtooth cycle. In contrast, this section presents a more detailed study in which at multiple times during each pulse, the evolution of the kinetic and fluid potential energy terms are calculated and compared with the evolving sawtooth duration [72, 73]. This goes beyond previous tests [8, 37, 41] which concentrated on measurements of the threshold ICRH power for sawtooth suppression.

The recent DTE1 campaign has yielded ICRH pulses during which both the sawtooth characteristics and the ICRH minority ion population both evolve substantially. Figure 5.7 shows five such discharges. In each, the RF power was ramped up slowly, thereby increasing the minority ion tail temperatures and correspondingly the sawtooth free periods of consecutive sawtooth cycles. Each discharge was heated with relatively low concentrations ($n_h/n_e \approx 0.03$) of minority protons, which, as mentioned in Section 5.3, for the level of applied RF power, the perpendicular tail temperatures were very high (up to 1.1 MeV) and the degree of anisotropy also large. Consequently, the appropriate regime for modelling the kink mode stability of the discharges depicted in Fig. 5.7 is described in Section 4.2.4.

Each vertical line in Fig. 5.7 denotes a time at which the parameters characterising the plasma were either measured experimentally or modelled using the PION code. The parameter values are then used to calculate the hot ion contribution $\Re\{\delta\hat{W}_h\}$ of Eq. (4.26) and in parallel, a measure of the destabilising toroidal MHD energy of the plasma is provided by evaluating Eq. (4.30) for Δ'. To assist in these calculations, the analysis outlined in Section 5.2 is employed.

It was pointed out in Section 5.3 that the q profile is not usually known to a high degree of accuracy in JET. However, each of the dotted lines of Fig. 5.7 correspond approximately to the end of the quiescent period, and it is at this point in time when r_1 can be inferred easily from measurements of the inversion radius. Upon employing Eq. (5.13), it is clear that the remaining parameter required to characterise q is q_0. To deduce q_0, a model inspired by the data shown in Fig. 5.2 is assumed. The model is consistent with the general observation that q_0 decreases with lengthening sawtooth quiescent period, i.e. q_0 at times corresponding to the earlier dotted lines of Fig. 5.7 assume larger values than those of later times. Specifically, the model sets $q_0 = 0.8$ at the start of the sawtooth cycle and at the end of the largest sawtooth free period $q_0 = 0.7$. Intermediate values of q_0 throughout the discharge are calculated via a simple linear interpolation.

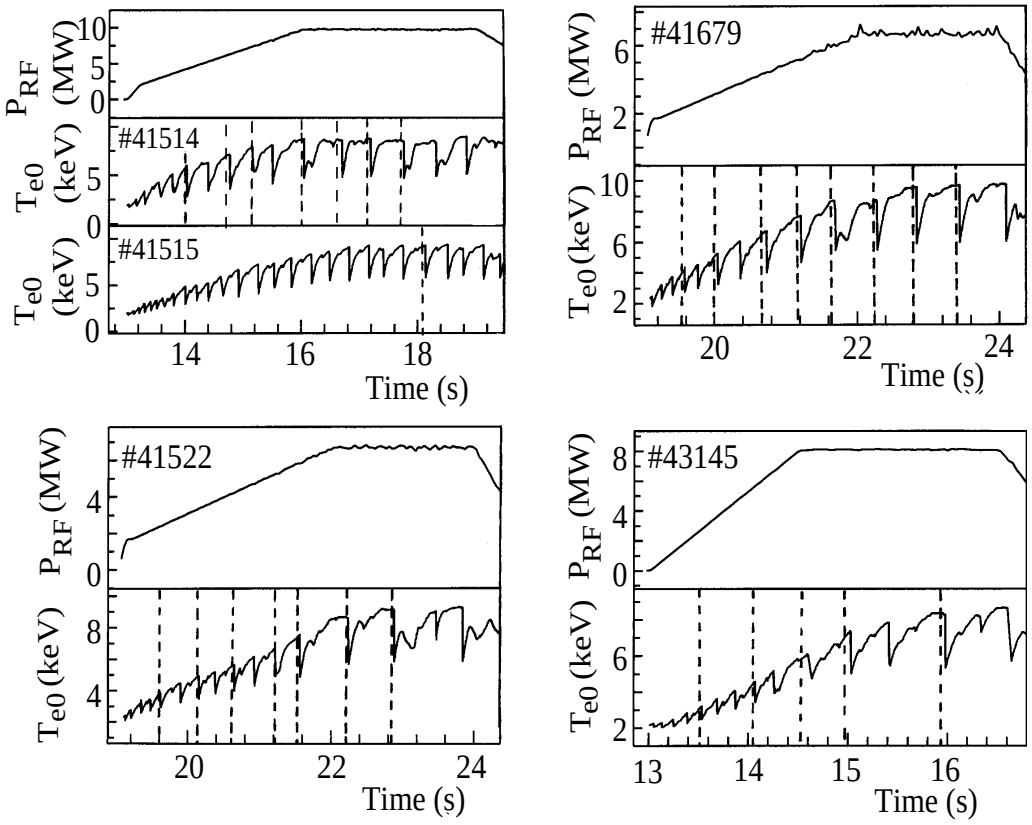

Figure 5.7: Time profiles of ICRH power and central electron temperature. Discharges 43145, 41514, 41515 and 41522 are (H)D plasmas. Discharge 41679 is a (H)DT plasma. Vertical dotted lines correspond to times when internal kink calculations were computed (see Fig. 5.8).

Both the real component of $\delta\hat{W}_h$ and Δ' are calculated and plotted in Fig. 5.8

as a function of the sawtooth period τ_s, at times corresponding to the vertical dotted lines of Fig. 5.7 (note that unless otherwise stated, it will be assumed henceforth that $\delta\hat{W}_h$ represents the real part of the complex quantity). Figure 5.8 demonstrates that in five separate JET pulses the stabilising effects associated with energetic particles and the destabilising effects of higher pressure both increase with lengthening sawtooth period. Theory suggests [30, 31, 32] that, as the plasma pressure rises and Δ' increases during a pulse, continued stabilisation is possible if $\delta\hat{W}_h$ increases sufficiently. Thus, the systematic correlation between $\delta\hat{W}_h$, Δ' and τ_s throughout Figure 5.8 is consistent with the premise that a sawtooth crash occurs when the ideal kink mode is close to marginal stability. This is clear in pulses 41522, 41679 and 43145 and additional support is provided by pulses 41514 and 41515. The latter two are similar, except that the RF wave orientation was reversed. As a result the central perpendicular tail temperature of ions in 41514 peaked at 850 keV, but only at 350 keV in 41515 [74]. The sawteeth in 41514 are of a much longer duration than those of 41515, thus providing additional evidence for sawtooth stabilisation by populations of energetic ions. Contrasting levels of stabilisation from the energetic ions, quantified by calculating $\delta\hat{W}_h$ during pulses 41514 and 41515, are shown in Fig. 5.8: data for energetic ions in 41515 were only available at a single time.

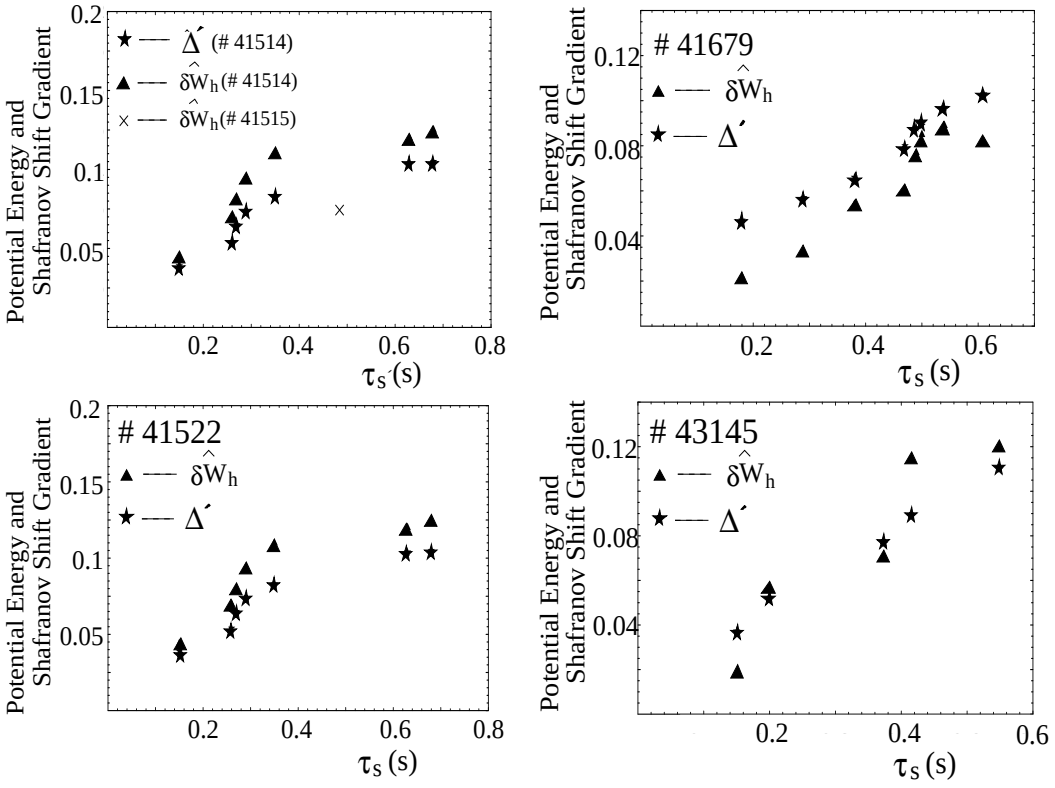

Figure 5.8: Computed values of Δ' and $\delta\hat{W}_h$ and measured values of sawtooth duration τ_s at multiple times during the discharges shown in Fig. 5.7.

In summary, the JET DTE1 campaign included sawtoothing ICRH pulses in which both the sawtooth characteristics and the energetic minority ion population evolved substantially. For multiple times during several sawtoothing pulses, the evolution of the kinetic and fluid potential energies have been calculated from measurements and PION simulations of the energetic ions, and compared with the evolving sawtooth duration. It is shown that minority ion stabilisation of the $m = 1$ internal kink mode increases in parallel with destabilising toroidal effects, as expected from experimental observations of increasing sawtooth duration. This is consistent with previous demonstrations that q_0 usually remains below unity for the whole sawtooth period in JET [12]. Despite this, long ramping times and giant sawteeth are observed, the latter coinciding with strong kinetic stabilisation.

5.5 Summary and Discussion

A generalised energy principle has been used to examine the stability of the ideal internal kink mode for plasmas with ICRH heating. A key feature of the analysis is the implementation of a new analytically tractable distribution function [39]. It is shown that the model distribution function describes salient features of the pitch angle dependence of ion populations heated with ICRH. In particular, the tail temperatures are inferred from Stix's [40] model and the distribution function is independent of the poloidal angle, thereby satisfying the drift kinetic equation. Also in this chapter, and in addition to the simple expressions obtained in Ref. [39] for $\delta\hat{W}_{ht}$, the effects of the hot ions are extended to allow accurate computation for Δ'.

In a study that compares theory with recent DTE1 experimental data it is shown that the ideal sawtooth trigger is sensitive to the q profile. The observed sawtooth cycle and corresponding evolving safety factor is found to be consistent with computations of the ideal internal kink mode stability. This broadens the debate regarding the possible mechanism behind what drives the sawtooth crash event.

In a further investigation, another ideal internal kink mode model is used to analyse DTE1 discharges that include highly energetic ICRH minority protons. It is consistently shown that the destabilising toroidal effects of these discharges increases with sawtooth period. However, as reflected by the extended quiescent times of giant sawteeth, the kinetic stability of the hot ions also increase. The consistency of the stability calculations with sawtooth behaviour during each pulse enhances confidence in applying the generalised collisionless energy principle [25, 28] to the modelling and prediction of sawtooth phenomenology in present and future tokamak fusion experiments involving energetic particles.

The effects of resistivity on the internal kink mode have not yet been considered. As discussed in Section 2.4.7 these are controlled by the parameter $\Lambda \equiv -i\left[\omega(\omega-\hat{\omega}_{*e})(\omega-\omega_{*i})\right]^{1/3}/\gamma_R$, where $\hat{\omega}_{*e} = \omega_{*e}(1+0.71\eta_e)$, $\omega_{*e} = dP_e/dr/(en_eB_0r)$, $\omega_{*i} = -dP_i/dr/(en_iB_0r)$, $\eta_e = d\ln T_e/d\ln n_e$ and γ_R is the growth rate of the resistive

$m = 1$ mode. This last quantity varies as $s_1^{2/3}$, where s_1 is magnetic shear at the $q = 1$ surface. The ideal limit is represented by $|\Lambda| \to \infty$. Solving the full dispersion relation [30, 31, 32] could, in principle, enable further comparisons with observation to be made. In practice, uncertainties in the q-profile preclude meaningful comparisons: in particular, the transition between ideal and resistive behaviour is controlled by the value of Λ, which itself is strongly dependent on s_1, a parameter which could not be measured directly in the JET pulses considered here. It should also be mentioned that the imaginary component of the ideal dispersion relation at marginal stability, defined by Eq. (5.7), typically defines a mode with $\omega_r > \omega_{*pi}$. Hence, unlike Coppi *et al* [32] and many other authors subsequently who, neglecting the contribution $\Im\{\delta\hat{W}_{kh}\}$ in the ideal and marginally stable dispersion relation, obtain $\Lambda = 0$, it is found that for suitable estimates of s_1, the solution of Eq. (5.7) gives $\Lambda \sim 1$. Although this certainly does not mean that resistive effects are negligible, it does demonstrate that by consistently accounting for the Landau resonance of barely trapped energetic ions with the mode, a stronger case for neglecting resistive effects can be made.

We now turn to the question of toroidal plasma rotation, which in this chapter has been assumed to be negligible. The effects of toroidal plasma rotation on the internal kink mode for plasmas in the banana regime are considered in the next chapter, particularly in the regime where the toroidal plasma rotation frequency $\Omega \sim \omega_{*pi}$. Similar modifications in plasmas where the collisionless population are hot minority ions requires $\Omega \sim \langle\omega_{mdh}\rangle$. Such an ordering is easily possible in NBI discharges where typically in JET $\Omega \sim 10^5$ rad/s. However, for ICRH heating, the maximum value of Ω corresponds to about 10 - 20 percent of the plasma rotation observed with NBI heating in similar experimental conditions [75]. In addition, the precessional drift velocities of ICRH ions are generally much larger than those of NBI ions. These observations justify neglecting the effects of plasma rotation in all the discharges considered in this chapter.

Chapter 6

Toroidal Plasma Rotation and the Stability of the Internal Kink Mode in the Banana Regime

With the long term interest of nuclear fusion research turning towards ever larger tokamaks and hotter plasmas, the kinetic effects of thermal ions has become an issue of increasing importance. Perhaps most crucial is the question of extended sawtooth quiescent periods in 'next step' devices, and the possible relationship to strong kinetic stabilisation. Another particularly relevant issue is the effect that the equilibrium electric field and toroidal plasma rotation may have on sawteeth. This is a neglected area of research. Nevertheless, as mentioned in Section 5.5, in many experiments the plasma rotation frequency is observed to be very large. The present chapter attempts to tackle these important points.

The effect of toroidal plasma rotation on the internal kink mode is, for the first time, evaluated in the banana regime. The plasma rotation caused by the equilibrium electric field Ω_Φ is limited to an ordering where $\Omega_\Phi \sim \omega_{*pi}$. This is well within the regimes observed in experiments and furthermore $\Omega_\Phi \sim \omega_{*pi}$ ensures that the stability of the internal kink mode is very sensitive to small variations in the toroidal plasma rotation. In addition, and unlike many other studies, e.g. [44], the ideal collisionless internal kink mode dispersion relation is solved exactly. To achieve this, $\delta\hat{W}_{ki}$ is first reduced analytically and then the tractable numerical integrals are evaluated exactly, rather than expanding $\delta\hat{W}_{ki}$ about one of the many commonly used limits.

The impact of toroidal plasma rotation is analysed chiefly via evaluation of the critical poloidal beta. This classical measure of the internal kink stability [15] is chosen for two principal reasons. First, it provides useful information regarding the ideal stability threshold. Indeed, the MHD critical value $\beta_p^c \approx 0.3$ provides an obvious benchmark relative to modifications that correspond to the kinetic effects of the

thermal ions. Second, evaluating β_p^c only requires solving the dispersion relation at marginal stability: the kinetic terms are greatly simplified for cases where the growth rate is zero. However, in some cases, the sign and magnitude of growth rates are computed close to threshold conditions.

This chapter is organised as follows. The leading order plasma flows are described in Section 6.1. Following this, Section 6.2 contains a discussion relating the relative sizes of various competing natural frequencies and an analysis that extends the dispersion relation of Eq. (4.19) to include the equilibrium electric field and induced plasma rotation. In Section 6.3 the typical characteristics (including the plasma rotation magnitude and profile) of sawtoothing discharges are described and represented in a model that will be used to assess the effect of plasma rotation on the mode. Quantitative results based on the theoretical extensions and models of Sections 6.2 and 6.3 are contained in Section 6.4. Finally, the results of this chapter are summarized, and the implications on fusion research are discussed in Section 6.5.

6.1 Leading Order Equilibrium Flow in Tokamak Plasmas

This section is dedicated to a description of toroidal plasma rotation in tokamaks. Potentially the largest contribution is caused by the equilibrium electric field. However, in this investigation, its size is limited to a scaling comparable with the ion diamagnetic frequency. To include diamagnetic rotation, the equilibrium fluid velocity is resolved by considering the ideal limit of Eq. (2.50), i.e. ideal Ohm's law with the Hall term and electron diamagnetic effects. The perpendicular components are identified as

$$\boldsymbol{u}_\perp = \boldsymbol{u}_\Phi + \boldsymbol{u}_{*pi}$$

with

$$\boldsymbol{u}_\Phi = -\frac{\boldsymbol{\nabla}\Phi \times \boldsymbol{B}}{B^2} \quad , \quad \boldsymbol{u}_{*pi} = -\frac{\boldsymbol{\nabla} P_i \times \boldsymbol{B}}{eZn_i B^2},$$

$\boldsymbol{E} = -\boldsymbol{\nabla}\Phi$ and Φ the equilibrium electrostatic potential. Assuming as usual that P_i and Φ are only radially dependent, and upon writing $u_\perp \boldsymbol{e}_\perp = u_{\perp\theta}\boldsymbol{e}_\theta + u_{\perp\phi}\boldsymbol{e}_\phi$, the perpendicular fluid velocity components are simply

$$u_{\perp\theta} = \frac{\left(\Phi' + \frac{P_i'}{eZn_iB_0}\right) B_\phi}{B^2} \quad \text{and} \quad u_{\perp\phi} = -\frac{\left(\Phi' + \frac{P_i'}{eZn_iB_0}\right) B_\theta}{B^2}. \tag{6.1}$$

where $' \equiv \partial/\partial r$. Equation (6.1) suggests that the poloidal flow dominates over the toroidal flow (since $B_\theta \sim \varepsilon B_\phi$). However, it is well recognized that parallel viscosity strongly damps the poloidal plasma rotation. The effect this has on the parallel dynamics can be obtained via Eq. (6.1) and the constraint $u_\theta = 0$. The various components of $\boldsymbol{u}$ are shown in Fig. 6.1.

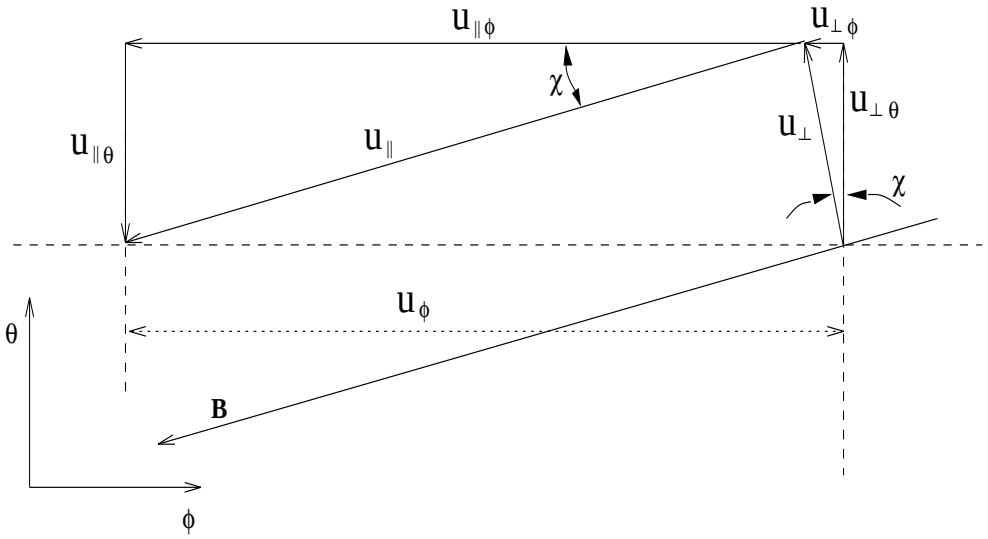

Figure 6.1: Typical fluid velocity components with the constraint $u_\theta = 0$.

Setting $u_\theta = 0$ gives $u_{\|\theta} = -u_{\perp\theta}$. From inspection of Fig. 6.1 it is also clear that $\tan\chi = u_{\perp\phi}/u_{\perp\theta} = u_{\|\theta}/u_{\|\phi}$. Since $u_\phi = u_{\|\phi} + u_{\perp\phi}$ one easily obtains the toroidal fluid velocity:

$$u_\phi = -\frac{u_{\perp\theta}^2}{u_{\perp\phi}}\left(1 - \left(\frac{u_{\perp\phi}}{u_{\perp\theta}}\right)^2\right). \tag{6.2}$$

Hence, using $q = rB_\phi/RB_\theta$ and Eq. (6.1), the toroidal plasma rotation frequency $\Omega = u_\phi/R$ is approximately given by:

$$\Omega = \Omega_\Phi + \omega_{*pi} \tag{6.3}$$

with

$$\Omega_\Phi = -\frac{q\Phi'}{B_0 r} \text{ and } \omega_{*pi} = -\frac{qP_i'}{eZn_iB_0r}. \tag{6.4}$$

The components Ω_Φ and ω_{*pi} are the same sign providing the equilibrium electric field is positive, or, to the contrary, the electrostatic and diamagnetic contributions are in opposition if the electric field is negative.

The dispersion relation of Eq. (4.19) already accounts for the diamagnetic contribution of plasma rotation. These effects enter the dispersion relation through δW_{ki}^e and the inertia. In the following section a new dispersion relation is derived which also accounts for the plasma rotation caused by the equilibrium electric field. It will become clear that for the general case where $\Phi' \neq 0$, the dispersion relation is explicitly dependent on both Ω_Φ and ω_{*pi}.

6.2 Extensions of the Dispersion relation to Include finite Ω_Φ

Before considering the effects of Ω_Φ on the internal kink mode, it is important to first consider the comparative sizes of the other frequencies often included in δW_{ki}. In most of the regimes examined in Section 6.4 it is found that $\Re\{\omega\} \equiv \omega_r \sim \omega_{*pi}$, and in addition the thermal ion temperatures typically exceed 10 keV. Such enhanced ion temperatures ensure that whilst ω_{*pi} is large, the effective collision frequency of trapped thermal ions ν^{ii}_{eff} is, in comparison, relatively low. For many of the regimes considered in Section 6.4 it is found that $\nu^{ii}_{\text{eff}}/\omega_{*pi} \sim \varepsilon_1$, thereby justifying the collisionless limit. Throughout this chapter the collisionless limit is assumed even for temperatures less than 10 keV. This assists in reducing the number of parameters and clarifies the origin of the various trends observed in the results. Also note that the effective electron collision frequency is so large ($\nu^{ee}_{\text{eff}}/\nu^{ii}_{\text{eff}} = \sqrt{m_i/m_e}$, where m_i/m_e is the ion-electron mass ratio) that electrons do not contribute to kinetic behaviour, unlike thermal ions.

In this study the plasma rotation is limited to $\Omega_\Phi \sim \omega_{*pi}$, or equivalently, $E_r \sim \partial P_i/\partial r \,/\, n_i e Z$. In addition to setting up resonances between various natural frequencies, such an ordering serves to simplify the formalism describing internal kink mode stability. Indeed we have already seen that the external fluid potential energy term δW^e_f does not depend directly on the diamagnetic contribution to the equilibrium flow velocity. This is on account of $\boldsymbol{u}_{*pi}$ being small, and furthermore since it is assumed that $\Omega_\Phi \sim \omega_{*pi}$, it follows that the effects of the electrostatically induced flow $\boldsymbol{u}_\Phi$ on δW^e_f can also be neglected. Even at higher velocities where centrifugal effects are taken into account only small alterations to the MHD stability have been calculated [76].

Upon considering the linearly perturbed MHD equations it is clear that the electric field cannot appear explicitly in perturbed fluid potential energy terms, but only indirectly through the equilibrium flow $\boldsymbol{u}$. Whilst, in external fluid terms, the effects of finite flow are very small (and therefore neglected), the effects of finite $\boldsymbol{u}_{*pi}$ on the singular layer term of Eq. (4.18) must be extended to include finite $\boldsymbol{u}_\Phi$. For the external kinetic term δW^e_{ki} the situation is markedly different. Here it is found that the dynamics of single particles are strongly modified by the radial electric field. In particular, an electric field dominates over the magnetic field non-homogeneity effects of trapped precessing particles. Since kinetic quantities constitute single particle and collective resonances, perturbations of kinetic origin are also strongly modified by an electrostatic potential. If no such potential exists the dynamics is somewhat simplified and the standard perturbed kinetic distribution function of Eq. (3.51) applies.

At this point it is valuable to consider again the perturbed distribution function of the external region for the case $\Omega_\Phi = 0$. It is useful to write Eq. (3.51) in the more general and common form [45]:

$$\delta f^e_i = -\boldsymbol{\xi}\cdot\boldsymbol{\nabla} f_i + 2\,\frac{\omega - n\frac{m_i}{Ze}\frac{\partial f_i/\partial\psi\,|_{\mathcal{E}}}{\partial f_i/\partial\mathcal{E}\,|_\psi}}{\omega - n\frac{m_i}{Ze}\frac{\partial \mathcal{J}/\partial\psi\,|_{\mathcal{E}}}{\partial \mathcal{J}/\partial\mathcal{E}\,|_\psi}}\;\left.\frac{\partial f_i}{\partial\mathcal{E}}\right|_\psi \mathcal{E}\,\langle J\rangle\,, \tag{6.5}$$

where $J = \alpha B \boldsymbol{\nabla} \cdot \boldsymbol{\xi}_\perp/2 - \boldsymbol{\xi}_\perp \cdot \boldsymbol{\kappa}(1 - 3\alpha B/2)$, n is the toroidal mode number and $\partial/\partial\mathcal{E}\,|_\psi$ is a partial derivative with respect to $\mathcal{E}$ for constant ψ, where for circular flux surfaces $r\,B_0\,dr = q(r)\,d\psi$. Inspecting the RHS of Eq. (6.5), the first term is the convective component (which gives rise to fluid MHD quantities) and the other term is the perpendicular compressional term (additional kinetic quantity). Kinetic quantities can be recognised through the frequencies

$$\omega_{*i} = \frac{m_i}{Ze}\frac{\partial f_i/\partial\psi\,|_\mathcal{E}}{\partial f_i/\partial\mathcal{E}\,|_\psi} \quad \text{and} \quad \langle\omega_{mdi}\rangle = \frac{m_i}{Ze}\frac{\partial\mathcal{J}/\partial\psi\,|_\mathcal{E}}{\partial\mathcal{J}/\partial\mathcal{E}\,|_\psi}. \tag{6.6}$$

We recall that the numerator of Eq. (6.5) contains the difference between the internal kink mode frequency and the ion diamagnetic frequency. The denominator contains the difference between the kink mode frequency and the magnetic precessional frequency of trapped thermal ions. It is of interest to see how the electrostatic potential modifies these fundamental resonances.

We now turn to the more general scenario where $\Phi \neq 0$. The unperturbed particles now have

$$\mathcal{K} = \mathcal{E} + Ze\Phi/m_i \tag{6.7}$$

as a constant of equilibrium motion. Antonsen and Lee [25] developed a gyro kinetic equation in terms of the slowly varying quantities μ, $\mathcal{K}$, $\mathcal{J}$ and solved the perturbed equation for δf_i. From Ref. [25] one can show that the only changes to Eq. (6.5) that result from the inclusion of non-zero equilibrium electrostatic potential correspond to the transformations $\partial/\partial\mathcal{E}\,|_\psi \longrightarrow \partial/\partial\mathcal{K}\,|_\psi$ and $\partial/\partial\psi\,|_\mathcal{E} \longrightarrow \partial/\partial\psi\,|_\mathcal{K}$. Hence Eq. (6.5) is generalised to

$$\delta f_i^e = -\boldsymbol{\xi}\cdot\boldsymbol{\nabla} f_i + 2\,\frac{\omega - n\frac{m_i}{Ze}\frac{\partial f_i/\partial\psi\,|_\mathcal{K}}{\partial f_i/\partial\mathcal{K}|_\psi}}{\omega - n\frac{m_i}{Ze}\frac{\partial\mathcal{J}/\partial\psi\,|_\mathcal{K}}{\partial\mathcal{J}/\partial\mathcal{K}|_\psi}}\;\left.\frac{\partial f_i}{\partial\mathcal{K}}\right|_\psi \mathcal{E}\,\langle J\rangle\,. \tag{6.8}$$

Note that whilst the kinetic component of the perturbed potential energy is modified, the fluid component is, as expected, unchanged. It is now necessary to explore in more detail how the equilibrium electric field affects the kinetic component of the perturbed distribution function and then relate these changes to the equilibrium plasma rotation Ω_Φ.

6.2.1 δW_{ki}^e and Modifications for finite Ω_Φ

In this section we seek to obtain δf_i^e and subsequently δW_{ki}^e as a function of Ω_Φ. We begin by attempting to define Eq. (6.8) in terms of the ion diamagnetic frequency and magnetic drift precession frequency.

Regardless of whether Φ is finite, the longitudinal invariant

$$\mathcal{J} = \oint v_\parallel dl$$

is conserved and in general one can define the drift precession frequency [56] as:

$$\langle \omega_{di} \rangle = \frac{m_i}{Ze} \frac{\partial \mathcal{J}/\partial \psi \mid_{\mathcal{K}}}{\partial \mathcal{J}/\partial \mathcal{K} \mid_{\psi}}. \tag{6.9}$$

To evaluate (6.9) it is necessary to define the parallel velocity in terms of $\mathcal{K}$ rather than $\mathcal{E}$:

$$v_{\parallel} = \sqrt{2} \left(\mathcal{K} - \mu B - \frac{eZ\Phi}{m_i} \right)^{1/2},$$

thus giving

$$\left. \frac{\partial \mathcal{J}}{\partial \psi} \right|_{\mathcal{K}} = \oint \left(\frac{R v_{\parallel}}{q} \frac{\partial q}{\partial \psi} - \frac{\mu}{v_{\parallel}} \frac{\partial B}{\partial \psi} \right) dl - \frac{eZ}{m_i} \frac{\partial \Phi}{\partial \psi} \oint \frac{1}{v_{\parallel}} dl \quad \text{and} \quad \left. \frac{\partial \mathcal{J}}{\partial \mathcal{K}} \right|_{\psi} = \oint \frac{1}{v_{\parallel}} dl.$$

Again using $r\, B_0\, dr = q(r)\, d\psi$ and referring to Eqs. (3.10), (3.20) and (6.4) it is now clear that

$$\langle \omega_{di} \rangle \equiv \frac{m_i}{Ze} \frac{\partial \mathcal{J}/\partial \psi \mid_{\mathcal{K}}}{\partial \mathcal{J}/\partial \mathcal{K} \mid_{\psi}} = \langle \omega_{mdi} \rangle + \Omega_\Phi. \tag{6.10}$$

Thus, upon including finite Ω_Φ, the bounce averaged drift frequency of trapped ions is modified in exactly the same way as the bulk toroidal plasma rotation Ω. Recalling that a poloidal damping model is used in the derivation of the toroidal plasma rotation, whilst a single particle guiding centre approach is used to highlight the precessional frequency result, the fact that a finite equilibrium electric field produces an identical modification in both Ω and $\langle \omega_{di} \rangle$ is surprising.

We now turn to evaluating the remaining quantity occurring in the numerator of Eq. (6.8). For this application the Maxwellian distribution is required in terms of $\mathcal{K}$:

$$f_i = \frac{n_i \exp\left(Ze\Phi/T_i\right)}{(2\pi T_i)^{3/2}} \exp\left(\frac{-m_i \mathcal{K}}{T_i} \right). \tag{6.11}$$

Referring to Eqs. (6.6) and (6.4) it can be seen that

$$\frac{m_i}{eZ} \frac{\partial f_i/\partial \psi \mid_{\mathcal{K}}}{\partial f_i/\partial \mathcal{K} \mid_{\psi}} = \omega_{*i} + \Omega_\Phi. \tag{6.12}$$

Since Eq. (6.12) contains both ion diamagnetic and electrostatic components with scalings identical to Eq. (6.3) one can interpret Eq. (6.12) as the kinetic analogue of the total toroidal plasma rotation $\Omega = \omega_{*pi} + \Omega_\Phi$.

It is now possible to identify the modifications of the perturbed kinetic distribution function which are attributable to finite Ω_Φ. By Eqs. (6.10) and (6.12) and noting $\partial f_i(r,\mathcal{E})/\partial \mathcal{E} \mid_r \; = \; \partial f_i(r,\mathcal{K})/\partial \mathcal{K} \mid_r$ when f_i is Maxwellian, the kinetic component of Eq. (6.8) becomes

$$\delta f^e_{ki} = 2 \left(\frac{\omega - \Omega_\Phi(r) - \omega_{*i}}{\omega - \Omega_\Phi(r) - \langle \omega_{mdi} \rangle} \right) \frac{\partial f_i}{\partial \mathcal{E}} \mathcal{E} \langle J \rangle, \tag{6.13}$$

on setting $n = 1$.

By comparing Eq. (6.13) with the kinetic component of Eq. (6.5) it is clear that the finite Φ corresponds solely to the simple transformations $\omega_{*pi} \to \omega_{*pi} + \Omega_\Phi$ and $\omega_{mdi} \to \omega_{mdi} + \Omega_\Phi$. This transformation, which holds true throughout the analysis, modifies Eq. (3.59) to

$$\delta W^e_{ki} = -2^{7/2}\pi^3 m_i \left(\frac{\xi_0}{R_0}\right)^2 \int_0^{r_1} dr\, r^2 \int_0^1 dk^2\, \frac{I_q^2}{K_b} \times \int_0^\infty d\mathcal{E}\, \mathcal{E}^{5/2} \frac{\partial f_i}{\partial \mathcal{E}} \left[\frac{\omega - \Omega_\Phi(r) - \omega_{*i}}{\omega - \Omega_\Phi(r) - \langle\omega_{mdi}\rangle}\right], \tag{6.14}$$

where K_b and I_q are defined in Eq. (3.60). Equation (6.14) appears again in Section 6.2.3 where it is required in the generalised dispersion relation.

6.2.2 The Singular Layer and Modifications for finite Ω_Φ

The effects of finite Ω_Φ on the kinetic potential energy contribution to the external region have now been calculated. In addition, it was shown that finite Ω_Φ has no effect on the fluid contribution of the external region. In contrast, this section demonstrates that in the singular layer, finite Ω_Φ modifies both fluid and kinetic terms.

In Section 6.2.1 it was noted that finite Φ modifies kinetic quantities merely with respect to the transformations $\omega_{*pi} \to \omega_{*pi} + \Omega_\Phi$ and $\omega_{mdi} \to \omega_{mdi} + \Omega_\Phi$. It therefore follows that we are at liberty to generalise the gyro kinetic equation of Eq. (3.40) as follows:

$$v_\parallel \frac{\partial \delta f_{ki}}{\partial l} - i(\omega - \omega_{mdi} - \Omega_\Phi)\delta f_{ki} - i(\omega - \omega_{*i} - \Omega_\Phi)\frac{\partial f_i}{\partial \mathcal{E}}\left[v_\parallel^2 + \mu B\right]\frac{\boldsymbol{\xi}_{\perp 0}\cdot\boldsymbol{\nabla} B}{B} = 0. \tag{6.15}$$

An element of care is required when implementing the transformations $\omega_{*pi} \to \omega_{*pi} + \Omega_\Phi$ and $\omega_{mdi} \to \omega_{mdi} + \Omega_\Phi$ in δW^s_{ki}. Specifically, in Section 4.1.1 it is argued that $\omega_{*i}(r_1) \gg \omega_{mdi}(r_1)$, and as a result the dependence of δf^s_{ki} and δW^s_{ki} on ω_{mdi} was removed. To get around this minor obstacle we note that Eq. (6.15) suggests the equivalent transformation $\omega \to \omega - \Omega_\Phi$. Hence, Eq. (4.16) is modified to

$$\delta W^s_{ki} = -2\pi^2 R_0 \int_s dr\, r(\hat{\xi}^s_\theta)^2 \rho \Delta(\omega - \Omega_\Phi)(\omega - \omega_{*pi} - \Omega_\Phi). \tag{6.16}$$

The remaining part of the dispersion relation that requires consideration is the fluid contribution to the singular layer, i.e. $\delta W^s_f + \delta K^s_\perp$. The effects of finite Ω_Φ are established by noting that the inertia $\delta K^s_\perp$ is most conveniently calculated in the absence of an electrostatic potential [21]. This can be arranged by transforming the eigenvalue ω to a frame moving with the toroidal rotation Ω_Φ, i.e. $\omega \to \omega - \Omega_\Phi$, and thus modifying Eq. (2.56) to [21]:

$$\gamma_I^2 = -(\omega - \Omega_\Phi)(\omega - \omega_{*pi} - \Omega_\Phi)|_{r_1}. \tag{6.17}$$

Aside form this transformation, $\delta W^s_f + \delta K^s_{\perp i} \propto \gamma_I$ is unchanged, i.e. both $\delta W^s_f + \delta K^s_\perp$ and δW^s_{ki} are modified in exactly the same way. Consequently, Eq. (4.18) which describes $D^s = \delta W^s_f + \delta K^s_\perp + \delta W^s_{ki}$ is still valid, but now with γ_I defined by Eq. (6.17) above.

6.2.3 The Generalised Dispersion Relation

The various components of the dispersion relation have now been modified to account for the effects of finite Ω_Φ. From Eqs. (6.8), (6.14) and (6.17), it can be seen that the dispersion relation of Eq. (4.19) is generalised as follows:

$$D(\tilde{\omega}) = -i \left. \frac{\sqrt{\tilde{\omega}(\tilde{\omega} - \omega_{*pi})}}{\omega_A} \right|_{r_1} + \varepsilon_1^2 \frac{3\pi}{s_1\sqrt{1+\Delta}} \left[\delta\hat{W}_f + \delta\hat{W}_{ki}(\tilde{\omega}) \right] = 0, \tag{6.18}$$

where the transformed eigenmode is defined,

$$\tilde{\omega} = \omega - \Omega_\Phi(r_1), \tag{6.19}$$

and dropping the 'e' superscript notation:

$$\delta W_{ki}(\tilde{\omega}) = -2^{7/2}\pi^3 m_i \left(\frac{\xi_0}{R_0}\right)^2 \int_0^{r_1} dr\, r^2 \int_0^1 dk^2\, \frac{I_q^2}{K_b} \times \int_0^\infty d\mathcal{E}\, \mathcal{E}^{5/2} \frac{\partial f_i}{\partial \mathcal{E}} \left[\frac{\tilde{\omega} - [\omega_{*i} + \Omega_\Phi(r) - \Omega_\Phi(r_1)]}{\tilde{\omega} - [\langle\omega_{mdi}\rangle + \Omega_\Phi(r) - \Omega_\Phi(r_1)]} \right]. \tag{6.20}$$

In Section 6.4 the above generalised dispersion relation is solved numerically for various regimes inferred from the models and parameters described in Section 6.3.

For the present it is of interest to bring to light some of the more obvious characteristics regarding the generalised dispersion relation. Consider a case where $\Omega_\Phi \gg \tilde{\omega}$. If Ω_Φ is large enough, the square bracket of Eq. (6.20) will approach unity and consequently the dependence of $\delta\hat{W}_{ki}$ on Ω_Φ, $\tilde{\omega}$, ω_{*pi} and $\langle\omega_{mdi}\rangle$ will be lost. This result is identical to the Kruskal and Oberman limit [22] of $\tilde{\omega} \to \infty$, which yields the rather simple stability criterion of Eq. (2.2).

Now consider a case where the magnitude of Ω_Φ is comparable with $\tilde{\omega}$, ω_{*pi} and $\langle\omega_{mdi}\rangle$, but the radial profile of Ω_Φ is not sheared, i.e. $\Omega_\Phi(r) = \Omega_\Phi(r_1)$. By inspection, it can be seen that if Ω_Φ is not sheared, the dispersion relation $D(\tilde{\omega})$ is independent of the magnitude of Ω_Φ. This result is intuitive, since it is clear that $\omega = \tilde{\omega} + \Omega_\Phi(r_1)$ represents the translation of a reference rigidly moving relative to the laboratory frame.

In general however Ω_Φ is sheared. Experimentally it is found that Ω_Φ is peaked at the plasma centre and drops off towards the plasma edge. For such an equilibrium it can be seen from Eq. (6.20) that δW_{ki} and hence $D(\tilde{\omega})$ are sensitive to small changes in Ω_Φ, particularly for the most interesting regimes in which $\tilde{\omega} \sim \omega_{*pi} \sim \langle\omega_{mdi}\rangle \sim \Omega_\Phi$.

Understanding why the dispersion relation is sensitive to sheared toroidal plasma rotation requires a reminder of the two major modifications to D. Single particles are strongly affected by the equilibrium electric field. This is reflected by the local dependence of δW_{ki} on Ω_Φ. However, when considering the effects of Ω_Φ on the inertia, it becomes clear that the internal kink mode is unique amongst ideal MHD modes because the inertia only contributes to the dispersion relation within the singular layer, and consequently the Doppler shift observed in $\delta K_\perp$ (and $\delta W_f^s + \delta W_{ki}^s$) corresponds to the equilibrium electric field located at r_1. Therefore, since part of the dispersion

relation is dependent on the local value of Ω_Φ and another part on $\Omega_\Phi(r_1)$, sheared toroidal plasma rotation necessarily introduces non-trivial modifications with regard to the stability of the internal kink mode in the banana regime.

6.3 Modelling the Effects of Plasma Rotation on Stability

This section describes the models and choice of parameters used to obtain the numerical results of Section 6.4. Such a discussion is required because the dispersion relation of Eq. (6.18) involves a large number of parameters, and choices have to be made regarding the best way to present the numerical results.

A convenient way to reduce the size of the problem is to determine internal kink stability close to marginal threshold conditions. Whilst this does restrict information concerning growth rates, it enables a thorough study of the ideal sawtooth trigger. In response to this, the models described in this section and the numerical results of Section 6.4 are based on conditions close to marginal stability.

6.3.1 Modelling δW_{ki} at Marginal Stability

Appendix B describes various analytical reductions to δW_{ki}. In particular, at marginal stability (where $\Im\{\omega\} = 0$) the relatively simple expressions defined by Eqs. (B.8) and (B.11) represent $\Re\{\delta W_{ki}\}$ and $\Im\{\delta W_{ki}\}$ exactly. The remaining pitch angle and radial integrals have to be evaluated numerically.

Since a great deal of effort has been made to present a tractable means of integrating δW_{ki} exactly, it is appropriate to employ accurate representations of the pitch angle dependent quantities I_q and $\langle\omega_{mdi}\rangle$.

I_q, defined in Eq. (3.60), is a rather complicated quantity. A two dimensional fit in k^2 and q is employed [77] which takes account of the logarithmic singularity in pitch angle at the trapped-passing boundary $k^2 = 1$. It is accurate to within 0.01 percent for $0.5 < q < 1$ and $0 < k^2 < 1$. Writing

$$I_q = \frac{1}{\pi}\sqrt{\frac{2}{\varepsilon}}F_q(q,k^2),$$

the following fit is henceforth used [77],

$$\begin{aligned} F_q(q,k^2) \;=\; & [2E(k^2) - K(k^2)] - \frac{4(1-q)\cos(\pi q)}{1-4(1-q)^2}[E(k^2) + (k^2-1)K(k^2)] \\ & - (1+\cos(\pi q))f_1(q)\left[E(k^2) + (k^2-1)K(k^2) + \frac{2}{\pi}E(k^2) - 1\right] \\ & - (1+\cos(\pi q))[E(k^2) - K(k^2)] - f_2(q)(1-k^2)\left[\frac{\pi}{2} - K(k^2)\right], \end{aligned} \tag{6.21}$$

with

$$f_1(q) = \frac{\pi}{2}\left[1.0841 - 0.3193(1-q)^2 - 0.0683(1-q)^4\right],$$
$$f_2(q) = 5.1\left(q - \frac{1}{2}\right)(1-q)^2\left[1 - 0.034(1-q)\right].$$

For the cases where β is relatively large it is appropriate to include the effects of Shafranov shifted circular flux surfaces on the magnetic drift of trapped ions [78]. Unlike most other studies where the effects of finite pressure on trapped ion orbits have been ignored, the definition of $\langle\omega_{mdi}\rangle$ used in the computations of Section 6.4 reflect finite β. Referring to Connor *et al* [78]:

$$\langle\omega_{mdi}\rangle = \frac{qm_i\mathcal{E}}{eZB_0R_0\,r}\left[F_1 + 2sF_2 - \zeta\left(\frac{1}{4q^2} + F_3\right)\right], \tag{6.22}$$

where $F_{1,2,3}$ are defined in terms of complete elliptic integrals of the the first and second kind,

$$F_1 = 2E(k^2)/K(k^2) - 1,$$
$$F_2 = 2E(k^2)/K(k^2) + 2(k^2-1),$$
$$F_3 = \frac{4}{3}[(2k^2-1)E(k^2)/K(k^2) + (1-k^2)]. \tag{6.23}$$

The modifications of $\langle\omega_{mdi}\rangle$ relative to the shifting of magnetic flux surfaces are identified with the last term in the square brackets of Eq. (6.22) in which

$$\zeta = -\frac{2R\mu_0}{B^2}\frac{dp}{dr}q^2. \tag{6.24}$$

Setting $\zeta = 0$ obtains Eq. (3.61).

The kinetic potential energy terms $\Re\{\delta W_{ki}\}$ and $\Im\{\delta W_{ki}\}$ of Eqs. (B.8) and (B.11) are evaluated in terms of the above definitions of I_q and $\langle\omega_{mdi}\rangle$. To facilitate the radial integration, the profiles of various parameters are also required. Such quantities, most of which are also required in fluid terms, are defined later.

6.3.2 Modelling the Internal Kink Mode Close to Marginal Stability

This section seeks to provide a means of analysing the stability of the internal kink when the mode is close to the marginal boundary. The various models described below are employed in Section 6.4.

At marginal stability, Eq. (6.18) describes two different modes. One of these is embedded in the Alfvén continuum, which requires either $\tilde{\omega} > \omega_{*pi}$ or $\tilde{\omega} < 0$. Assuming this to be the case, the imaginary and real parts of Eq. (6.18) respectively reveal

$$\left.\frac{s\sqrt{1+\Delta}}{3\,\pi\,\varepsilon^2}\,\frac{\sqrt{\tilde{\omega}(\tilde{\omega}-\omega_{*pi})}}{\omega_A}\right|_{r_1} - \Im\left\{\delta\hat{W}_{ki}\right\} = 0 \tag{6.25}$$

$$\delta\hat{W}_f + \Re\left\{\delta\hat{W}_{ki}\right\} = 0. \tag{6.26}$$

Equation (6.25) describes a balance between Alfvén continuum damping and the ion Landau drive. In this respect the marginally stable mode embedded in the continuum resembles the fishbone instability discussed by Chen *et al* [28]. The other mode, is henceforth labelled the 'gap mode'. This mode experiences no continuum damping, since its frequency lies in the low frequency diamagnetic gap in the Alfvén continuum $0 < \tilde{\omega} < \omega_{*pi}$. At marginal stability the gap mode is neither continuum or Landau damped. Hence for $0 < \tilde{\omega} < \omega_{*pi}$, the imaginary and real parts of Eq. (6.18) yield:

$$\Im\left\{\delta\hat{W}_{ki}\right\} = 0 \tag{6.27}$$

$$\left.\frac{s\sqrt{1+\Delta}}{3\,\pi\,\varepsilon^2}\,\frac{\sqrt{\tilde{\omega}(\omega_{*pi}-\tilde{\omega})}}{\omega_A}\right|_{r_1} + \delta\hat{W}_f + \Re\left\{\delta\hat{W}_{ki}\right\} = 0. \tag{6.28}$$

In the case of Gap Modes, the effects of finite Larmor radius provides additional internal kink stability through the positive definite inertial term in Eq. (6.28). Both gap and continuum modes are observed in Section 6.4.

In this chapter the stability of the internal kink mode is gauged chiefly via evaluation of the critical poloidal beta β_p^c. This classical quantity is chosen partly because the computation for β_p^c necessarily requires marginal stability, and partly for historical reasons [15]. In line with this approach the fluid potential energy $\delta\hat{W}_f$ is henceforth defined by Eq. (A.1) throughout the numerical evaluations of Section 6.4. However, it is appropriate to point out that a unique value for β_p^c cannot be obtained from a dispersion relation that includes kinetic effects, since in addition to the pressure (and hence β_p^c), δW_{ki} also depends strongly on the ratio of central temperature with central density and their respective profiles.

The uncoupling of the density and temperature from the pressure can be observed in Eqs. (B.8) and (B.11). It can be seen that $\Re\{\delta W_{ki}\}$ and $\Im\{\delta W_{ki}\}$ depend on a factor proportional to $T_i/[\omega - \Omega_\Phi(r)]$. The dependency of δW_{ki} on $T_i/[\omega - \Omega_\Phi(r)]$ can be removed by assuming the Kruskal and Oberman limit [22] ($\omega - \Omega_\Phi \to \infty$) or the limit used throughout Chapter 5 ($\omega - \Omega_\Phi \to 0$). However, in this chapter the regime of interest corresponds to $\tilde{\omega} \sim \omega_{*pi} \sim \langle\omega_{mdi}\rangle \sim \Omega_\Phi$, and as a result a model must be assigned for the identification of β_p^c. Throughout Section 6.4 β_p^c is evaluated by keeping the central density n_0 and the density and temperature profiles constant, thereby satisfying the marginally stable dispersion relation by first evaluating the unique critical mode frequency $\tilde{\omega}^c$ and the temperature T_0^c. Henceforth $T_0 \equiv T_{i0} = T_{e0}$ will be assumed.

The model used to identify β_p^c follows from the fact that the central temperature is the variable most commonly associated with the sawtooth trigger mechanism. This point can be stressed in two ways. Firstly, as we have seen in Chapter 5 the central temperature evolves considerably during the sawtooth cycle, and secondly T_0 can be amplified via auxiliary heating. The plasma density on the other hand does not evolve by the same degree. In addition to identifying β_p^c, the internal kink mode trigger can be analysed by evaluating perturbed growth rates for conditions close to the stability boundary. To achieve this aim $\tilde{\omega}$ and T_0 are perturbed about $\tilde{\omega}^c$ and T_0^c as follows

$$T_0 = T_0^c + \delta T_0,$$

$$\tilde{\omega} = \tilde{\omega}^c + \delta\omega,$$

where $\tilde{\omega}^c$ is real and $\delta\omega$ imaginary. Since the dispersion relation $D(\tilde{\omega}, T_0^c) = 0$, one obtains

$$\delta\omega \frac{\partial D}{\partial \tilde{\omega}}\bigg|_{T_0^c,\tilde{\omega}^c} + \delta T_0 \frac{\partial D}{\partial T_0}\bigg|_{T_0^c,\tilde{\omega}^c} + O(\delta^2) \;=\; 0.$$

Although $\tilde{\omega}$ is now complex, $\partial/\partial\tilde{\omega}|_{\tilde{\omega}^c}$ can be chosen as an operation along a real path in the complex plane. $\delta\hat{W}_{ki}$ can therefore be differentiated numerically as follows

$$\frac{\partial \delta\hat{W}_{ki}}{\partial\tilde{\omega}}\bigg|_{\tilde{\omega}^c} = \lim_{\delta h\to 0} \frac{\delta\hat{W}_{ki}(\tilde{\omega}^c + \delta h) - \delta\hat{W}_{ki}(\tilde{\omega}^c - \delta h)}{2\delta h},$$

with $\Im\{\delta h\} = 0$. The fact that δh can be chosen to be real means that Eqs. (B.8) and (B.11) can be employed when evaluating $\partial\delta W_{ki}/\partial\tilde{\omega}|_{\tilde{\omega}^c}$. Restricting attention to $\delta\gamma = \Im\{\delta\omega\}$, the normalised quantity,

$$\frac{d\,(\gamma/\omega_A)}{d\,(T_0/T_0^c)} = -\frac{T_0}{\omega_A}\Im\left\{\frac{\partial D}{\partial T_0}\Big/\frac{\partial D}{\partial\tilde{\omega}}\right\}\bigg|_{T_0^c,\tilde{\omega}^c}, \tag{6.29}$$

is calculated using the following parameters,

$$\begin{aligned}
A_{cont} &= \frac{s\sqrt{1+\Lambda}}{6\pi\varepsilon^2}\left[\frac{2\,\tilde{\omega}^c - \omega_{*pi}}{\sqrt{\tilde{\omega}^c(\tilde{\omega}^c - \omega_{*pi})}}\right]\bigg|_{r_1,T_0^c},\\
A_{gap} &= \frac{s\sqrt{1+\Lambda}}{6\pi\varepsilon^2}\left[\frac{\omega_{*pi} - 2\,\tilde{\omega}^c}{\sqrt{\tilde{\omega}^c(\omega_{*pi} - \tilde{\omega}^c)}}\right]\bigg|_{r_1,T_0^c},\\
B &= \omega_A\frac{\partial}{\partial\tilde{\omega}}\left[\Re\{\delta\hat{W}_{ki}\}\right]\Big|_{T_0^c,\tilde{\omega}^c},\\
C &= -\,\omega_A\frac{\partial}{\partial\tilde{\omega}}\left[\Im\{\delta\hat{W}_{ki}\}\right]\Big|_{T_0^c,\tilde{\omega}^c},\\
E &= -\left(\delta\hat{W}_{f2}\,\beta_p^c + 2\,\delta\hat{W}_{f3}\beta_p^{c2}\right)\Big/\,3\Big|_{T_0^c},\\
F &= -T_0\frac{\partial}{\partial T_0}\left[\Re\{\delta\hat{W}_{ki}\}\right]\Big|_{T_0^c,\tilde{\omega}^c},\\
G &= T_0\frac{\partial}{\partial T_0}\left[\Im\{\delta\hat{W}_{ki}\}\right]\Big|_{T_0^c,\tilde{\omega}^c},\\
H_{cont} &= \frac{s\sqrt{1+\Lambda}}{6\pi\varepsilon^2}\left[\frac{\tilde{\omega}^c\,\omega_{*pi}}{\omega_A\sqrt{\tilde{\omega}^c(\tilde{\omega}^c - \omega_{*pi})}}\right]\bigg|_{r_1,T_0^c},\\
H_{gap} &= -\,\frac{s\sqrt{1+\Lambda}}{6\pi\varepsilon^2}\left[\frac{\tilde{\omega}^c\omega_{*pi}}{\omega_A\sqrt{\tilde{\omega}^c(\omega_{*pi} - \tilde{\omega}^c)}}\right]\bigg|_{r_1,T_0^c},
\end{aligned}$$

where $\delta\hat{W}_{f2}$ and $\delta\hat{W}_{f3}$ are defined by Eq. (A.2). Finding the imaginary component of Eq. (6.29) yields the following results: in the continuum,

$$\frac{d\,(\gamma/\omega_A)}{d\,(T_0/T_0^c)} = \frac{(A_{cont}+C)(E+F) - B(G+H_{cont})}{(A_{cont}+C)^2 + B^2}, \tag{6.30}$$

and in the gap,

$$\frac{d\,(\gamma/\omega_A)}{d\,(T_0/T_0^c)} = \frac{C(E+F+H_{gap}) - (A_{gap}+B)G}{C^2 + (A_{gap}+B)^2}. \tag{6.31}$$

In Section 6.4 β_p^c is calculated by solving the dispersion relation of either Eqs. (6.25) and (6.26) or Eqs. (6.27) and (6.28). In addition, for some cases the sign and magnitude of the growth rate is evaluated for conditions close to marginal stability using either Eq. (6.30) or Eq. (6.31).

6.3.3 Experimental Observations and Parameter Value Assignment

Before the dispersion relation can be solved numerically some of the various quantities that characterise the plasma must be defined. The plasma rotation profile is considered first. Unfortunately, in most experiments the plasma rotation is only measured close to the edge and as a result the profile in the plasma core can only be roughly estimated. However, in wall experiments at DIII-D [79] accurate measurements of the rotation profile were required to explain how the resistive wall mode can be destabilised by decreased plasma rotation at the $q = 3$ surface. Values of the toroidal rotation determined from the measured frequency of Mirnov oscillations are found to agree remarkably well with the fluid rotation, especially in the plasma core [79]. Two profiles, originally depicted in Ref. [79], are shown in Fig. 6.2. In one, the toroidal rotation at the $q = 2$ and $q = 3$ surfaces have been reduced through the strong magnetic braking of an error correction coil, and correspondingly the wall mode is destabilised. However, even in the discharge with weak magnetic braking, the plasma rotation at the $q = 2$ surface, which is located approximately at $r = a/2$, was less than 15 percent of the central rotation. In addition, inside $q = 2$, the profile is observed to be approximately parabolic.

Henceforth in this chapter the profile of $\Omega_\Phi(r)$ is modelled to reflect the characteristics observed in Fig. 6.2. Specifically, we set

$$\Omega_\Phi(r) = \Omega_{\Phi 0}\left[1 - \left(\frac{2r}{a}\right)^2\right], \tag{6.32}$$

The fact that Eq. (6.32) admits a fairly high shear within r_1 means that the effects of finite Ω_Φ on the stability of the internal kink mode are likely to be more critical. Furthermore, the sign of Ω_Φ is also important; in particular, if $\Omega_\Phi > 0$, then both contributions of Ω (Ω_Φ and ω_{*pi}) are in the same direction. Henceforth, $\Omega_\Phi > 0$ is referred so as co-rotation and $\Omega_\Phi < 0$ as counter-rotation.

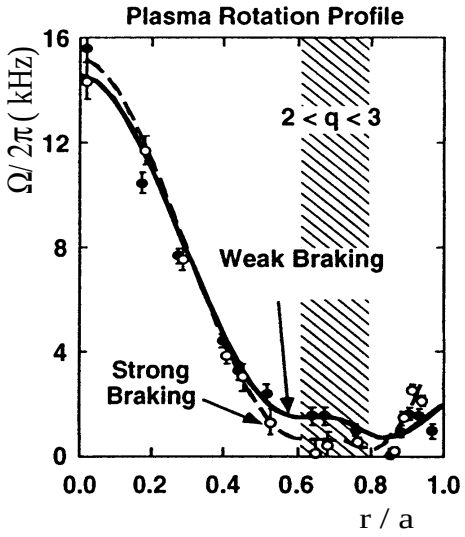

Figure 6.2: Two sheared plasma rotation profiles observed in the DIII-D experiment [79]. This illustrates the parabolic approximation used for $\Omega_\Phi(r)$.

Throughout the numerical results of Section 6.4 the independent variable is chosen to be $\Omega_\Phi(r_1)$, and the central temperature T_0, which must necessarily satisfy the marginally stable dispersion relation, is the dependent variable. However, the relative profiles of the density and temperature are also varied from one plot to the next. It is assumed that $n_i = n_{i0}[1-(r/a)^2]^{\nu_n}$ and $T_i = T_0[1-(r/a)^2]^{\nu_T}$, with $n_i = n_e$, $T_0 \equiv T_{i0}$ and $T_e = T_i$. Different values are assigned to the pressure profile index $\nu_n + \nu_T$ and the parameter

$$\eta_i = \frac{n_i}{T_i}\frac{dT_i}{dr}\left(\frac{dn_i}{dr}\right)^{-1}. \tag{6.33}$$

The following profiles and quantities, modelled on typical JET equilibrium, are fixed throughout Section 6.4: $R_0 = 3\text{m}$, $a = 1.25\text{m}$, $B_0 = 3\text{T}$, $n_{i0} = 4\times 10^{19} m^{-3}$ and $Z = 1$. The safety factor profile is $q = q_0\left[1 + d(r/a)^{2c}\right]^{1/c}$, where $q_0 = 0.7$, $d = 9.09$, $c = 1.33$ giving $r_1 = 0.45\text{m}$ and $q(a) = 5$.

6.4 Numerical Results

It is now time to solve the dispersion relation numerically using the parameters defined in Section 6.3.3. An effort is made to present the most important information regarding the sensitivity of the ideal internal kink mode stability to toroidal plasma rotation. In an attempt to reflect this the results are organised as follows. Section 6.4.1 contains a recipe used throughout the numerical analysis to solve the marginally stable dispersion relation. The recipe is described step by step and a relevant worked example is chosen. In Section 6.4.2 a stability window is found to exist. In forming the stability window a rather obscure 'damped mode' is considered in association with

the mode described in Section 6.4.1. In Section 6.4.3 attention turns to the mode most strongly linked to the sawtooth instability. Here the role of η_i and differing pressure profiles are investigated in association with varying $\Omega_\Phi(r_1)$.

6.4.1 A Numerical Recipe and Application to Numerical Results

We are now in a position to evaluate the stability of the internal kink mode for changing Ω_Φ. The following recipe is used to do this:-
(1) Depending on whether the mode is embedded in the continuum or in the gap, the root of either Eq. (6.25) or Eq. (6.27) is found respectively as a function of two independent parameters T_0 and $\Omega_\Phi(r_1)$. Subsequently a matrix of values of $\tilde{\omega}\left(\Omega_\Phi(r_1), T_0\right)$ is obtained.
(2) The eigenmode matrix $\tilde{\omega}\left(\Omega_\Phi(r_1), T_0\right)$ is substituted into the real kinetic potential energy to give $\Re\{\delta\hat{W}_{ki}\left(\Omega_\Phi(r_1), T_0\right)\}$
(3) Depending on whether the mode is embedded in the continuum or in the gap, either Eq. (6.26) or Eq. (6.28) is solved respectively using (1) and (2) above. Keeping $\Omega_\Phi(r_1)$ as a free parameter the critical central temperature can be identified $T_0^c\left(\Omega_\Phi(r_1)\right)$.
(4) It is then straightforward to evaluate $\beta_p^c\left(\Omega_\Phi(r_1)\right)$ and $\tilde{\omega}^c\left(\Omega_\Phi(r_1)\right)$
(5) Using the quantities $\tilde{\omega^c}\left(\Omega_\Phi(r_1)\right)$ and $T_0^c\left(\Omega_\Phi(r_1)\right)$ it is then possible to calculate $d\left(\gamma/\omega_A\right)/d\left(T_0/T_0^c\right)$ as a function of $\Omega_\Phi(r_1)$.

To illustrate steps (1) - (5) above, and to demonstrate the sensitivity of the internal kink mode stability to changes in $\Omega_\Phi(r_1)$, an example is chosen. We choose to investigate a mode satisfying $\tilde{\omega} > \omega_{*pi}$ in an equilibrium with $\nu_n + \nu_T = 3$ and $\eta_i = 2$. First let us inspect Fig. 6.3. In this figure $\Re\{\delta\hat{W}_{ki}\}$, $\Im\{\delta\hat{W}_{ki}\}$ and the layer term $-\Im\{\hat{D}^s\}$ are plotted against $\tilde{\omega}$ for $\Omega_\Phi(r_1) = 0$ and $T_0 = 10$ keV, where we define:

$$\hat{D}^s = -i\,\frac{s(1+\Delta)^{1/2}}{3\pi\varepsilon^2}\,\frac{\sqrt{\tilde{\omega}(\tilde{\omega}-\omega_{*pi})}}{\omega_A}\Bigg|_{r_1}, \tag{6.34}$$

such that $\hat{D}^s + \delta\hat{W} = 0$. The solution to $\tilde{\omega}(0,10)$ described in step (1) occurs where $\Im\{\delta\hat{W}_{ki}\} = -\Im\{\hat{D}^s\}$, which is shown by the dotted line in Fig. 6.3. This corresponds to one element in the matrix of $\tilde{\omega}\left(\Omega_\Phi(r_1), T_0\right)$ values.

From step (2) and the dotted line of Fig. 6.3 it is clear that $\Re\{\delta\hat{W}_{ki}\left(0,10\right)\} < 0$. The single element $\tilde{\omega}(0,10)$ is not a self consistent solution of Eq. (6.26) (the real component of the dispersion relation) but it does however highlight the sharp peak and trough of $\Re\{\delta\hat{W}_{ki}\}$ and demonstrates how the problem is constructed. Figure 6.4 presents the modification to Fig. 6.3 corresponding to an increase in the toroidal plasma rotation to $\Omega_\Phi(r_1) = 28$k r/s. On this occasion the solution for $\tilde{\omega}$ corresponding to the dotted line occurs at a peak in $\Re\{\delta\hat{W}_{ki}\}$ rather than a trough. Consequently Fig. 6.4 suggests that for the particular choice of equilibrium, co-rotation ($\Omega_\Phi > 0$) provides enhanced stability. The mechanism behind this is simple: the real and imaginary parts of $\delta\hat{W}_{ki}$ are shifted by a frequency $\Omega_\Phi(r) - \Omega_\Phi(r_1)$ as indicated by Eq. (6.20), whereas the inertia term is not shifted.

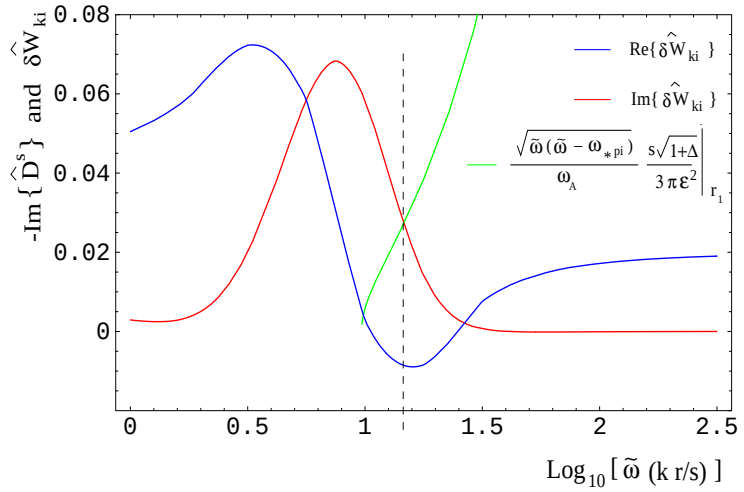

Figure 6.3: Plot of real and imaginary kinetic potential energy terms together with the singular layer term $\hat{D}^s$ as a function of the mode frequency for an equilibrium with $\nu_n + \nu_T = 3$, $\eta_i = 2$, $\Omega_\Phi(r_1) = 0$ and $T_0 = 10$keV. The solution to imaginary component of dispersion relation (Eq. (6.25)) occurs for a value of $\tilde{\omega}$ corresponding to the dotted line.

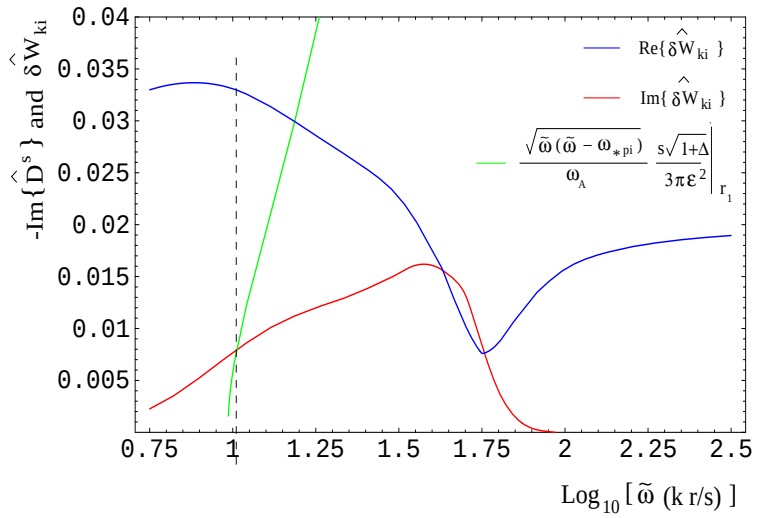

Figure 6.4: As Fig. 6.3 except that $\Omega_\Phi(r_1) = 28$ k r/s.

By going through steps (1) and (2), as shown in Figs. 6.3 and 6.4, for differing T_0 and $\Omega_\Phi(r_1)$ it is possible to satisfy the real component of the dispersion relation of Eq. (6.25). The solutions to steps (3), (4) and (5) are shown in Fig. 6.5.

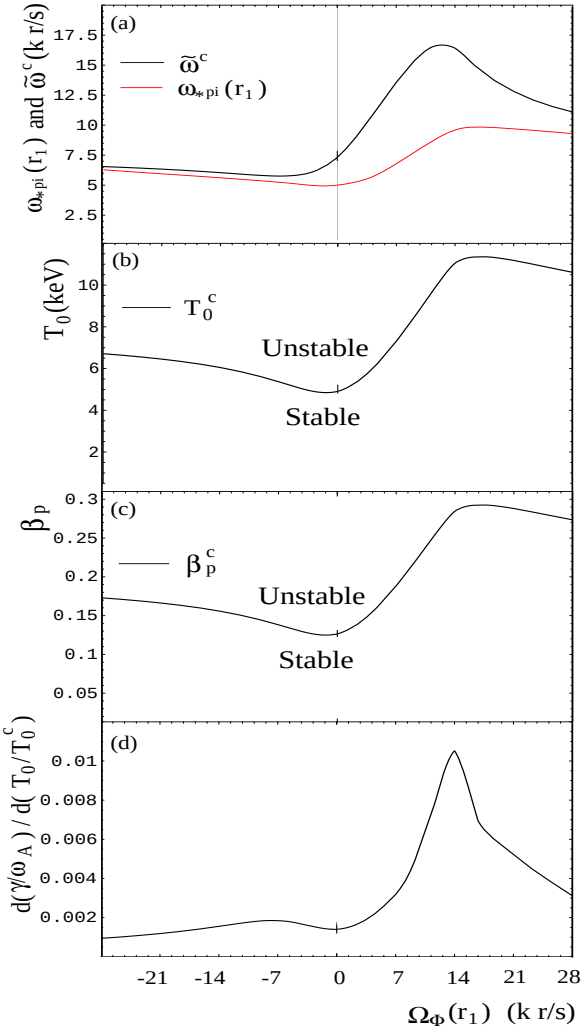

Figure 6.5: A plot of $\tilde{\omega}^c$, $\omega_{*pi}(r_1)$, T_0^c, β_p^c and $d(\gamma/\omega_A)/d(T_0/T_0^c)$ for changing $\Omega_\Phi(r_1)$. The mode corresponds to type $\tilde{\omega} > \omega_{*pi}(r_1)$.

Figure 6.5 (a), (b) and (c) show that $\tilde{\omega^c}$, T_0^c and β_p^c respectively peak at approximately 14 k r/s, whereas the minima approximately corresponds to $\Omega_\Phi(r_1) = 0$. It can be seen that counter-rotation ($\Omega_\Phi(r_1) < 0$) corresponds to only a slight increase in β_p^c, whilst co-rotation ($\Omega_\Phi(r_1) > 0$) provides a much larger enhancement. This enhancement in T_0^c and β_p^c coincides with increasingly stable $\Re\{\delta\hat{W}_{ki}\}$ (see Figs. 6.3 and Fig. 6.4). However, for $\Omega_\Phi(r_1) > 14$ k r/s the magnitude of $\Re\{\delta\hat{W}_{ki}\}$ reduces as it approaches the Kruskal and Oberman limit [22]. In addition, it should also be noted that at the optimised rotation $\Omega_\Phi(r_1) = 14$ kr/s, the perturbed growth rate is also peaked. The plot of $d(\gamma/\omega_A)/d(T_0/T_0^c)$ in Fig. 6.5 (d) indicates that the growth rate will respond five times greater to perturbations about the critical temperature when $\Omega_\Phi(r_1) = 14$ kr/s than when $\Omega_\Phi(r_1) = 0$. Hence, in this example, the desirable

optimised β_p^c is offset by a strong peak in the perturbed growth rate.

6.4.2 Damped Modes and the Stability Window

In Section 6.4.1 the marginal dispersion relation yielded a mode satisfying $\tilde{\omega}^c > \omega_{*pi}$. However, the dispersion relation of Eqs. (6.25) and (6.26) describe at least two coexisting modes. A second mode is investigated in this section, which in conjunction with the mode investigated in Section 6.4.1, can form a stability window in which the plasma is absolutely stable to any ideal internal kink displacements.

The second mode is interesting from a theoretical point of view. At marginal stability the mode must satisfy the imaginary component of the dispersion relation:

$$\left.\frac{s\sqrt{1+\Delta}}{3\,\pi\,\varepsilon^2}\,\frac{\sqrt{\tilde{\omega}(\tilde{\omega}-\omega_{*pi})}}{\omega_A}\right|_{r_1} = \Im\left\{\delta\hat{W}_{ki}\right\}.$$

The exact evaluation of kinetic terms used throughout this chapter demonstrate that $\Im\{\delta\hat{W}_{ki}\}$ contributes significantly to the dispersion relation even for $\tilde{\omega}^c < 0$. For such a mode, with the assumption that $\Omega_\Phi = 0$, contributions from $\Im\{\delta\hat{W}_{ki}\}$ arise as a result of the mode-particle resonance of reverse precessing ions. It is this contribution that allows a mode to exist with $\tilde{\omega}^c < 0$. The effect of non-zero Ω_Φ on $\Im\{\delta\hat{W}_{ki}\}$ is a shift in the resonance to either more deeply reverse magnetically precessing trapped ions or less deeply (even forward magnetically precessing) depending on the sign of Ω_Φ.

The $\tilde{\omega}^c < 0$ mode has a rather unexpected property, namely that it is increasingly damped with respect to enhanced values of β_p. Upon assuming certain limiting approximations, Fogaccia and Romanelli [44] also identified a so called 'damped' mode. One can demonstrate that a mode with $\tilde{\omega}^c < 0$ is a damped mode by considering the perturbed growth rate

$$\delta\gamma = -\delta T_0\,\Im\left\{\frac{\partial D}{\partial T_0}\Big/\frac{\partial D}{\partial\tilde{\omega}}\right\}\Big|_{\tilde{\omega}^c,T_0^c}.$$

Referring to Eq. (6.30) it is clear that if the weak dependence of B and C on $\delta\gamma$ is ignored,

$$\delta\gamma \propto \delta T_0\left|\frac{\partial}{\partial T_0}[\Re\{\delta\hat{W}\}]\right|\Big/\left[\frac{2\,\tilde{\omega}^c-\omega_{*pi}}{\sqrt{\tilde{\omega}^c(\tilde{\omega}^c-\omega_{*pi})}}\right]\Bigg|_{r_1,T_0^c},$$

where the modulus follows from $E+F>0$. Hence, if $\tilde{\omega}^c > \omega_{*pi}$, then $\delta\gamma \propto +\delta T_0$ as expected, whereas if $\tilde{\omega}^c < 0$, then $\delta\gamma \propto -\delta T_0$, i.e. the mode is damped with respect to an enhancement in T_0, or equivalently β_p.

Following the procedure outlined in Section 6.4.1, the dispersion relation can be solved self-consistently for changing $\Omega_\Phi(r_1)$. For clarity the equilibria used in the numerical results of Fig. 6.5 are employed again and the solutions are shown in Fig. 6.6.

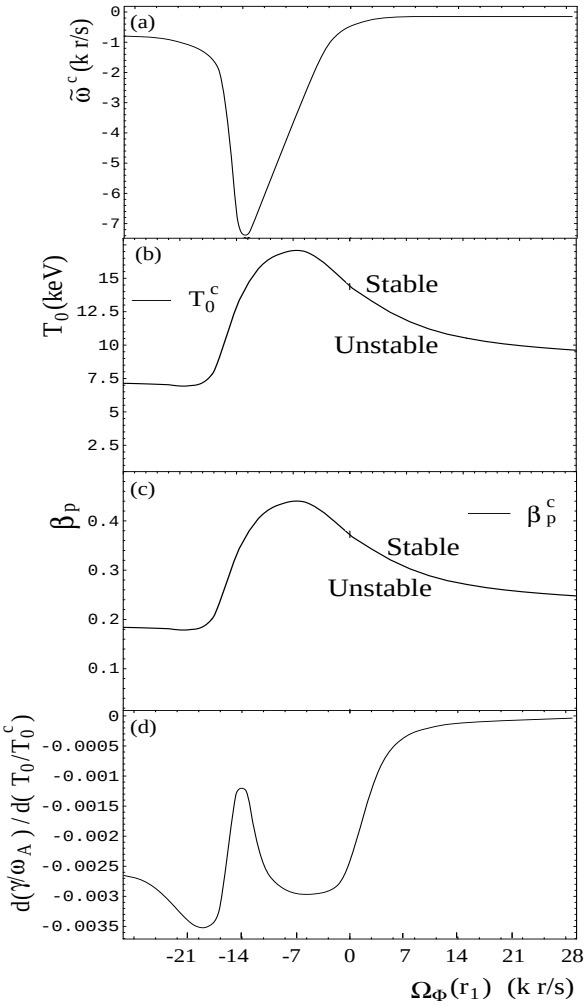

Figure 6.6: Using the equilibria employed in the numerical results of Fig. 6.5, this plot depicts the characteristics of a 'damped mode' i.e. $\tilde{\omega}^c < 0$. (a), (b), (c) and (d) show respectively $\tilde{\omega}^c$, T_0^c, β_p^c and $d(\gamma/\omega_A)/d(T_0/T_0^c)$ for changing $\Omega_\Phi(r_1)$.

For increasing co-rotation ($\Omega_\Phi(r_1) > 0$), kinetic resonances arise from increasingly deeply reversed magnetically precessing ions and as a result $\Im\{\delta W_{ki}\}$ and $\tilde{\omega}^c$ diminish. In addition $\Re\{\delta W_{ki}\}$ approaches the Kruskal and Oberman limit [22], which is smaller than $\Re\{\delta W_{ki}\}$ evaluated for $\Omega_\Phi = 0$. Consequently, a general trend is observed whereby β_p^c is reduced for increasingly positive $\Omega_\Phi(r_1)$.

For small values of counter-rotation. peaks in β_p^c and $|\tilde{\omega}^c|$ exist, which coincides with an enhancement in $\Im\{\delta W_{ki}\}$ due to the resonance of the more populous forward magnetically precessing ions. In addition it can be seen that the sign of $d(\gamma/\omega_A)/d(T_0/T_0^c)$ is always negative indicating that the mode is damped for an enhanced β_p regardless of the magnitude or sign of Ω_Φ.

Coupling the results of Figs. 6.5 (c) and 6.6 (c) provides a stability diagram. Figure 6.7 shows that a narrow stability window exists in which the plasma is absolutely

stable to ideal internal kink displacements. It should be noted that the stability window must necessarily close for sufficiently large Ω_Φ. This is because for $\Omega_\Phi \rightarrow \infty$, both modes approach the Kruskal and Oberman limit [22], which we recall is independent of $\tilde{\omega}^c$ and hence the particular mode in question.

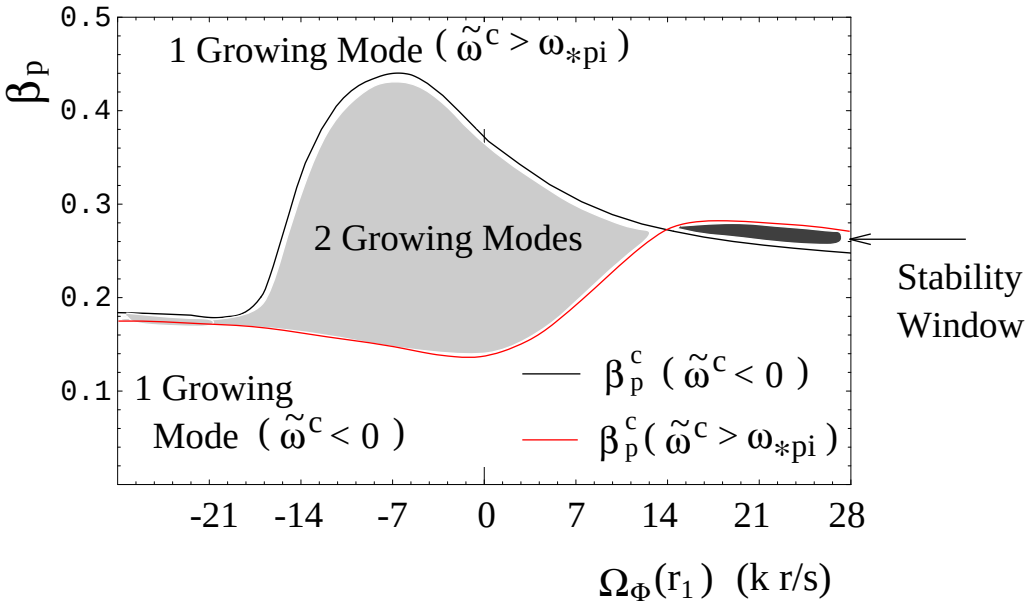

Figure 6.7: Stability diagram collectively featuring the modes shown in Figs. 6.5 and 6.6. A small stability window exists in which the plasma is absolutely stable to internal kink displacements.

6.4.3 Sensitivity of the Ideal Internal Kink Mode Stability Boundary to Changes in $\Omega_\Phi(r_1)$, η_i and the Pressure Profile

Whilst the mode with $\tilde{\omega}^c < 0$ is interesting, its role in an experimental plasma cannot be explained. Indeed, as mentioned in Section 2.4.5, a mode that is unstable at low β_p is likely to be suppressed by only the smallest amount of resistivity. Consequently, interest will be focused on modes that follow the usual convention of becoming increasingly unstable for enhanced β_p. This approach is consistent with the general theme of this thesis, namely an investigation of the sawtooth trigger.

A true investigation of sawtooth stability would not be complete without careful consideration of the effects of η_i, which as shown in Eq. (6.33), characterises the ratio of the temperature shear and the density shear. η_i can vary from one discharge to another, and in addition can evolve greatly during the sawtooth cycle. In this section the range of η_i is limited to typical measured values: $1/4 \leq \eta_i \leq 4$.

We begin by modifying Fig. 6.5 to include differing values of η_i. Figure 6.8 shows five solutions to the dispersion relation, each with $\nu_T + \nu_n = 3$. Fig. 6.8 (a) depicts

the normalised mode frequency $\tilde{\omega}^c/\omega_{*pi}$ verses the normalised plasma rotation

$$\hat{\Omega}_\Phi = \Omega_\Phi(r_1)/\omega_{*pi}(r_1)$$

for differing η_i. Figures depicted in terms of such normalised frequencies are independent of the equilibrium pressure and thus provide more general information than those of Figs. 6.5 and 6.6. In particular the boundary between the Alfvén continuum and the gap is easily located in Fig. 6.8 (a) at $\tilde{\omega}^c/\omega_{*pi}(r_1) = 1$. Other fundamental parameter values can also be identified in Fig. 6.8. For example at $\hat{\Omega}_\Phi = 1$, the total plasma rotation Ω at r_1 receives equal contributions from the pressure and electric field, whilst at $\hat{\Omega}_\Phi = -1$, the total plasma rotation is zero at r_1.

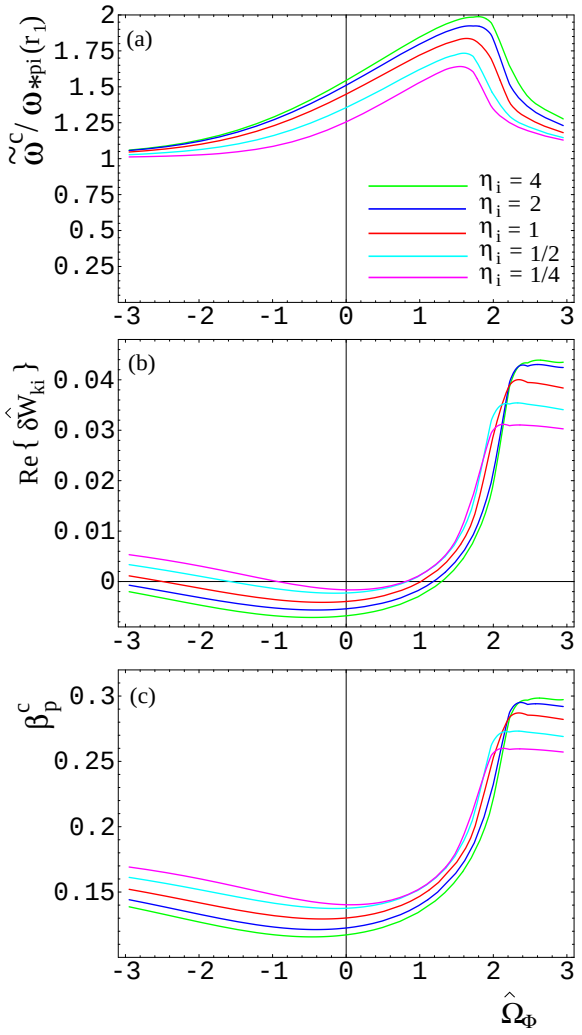

Figure 6.8: Depicting $\tilde{\omega}^c$, $\Re\{\delta\hat{W}_{ki}\}$ and β_p^c verses $\Omega_\Phi(r_1)/\omega_{*pi}(r_1)$ for five different assignments of η_i. In each plot the pressure profile is again controlled by $\nu_T + \nu_n = 3$.

Since both $\Re\{\delta W_{ki}\}$ and β_p^c are proportional to T_0, Figs. 6.8 (b) and (c) assume a similar form. For each η_i, both β_p^c and $\Re\{\delta W_{ki}\}$ are approximately minimised for

$\Omega_\Phi = 0$, and we note that the minimised value of threshold beta corresponds to $\Re\{\delta W_{ki}\} < 0$, whereas β_p^c and $\Re\{\delta W_{ki}\}$ are maximised for $\hat{\Omega}_\Phi \approx 2$. Within the range $-3 < \hat{\Omega}_\Phi < 0$ the threshold beta is only increased slightly for increased counter-rotation.

Interestingly, Fig. 6.8 demonstrates that β_p^c is more sensitive to changes in $\Omega_\Phi(r_1)$ for increased η_i. This trend is amplified when the shear of the pressure profile is reduced. Figure 6.9 illustrates the modifications of Fig. 6.8 corresponding to the adjustment $\nu_T + \nu_n = 3/2$. In particular it can be seen that for $\eta_i = 4$, the magnitude of β_p^c varies by a factor of two within the range $0 < \hat{\Omega}_\Phi < 1$.

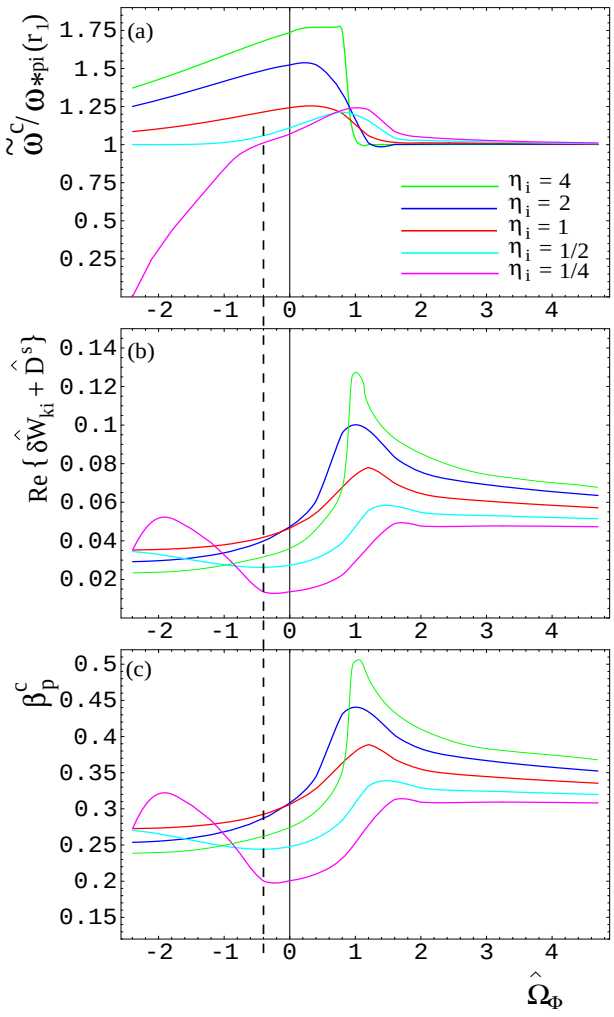

Figure 6.9: As Fig. 6.8 except that pressure profile is controlled by $\nu_T + \nu_n = 3/2$. Note that $\Re\{\hat{D}^s\} = 0$ for modes embedded in the continuum. The dotted line indicates the transition between the gap mode and the embedded mode for $\eta_i = 1/4$.

It is clear from Figs. 6.9 (a), (b) and (c) that for the case of $\eta_i = 4$, the large increases of $\Re\{\delta W_{ki}\}$ and β_p^c correspond to a large change in $\tilde{\omega}^c/\omega_{*pi}$ within a small

range of $\hat{\Omega}_\Phi$. Figure 6.10 illustrates the mechanism behind this by plotting the imaginary components of the dispersion relation of Eq. (6.25) for two values of plasma rotation. For $\hat{\Omega}_\Phi = 0.8$, it can be seen that the solution $\tilde{\omega}$ to Eq. (6.25), satisfied by $\Im\left\{\hat{D}^s + \delta\hat{W}_{ki}\right\} = 0$, occurs where $\Im\{\delta\hat{W}_{ki}(\tilde{\omega})\}$ is close to its maximum. However, as shown in Figs. 6.3 and 6.4, a positive increase in $\hat{\Omega}(r_1)$ has the effect of shifting the kinetic potential energy curves to the left. Since the slope of $\Im\{\delta\hat{W}_{ki}\}$ almost matches the slope of the layer contribution $-\Im\{\hat{D}^s\}$, only a very small change in the value of plasma rotation to $\hat{\Omega}_\Phi = 1$ dramatically reduces the eigenvalue solution $\tilde{\omega}^c/\omega_{*pi}(r_1)$ from approximately 1.75 to slightly greater than unity. Subsequently, the reduction in $\tilde{\omega}^c/\omega_{*pi}(r_1)$ gives rise to an increase in $\Re\{\delta W_{ki}\}$ and β_p^c.

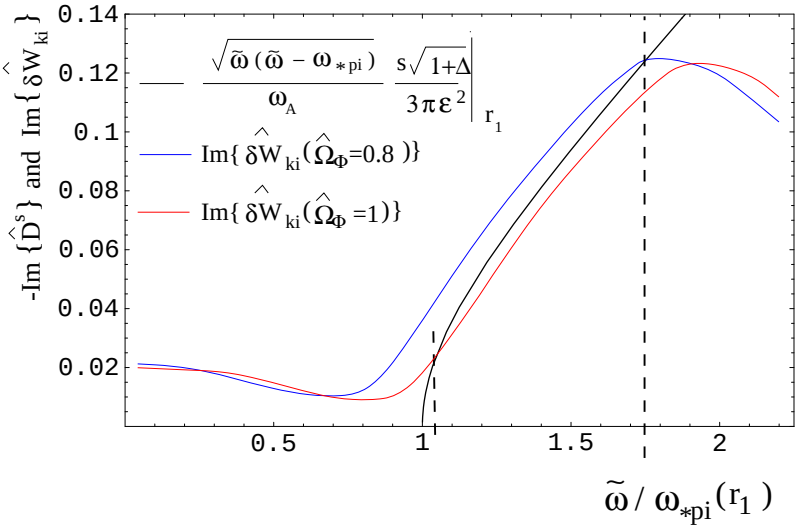

Figure 6.10: Showing how a small change in $\hat{\Omega}_\Phi$ results in a large reduction of $\tilde{\omega}^c/\omega_{*pi}(r_1)$ as observed in Fig. 6.9 (a) for the case of $\eta_i = 4$. Dotted lines indicate solutions to the imaginary part of the dispersion relation.

For all but the case $\eta_i = 1/4$, Fig. 6.9 illustrates that counter-rotation modifies $\Re\{\delta W_{ki}\}$ and β_p^c only slightly. Indeed for these modes, the greatest variation of β_p^c corresponds to changes in the plasma rotation relative to $\Omega_\Phi(r_1) \sim \omega_{*pi}(r_1)$. However, for $\eta_i = 1/4$ with $-2.4 \gtrsim \hat{\Omega}_\Phi \gtrsim -0.5$, the internal kink mode exists in a gap in the Alfvén continuum, i.e. $0 < \tilde{\omega}^c < \omega_{*pi}$. For $\hat{\Omega}_\Phi \lesssim -2.4$ or $\hat{\Omega}_\Phi \gtrsim 0.6$ the mode is embedded in the continuum with respectively $\tilde{\omega}^c < 0$ or $\tilde{\omega}^c > \omega_{*pi}$. As one can see from Eq. (6.28), for gap modes the layer term $\Re\{\hat{D}^s\}$ contributes to the real component of the dispersion relation and has the effect of enhancing β_p^c. For modes with $\tilde{\omega}^c > \omega_{*pi}$, it is clear from Eq. (6.34) that $\Re\{\hat{D}^s\} = 0$, whereas, as confirmed in Fig. 6.9 (a) and (b), for gap modes, $\Re\{\hat{D}^s\}$ is maximised where $\tilde{\omega}^c/\omega_{*pi}(r_1) \approx 1/2$.

The fact that the gap mode appears to be associated with small η_i and counter-rotation is at first rather curious. At marginal stability gap modes satisfy $\Im\{\delta W_{ki}\} =$

0. Figures 6.3, 6.4 and 6.10 show that $\Im\{\delta W_{ki}\} > 0$ for all $\tilde{\omega}$, and hence a gap mode cannot exist. However, it is possible that the condition $\Im\{\delta W_{ki}\} < 0$ can be satisfied for small η_i, thereby introducing the possibility of gap modes. Consider the case where $\Omega_\Phi = 0$. At marginal stability the Landau resonance $\tilde{\omega} = \langle\omega_{mdi}\rangle$ gives rise to the imaginary component of δW_{ki}. In addition, the relative sizes of $\tilde{\omega}$ and ω_{*i} can affect the sign and amplitude of $\Im\{\delta W_{ki}\}$. To see this we write the term $-(\tilde{\omega} - \omega_{*i})/\omega_{*pi}$, which is proportional to the numerator of $\Im\{\delta W_{ki}\}$, as:

$$\frac{1 + \eta_i\left(\frac{m_i\mathcal{E}}{T_i} - \frac{3}{2}\right)}{1 + \eta_i} - \frac{\tilde{\omega}}{\omega_{*pi}}. \tag{6.35}$$

Unless $\tilde{\omega}/\omega_{*pi} \gg 1$, Eq. (6.35), and hence $\Im\{\delta W_{ki}\}$ are both positive. However Eq. (6.35) can change sign for lower values of $\tilde{\omega}/\omega_{*pi}$ providing that η_i is sufficiently small. Setting $\eta_i = 0$, Eq. (6.35) becomes

$$1 - \frac{\tilde{\omega}}{\omega_{*pi}}. \tag{6.36}$$

Hence, for $\eta_i = 0$, a change of sign requires $\tilde{\omega} > \omega_{*pi}$, which is at variance with the definition of the gap mode.

It is possible to change the sign of the numerator within the gap regime $0 < \tilde{\omega} < \omega_{*pi}$ if one includes finite plasma rotation. Equation (6.36) is then modified to

$$1 - \frac{\tilde{\omega} + \Omega_\Phi(r_1) - \Omega_\Phi(r)}{\omega_{*pi}}. \tag{6.37}$$

Assuming that $0 < \tilde{\omega} < \omega_{*pi}$ and $\Omega_\Phi(r)$ has a monotonically decreasing profile, a change of sign in Eq. (6.37) can be obtained if $\Omega_\Phi < 0$, i.e. gap modes require counter-rotation. These statements are illustrated in Fig. 6.11. Here the contrasting dependence of $\Im\{\delta W_{ki}\}$ with respect to $\tilde{\omega}$ are shown for two different values of plasma rotation. The dotted lines represent solutions to the imaginary component of the dispersion relation and are therefore identified with the corresponding points on Fig. 6.9 (a) for the case of $\eta_i = 1/4$. When $\hat{\Omega}_\Phi = 0$, it can be seen that $\Im\{\delta W_{ki}\}$ changes sign only for $\tilde{\omega} > \omega_{*pi}$, and hence the dotted line corresponds to the solution of Eq. (6.25). However, for $\hat{\Omega}_\Phi = -1$, $\Im\{\delta W_{ki}\}$ changes sign within $0 < \tilde{\omega} < \omega_{*pi}$ and hence the dotted line corresponds to the solution of Eq. (6.27), i.e. $\Im\{\delta W_{ki}\} = 0$. This mechanism arises as a result of shifts in the $\delta W_{ki}(\tilde{\omega})$ curves produced by changes in Ω_Φ.

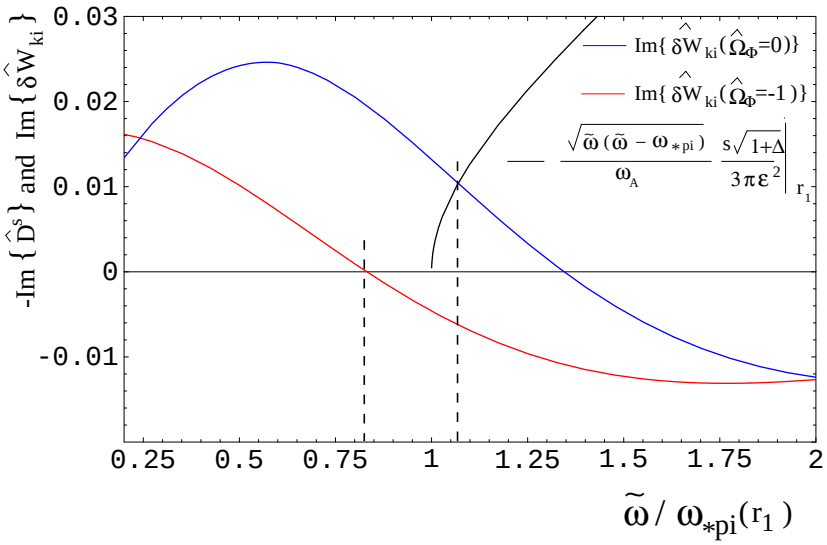

Figure 6.11: Depicting the dependence of $\Im\{\delta W_{ki}\}$ on $\tilde{\omega}$ for differing $\hat{\Omega}_\Phi$. Solutions to the imaginary component of the dispersion relation for the case of $\eta_i = 1/4$ are indicated by dotted lines. For $\hat{\Omega}_\Phi = 0$, the solution is embedded in the continuum ($\tilde{\omega}^c > \omega_{*pi}(r_1)$), whereas for $\hat{\Omega}_\Phi = -1$ the solution lies in the gap of the Alfvén continuum ($0 < \tilde{\omega}^c < \omega_{*pi}(r_1)$).

Figures 6.8 and 6.9 demonstrate that the threshold poloidal beta is an increasingly sensitive function of Ω_Φ for increasing η_i. Comparisons between Figs. 6.8 and 6.9 show that the pressure profile also influences β_p^c. In particular, for a fairly flat profile ($\nu_n + \nu_T = 3/2$), β_p^c is most sensitive to changes in $\hat{\Omega}_\Phi$ about unity, whereas for a more sheared profile ($\nu_n + \nu_T = 3$), larger values of $\hat{\Omega}_\Phi$ are required to produce a similar degree of sensitivity. It has also been shown that if $\Omega_\Phi < 0$ and $\eta_i \ll 1$, the emergence of a mode existing in a gap in the Alfvén continuum can also assist in increasing β_p^c.

6.5 Summary and Discussion

The ideal sawtooth trigger condition has been modified to include the effects of toroidal rotation. The latter, which includes a component Ω_Φ induced from the electric field, is limited to an order similar to that of the thermal ion diamagnetic frequency. The ideal internal kink mode calculations take into account the kinetic response of thermal ions in both the singular layer (close to $q = 1$) and the external region. Modifications arising from the inclusion of Ω_Φ are shown to exist solely in the external kinetic term.

If Ω_Φ is not sheared, there is no effect on the internal kink mode. If Ω_Φ is sheared, the enhancement to the total plasma rotation $\Omega = \Omega_\Phi + \omega_{*pi}$ has the effect of locally shifting $\delta W_{ki}[\tilde{\omega}]$ to $\delta W_{ki}[\tilde{\omega} + \Omega_\Phi(r_1) - \Omega_\Phi(r)]$. For modes with $\tilde{\omega} \sim \omega_{*pi} \sim \langle\omega_{mdi}\rangle$, the

result of a frequency shift $\Omega_\Phi(r) - \Omega_\Phi(r_1) \sim \omega_{*pi}$ is to dramatically modify β_p^c.

Various regimes have been investigated, and in each it is found that β_p^c, the quantity traditionally used to determine the threshold stability of the ideal internal kink, depends sensitively on Ω_Φ. In Section 6.4.2 the dispersion relation was shown to yield two contrasting but coexisting modes. A narrow stability window was found to exist in which both ideal modes are absolutely stable. However, whilst one of the modes ($\tilde{\omega} > \omega_{*pi}$) was found to agree with the conventional internal kink modes, a perturbation analysis revealed that the other mode ($\tilde{\omega} > 0$) is increasingly unstable for decreasing β_p.

In Section 6.4.3 attention turned to the effects of Ω_Φ on the conventional internal kink mode. This study was supplemented with an investigation into the additional effects of density and temperature profiles on threshold stability. In general it was found that β_p^c is an increasingly sensitive function of Ω_Φ for increasing η_i. Provided η_i is not much smaller than one, counter-rotation was shown to have little effect on β_p^c, whereas co-rotation enhanced β_p^c by a factor of two. In particular, upon choosing a relatively flat pressure profile ($\nu_n + \nu_T = 3/2$), β_p^c proved to be very sensitive to small changes in $\Omega_\Phi(r_1)$ when $\Omega_\Phi(r_1) \approx \omega_{*pi}$.

Assuming a flat temperature profile, peaked density profile and counter rotation, it has been possible to explore the stability of a mode existing in the gap of the Alfvén continuum. The diamagnetic stabilisation of the observed gap mode is maximised for $\Omega_\Phi(r_1) \approx -2\omega_{*pi}$. A sufficiently large increase in either counter-rotation or co-rotation shifts the mode out of the gap.

This chapter has demonstrated that finite Ω_Φ has a profound effect on the ideal internal kink stability of plasmas in the banana regime. Furthermore, the results may explain some of the observed interaction between sawtooth stability and plasma rotation. For example, in locked mode experiments a change in the RMP amplitude and a corresponding change in the amplitude and shear of Ω_Φ can remove sawteeth altogether [38]. Moreover, in NBI experiments, a reversal in the direction of the minority ion injection, and corresponding plasma rotation direction, can significantly modify the sawtooth period and amplitude.

The dispersion relation of Eq. (6.18) can easily be modified to include the effects of an NBI population. The additional term $\delta\hat{W}_{kh}(\tilde{\omega})$ is identical to Eq. (6.20) except for the interchange of the thermal ion distribution function, diamagnetic frequency and precessional drift frequency to f_h, ω_{*h} and $\langle\omega_{mdh}\rangle$ respectively. As mentioned in Section 5.5, for NBI experiments the plasma rotation is somewhat larger than that observed in ICRH experiments and the precessional drift frequency is smaller. It is plausible that in many NBI experiments the plasma rotation could be ordered such that $\Omega_\Phi(r_1) \sim \langle\omega_{mdh}\rangle$, and this being the case, the effects of finite sheared Ω_Φ should be included when using internal kink models to interpret sawtooth and fishbone behaviour in NBI discharges.

Chapter 7

Conclusions

The goal of this thesis has been to extend the analysis of the ideal internal kink mode to represent more accurately experimental observation. Recent large experiments, e.g. JET and TFTR, include populations of hot ions, and there has been a pressing need to understand in greater detail the interaction between hot collisionless ion populations and $m = n = 1$ internal kink mode behaviour.

From the comprehensive Historical Overview of Section 2.1 two particularly striking gaps appeared in previous work. One of these is a lack in the implimentation of suitably representative ICRH minority ion distribution functions, and the other is omission of the equilibrium electric field and induced plasma rotation from internal kink calculations. Whilst the earlier chapters of this thesis provided a background regarding the collisionless extensions of the internal kink mode, Chapters 5 and 6 respectively accommodated some of the answers to the former and latter gaps pointed out above.

In Chapter 5 ICRH heated JET DT sawtoothing discharges were compared with a generalised energy principle which describes the ideal internal kink mode stability. Hot minority ion contributions to the internal kink mode were calculated in terms of a new distribution function which accurately represents the anisotropically distributed population. In one study it was found that during the sawtooth cycle, the evolving q profile modifies the stability of the ideal internal kink significantly, and may therefore constitute an important element of the sawtooth crash mechanism. In another study, the minority ion pressure was found to be so large that, together with the stabilising kinetic contribution, the hot ions contributed strongly towards the toroidal destabilisation of the internal kink mode. By carefully accounting for the evolving bulk and minority plasma contributions, a strong correlation emerged between sawtooth duration and both the kinetic stabilisation and toroidal destabilisation of the ideal internal kink mode.

In Chapter 6 the analysis describing the ideal internal kink mode was, for the first time, modified to include the effects of the equilibrium electric field and induced toroidal plasma rotation. The numerical results of Section 6.4 concentrated on exact stability threshold calculations for a plasma in the banana regime. Differing equilibria were investigated, but common to each was the high degree of sensitivity that the internal kink mode exhibited to variations in the sheared toroidal plasma rotation.

This thesis has been successful in extending the analysis that describes the internal kink mode, evaluating more accurately the effects of realistic equilibria, and in some cases interpreting and predicting sawtooth behaviour. However, the models extended and employed in this thesis could themselves be improved, and in so doing, more in-depth investigations could be carried out in the future. For the interpretation of JET sawtoothing discharges, the analysis could be extended to include resistivity. Whilst this would invoke an additional degree of complexity, and perhaps uncertainty (see Section 5.5), it would provide more realistic comparisons between theory and observed sawtooth behaviour. The ideal model of Chapter 6 could be extended in a variety of interesting ways. First, for cases where the thermal ion temperatures are not very high, one could also consider the effects of ion-ion collisions. In addition, rather than an analysis purely based on the marginally stable internal kink mode, the numerical analysis of Section 6.4 could be extended to include the relationship between highly unstable internal kink modes and finite toroidal plasma rotation. Such a study could be particularly important to the experimental interpretation of fishbones, whereby, as mentioned in Section 6.5, the effects of finite plasma rotation on kinetic terms that describe the effects of neutral beam populations could easily be included.

Appendix A

MHD Toroidal and Shaping Contributions to δW

In this appendix the MHD toroidal and shaping contributions to δW are defined. In contrast to the toroidal term of Eq. (2.34), the definitions and calculations defined here are not restricted to a parabolic q profile.

Bussac's [15] expression of the toroidal fluid term is

$$\delta\hat{W}^T = (\delta\hat{W}_{f1} + \delta\hat{W}_{f2}\beta_p + \delta\hat{W}_{f3}\beta_p^2)/3, \tag{A.1}$$

where

$$\delta\hat{W}_{f1} = \frac{\sigma}{2} + \frac{\left[\frac{9}{4}(b^{(2)}-1)(1-c^{(2)}) - 6\sigma(b^{(2)}-1)(c^{(2)}+3) - 4\sigma^2(c^{(2)}+3)(b^{(2)}+3)\right]}{[16(b^{(2)}-c^{(2)})]},$$

$$\delta\hat{W}_{f2} = -\frac{(c^{(2)}+3)[3(b^{(2)}-1)+4\sigma(b^{(2)}+3)]}{8(b^{(2)}-c^{(2)})},$$

$$\delta\hat{W}_{f3} = -\frac{(b^{(2)}+3)(c^{(2)}+3)}{4(b^{(2)}-c^{(2)})}. \tag{A.2}$$

Restricting attention to only elongation (L) and triangular (T) contributions, Edery's [43] shaping contribution to $\delta\hat{W}$ has the from

$$\delta\hat{W}^S = \delta\hat{W}^{SL} + \delta\hat{W}^{ST} \tag{A.3}$$

with

$$\delta\hat{W}^{SL} = \frac{1}{12\varepsilon_1^2}\left[\frac{[L_1' - L_1/r_1]^2\left(b^{(3)}+4\right)\left(c^{(3)}+4\right)}{c^{(3)}-b^{(3)}} + \frac{[L_1'+3L_1/r_1]^2\, b^{(-1)}c^{(-1)}}{c^{(-1)}-b^{(-1)}}\right]$$

and

$$\delta\hat{W}^{ST} = \frac{1}{12\varepsilon_1^2}\left[\frac{[T_1' - 2T_1/r_1]^2\left(b^{(4)}+5\right)\left(c^{(4)}+5\right)}{c^{(4)}-b^{(4)}}\right. \tag{A.4}$$

$$\left. + \frac{[T_1'+4T_1/r_1]^2\left(b^{(-2)}-1\right)\left(c^{(-2)}-1\right)}{c^{(-2)}-b^{(-2)}}\right], \tag{A.5}$$

where, in Eq. (2.25), the loci of non-circular flux surfaces are defined in terms of the elongation $L(r)$ and triangularity $T(r)$. Also, as usual $' \equiv d/dr$ and the subscript '1' denontes evaluation at r_1.

The quantities $b^{(m)}$ and $c^{(m)}$ are defined as

$$b^{(m)} = \frac{r}{\xi^{(m)}} \frac{d\xi^{(m)}}{dr}\bigg|_{r=r_1-} \quad \text{and} \quad c^{(m)} = \frac{r}{\xi^{(m)}} \frac{d\xi^{(m)}}{dr}\bigg|_{r=r_1+}, \tag{A.6}$$

with functions $\xi^{(m)}(r < r_1)$ and $\xi^{(m)}(r > r_1)$ being the solutions of the homogeneous equation for the eigenfunction ξ:

$$\frac{d}{dr}\left[r^3 \left(\frac{1}{q} - \frac{1}{m}\right)^2 \frac{d\xi}{dr}\right] - r(m^2 - 1)\left(\frac{1}{q} - \frac{1}{m}\right)^2 \xi = 0. \tag{A.7}$$

Permissible solutions are regular as $r \to 0$ and $r \to r_2$ (where $q(r_2) = 2$). The boundary conditions $[\xi(0) = 0\,,\, d\xi(0)/dr = 1]$ are used to obtain $b^{(2)}$ and $[\xi(r_2) = 1\,,\, d\xi(r_2)/dr = 0]$ to obtain $c^{(2)}$.

Appendix B

Analytical Reduction of $\delta\hat{W}_{ki}$

This appendix describes the analytical methods used to reduce the complexity of $\Re\{\delta\hat{W}_{ki}\}$ and $\Im\{\delta\hat{W}_{ki}\}$. The simplified but exact definitions of $\Re\{\delta\hat{W}_{ki}\}$ and $\Im\{\delta\hat{W}_{ki}\}$ are employed in the numerical results section of 6.4.

The kinetic perturbed potential energy term of Eq. (6.20) can be written in the form,

$$\delta W_{ki} = -2^{\frac{7}{2}}\pi^3|\xi_{r0}|^2 m_i \frac{1}{R_0^2}\int_0^{r_1} dr r^2 \int_0^\infty d\mathcal{E}\mathcal{E}^{\frac{5}{2}}\int_0^1 dk^2 \frac{I_q^2\left(\omega_{tot}\frac{\partial f_i}{\partial \mathcal{E}} - \frac{q}{r\omega_{ci}}\frac{\partial f_i}{\partial r}\right)}{K_b[\omega_{tot} - \overline{\omega}_{mdi}]}, \quad \text{(B.1)}$$

with $\omega_{tot}(r) = \omega - \Omega_\Phi(r) = \tilde{\omega} + \Omega_\Phi(r_1) - \Omega_\Phi(r)$ and $\omega_{ci} = eZB_0/m_i$. The energy integral can be evaluated analytically if the ions are distributed negative exponentially. Such distributions describe ICRH and thermal ion populations:

$$f_i(r,k,\mathcal{E}) = N(r,k)\exp(-b(r,k)\mathcal{E}), \quad \text{(B.2)}$$

where $b = m_i/T_i$ and $N = n_i m_i^{3/2}/(2\pi T_i)^{3/2}$ for a Maxwellian thermal ion population. By substituting Eq. (B.2) into Eq. (B.1), δW_{ki} contains energy integrals of the form,

$$\int_0^\infty \frac{\mathcal{E}^{\frac{5}{2}}\exp(-b\mathcal{E})}{\omega_{tot} - \mathcal{D}\mathcal{E}}d\mathcal{E}\ ,\ \int_0^\infty \frac{\mathcal{E}^{\frac{7}{2}}\exp(-b\mathcal{E})}{\omega_{tot} - \mathcal{D}\mathcal{E}}d\mathcal{E} \quad \text{(B.3)}$$

where $\langle\omega_{mdi}\rangle = \mathcal{D}(r,k)\mathcal{E}$. At marginal stability

$$\begin{aligned}
\Re\left\{\int_0^\infty \frac{\mathcal{E}^{\frac{5}{2}}\exp(-b\mathcal{E})}{\omega_{tot} - \mathcal{D}\mathcal{E}}d\mathcal{E}\right\} &= \frac{\sqrt{\pi}}{4b^{\frac{7}{2}}\omega_{tot}}\mathrm{Fn}_1(x),\\
\Re\left\{\int_0^\infty \frac{\mathcal{E}^{\frac{7}{2}}\exp(-b\mathcal{E})}{\omega_{tot} - \mathcal{D}\mathcal{E}}d\mathcal{E}\right\} &= \frac{\sqrt{\pi}}{4b^{\frac{9}{2}}\omega_{tot}}\mathrm{Fn}_2(x),\\
\Im\left\{\int_0^\infty \frac{\mathcal{E}^{\frac{5}{2}}\exp(-b\mathcal{E})}{\omega_{tot} - \mathcal{D}\mathcal{E}}d\mathcal{E}\right\} &= -\frac{\pi}{\omega_{tot}b^{\frac{7}{2}}}\mathrm{Fn}_3(x),\\
\Im\left\{\int_0^\infty \frac{\mathcal{E}^{\frac{7}{2}}\exp(-b\mathcal{E})}{\omega_{tot} - \mathcal{D}\mathcal{E}}d\mathcal{E}\right\} &= -\frac{\pi}{\omega_{tot}b^{\frac{9}{2}}}\mathrm{Fn}_4(x), \quad \text{(B.4)}
\end{aligned}$$

with $x = \mathcal{D}/(b\,\omega_{tot})$. For $x > 0$, trapped ions magnetically precess in the same direction as ω_{tot} giving

$$\begin{aligned}
\mathrm{Fn}_{1+}(x) &= 4\sqrt{\pi}\frac{1}{x^{\frac{7}{2}}}\mathrm{erfi}\left(\frac{1}{\sqrt{x}}\right)\exp\left(-\frac{1}{x}\right) - \frac{3}{x} - \frac{2}{x^2} - \frac{4}{x^3}, \\
\mathrm{Fn}_{2+}(x) &= 4\sqrt{\pi}\frac{1}{x^{\frac{9}{2}}}\mathrm{erfi}\left(\frac{1}{\sqrt{x}}\right)\exp\left(-\frac{1}{x}\right) - \frac{15}{2x} - \frac{3}{x^2} - \frac{2}{x^3} - \frac{4}{x^4}, \\
\mathrm{Fn}_{3+}(x) &= \frac{1}{x^{7/2}}\exp\left[-\frac{1}{x}\right], \\
\mathrm{Fn}_{4+}(x) &= \frac{1}{x^{9/2}}\exp\left[-\frac{1}{x}\right],
\end{aligned} \tag{B.5}$$

where '+' denotes $x > 0$,

$$\mathrm{erfi}(x) = -i\mathrm{erf}(ix) = \frac{2}{\sqrt{\pi}}\int_0^x \exp(z^2)dz,$$

and $\mathrm{erf}(x)$ is the standard error function [54].

For $x < 0$, the energy integral does not contain a residue. This follows from the fact that the resonance condition $\omega_{tot} = \mathcal{D}\mathcal{E}$ cannot be met for any energy or radius if $x \propto \mathcal{D}/\omega_{tot} < 0$. However, the principle parts of Eq. (B.3) do not vanish:

$$\begin{aligned}
\mathrm{Fn}_{1-} &= -4\sqrt{\pi}\frac{1}{(-x)^{\frac{7}{2}}}\mathrm{erfc}\left(\frac{1}{\sqrt{-x}}\right)\exp\left(-\frac{1}{x}\right) - \frac{3}{x} - \frac{2}{x^2} - \frac{4}{x^3}, \\
\mathrm{Fn}_{2-} &= -4\sqrt{\pi}\frac{1}{(-x)^{\frac{9}{2}}}\mathrm{erfc}\left(\frac{1}{\sqrt{-x}}\right)\exp\left(-\frac{1}{x}\right) - \frac{15}{2x} - \frac{3}{x^2} - \frac{2}{x^3} - \frac{4}{x^4}, \\
\mathrm{Fn}_{3-} &= 0, \\
\mathrm{Fn}_{4-} &= 0,
\end{aligned} \tag{B.6}$$

where '$-$' denotes $x < 0$ and $\mathrm{erfc}(x) = 1 - \mathrm{erf}(x)$. From inspection of Eqs. (B.5) and (B.6), numerical difficulties are clearly envisaged at the pitch angle k_c^2 for which the magnetic precession drift of trapped ions is nullified; i.e. k_c^2 is defined by $x(k_c) = 0$. However, one can show that in the limit $x \to 0$ (or $k^2 \to k_c^2$), Fn_3 and Fn_4 vanish and Fn_1 and Fn_2 converge. Specifically, $\mathrm{Fn}_{1+}(k^2 = k_c^2) = \mathrm{Fn}_{1-}(k^2 = k_c^2) = 15/2$ and $\mathrm{Fn}_{2+}(k^2 = k_c^2) = \mathrm{Fn}_{2-}(k^2 = k_c^2) = 105/4$. To remove the numerical difficulties that arise from the cancellation of singular terms as $x \to 0$, Fn_1 and Fn_2 are numerically interpolated within the range $-1 < x < 1$ as depicted in Fig. B.1.

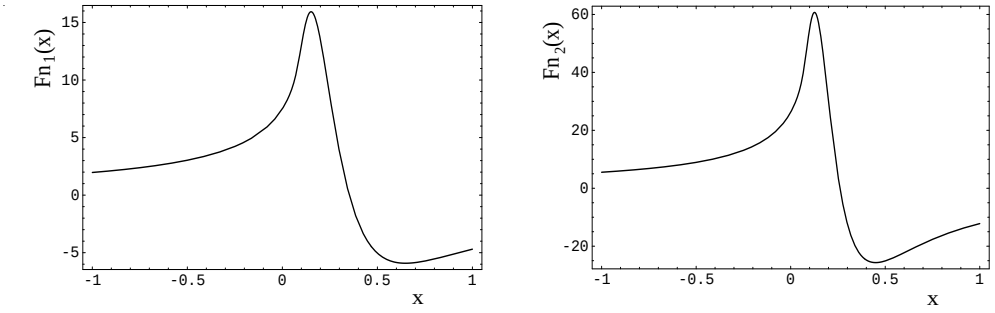

Figure B.1: Showing the numerically interpolated functions $\mathrm{Fn}_1(x)$ and $\mathrm{Fn}_2(x)$ against x within the range $-1 < x < 1$.

The following normalised quantities are now used:

$$\hat{n}_i = n_i/10^{19}\ \mathrm{m}^{-3}$$

$$\hat{T}_i = T_i/1\mathrm{keV}$$

$$\hat{\omega}_{tot} = \omega_{tot}/1\mathrm{k}\ \mathrm{rs}^{-1}.$$

Hence, referring to Eq. (6.22) for the definition of $\langle\omega_{mdi}\rangle$, yields

$$x(r,k^2) = \frac{q(r)\hat{T}_i(r)\left[F_1(k^2) + 2s(r)F_2(k^2) - \zeta(r)\left(\frac{1}{4q(r)^2} + F_3(k^2)\right)\right]}{B_0 R_0 Z r \hat{\omega}_{tot}(r)}, \tag{B.7}$$

and recalling the normalisation $\delta W = 6\pi^2 R_0 B_0^2 \xi_0^2 \varepsilon_1^4 \delta\hat{W}/\mu_0$, one can now show that

$$\Re\left\{\delta\hat{W}_{ki}\right\} = 0.151\times10^{-3}\left(\frac{1}{B_0^2\varepsilon_1^{3/2}r_1^{5/2}}\right)\int_0^{r_1} dr r^{\frac{1}{2}} \times\left[\left\{\frac{q\hat{T}_i}{B_0 Z\hat{\omega}_{tot}}\left(\hat{T}_i\frac{d\hat{n}_i}{dr} - \frac{3}{2}\hat{n}_i\frac{d\hat{T}_i}{dr}\right) + \hat{n}_i\hat{T}_i r\right\}\mathrm{G}_1 + \frac{q\hat{n}_i\hat{T}_i}{B_0 Z\hat{\omega}_{tot}}\frac{d\hat{T}_i}{dr}\mathrm{G}_2\right] \tag{B.8}$$

where $0.151\times10^{-3} = \frac{e\mu_0\times10^{22}}{3\sqrt{2}\,\pi}$, and

$$\mathrm{G}_1(r) = \int_0^1 \frac{F_q^2}{K(k^2)}\mathrm{Fn}_1\, dk^2 \ \text{ and } \ \mathrm{G}_2(r) = \int_0^1 \frac{F_q^2}{K(k^2)}\mathrm{Fn}_2\, dk^2, \tag{B.9}$$

with F_q defined by Eq. (6.21).

The pitch angle integrals are arranged as follows,

$$\mathrm{G}_1(r) = \int_{k_a}^{k_b}\frac{F_q^2}{K(k^2)}\mathrm{Fn}_{1+}\, dk^2 + \int_{k_d}^{k_e}\frac{F_q^2}{K(k^2)}\mathrm{Fn}_1\, dk^2 + \int_{k_f}^{k_g}\frac{F_q^2}{K(k^2)}\mathrm{Fn}_{1-}\, dk^2, \tag{B.10}$$

where Fn_1 is interpolated between the limits k_d and k_e which correspond to the interval $-1 < x < 1$. Numerical values are assigned to the integral limits of Eq. (B.10) by noting that $\langle\omega_{mdi}\rangle$ (and therefore $|x|$) is in general a monotonically decreasing function

of k^2 (at least for moderate values of ζ). For $\omega_{tot}(r) > 0$, the integration limits are defined: $k_a = 0$, $x(k_b) = x(k_d) = 1$, $x(k_e) = x(k_f) = -1$, $k_g = 1$. For $\omega_{tot}(r) < 0$, the integration limits are defined: $k_f = 0$, $x(k_e) = x(k_a) = 1$, $x(k_g) = x(k_d) = -1$, $k_b = 1$.

Since x is a function of r and k^2, then the limits k_a, k_b, k_d, k_e, k_f and k_g are also functions of r. Depending on the type of mode and the direction of the toroidal rotation, the sign of $\omega_{tot}(r)$ may change with respect to r and hence the definitions of the pitch angle integral limits must change appropriately throughout the radial integration.

The normalised imaginary kinetic potential energy is

$$\Im\left\{\delta\hat{W}_{ki}\right\} = -1.071\times10^{-3}\left(\frac{1}{B_0^2\varepsilon_1^{3/2}r_1^{5/2}}\right)\int_0^{r_1} dr r^{\frac{1}{2}} \times\left[\left\{\frac{q\hat{T}_i}{B_0 Z\hat{\omega}_{tot}}\left(\hat{T}_i\frac{d\hat{n}_i}{dr}-\frac{3}{2}\hat{n}_i\frac{d\hat{T}_i}{dr}\right)+\hat{n}_i\hat{T}_i r\right\}\mathrm{G}_3+\frac{q\hat{n}_i\hat{T}_i}{B_0 Z\hat{\omega}_{tot}}\frac{d\hat{T}_i}{dr}\mathrm{G}_4\right] \quad \text{(B.11)}$$

where $-1.071\times10^{-3} = \frac{2\sqrt{2}e\mu_0\times10^{22}}{3\sqrt{\pi}}$, and G_3 and G_4 are defined as follows. For $\omega_{tot}(r) > 0$:

$$\mathrm{G}_3(r) = \int_0^{k_c}\frac{F_q^2}{K(k^2)}\mathrm{Fn}_3\,dk^2 \text{ and } \mathrm{G}_4(r) = \int_0^{k_c}\frac{F_q^2}{K(k^2)}\mathrm{Fn}_4\,dk^2, \quad \text{(B.12)}$$

and for $\omega_{tot}(r) < 0$:

$$\mathrm{G}_3(r) = \int_{k_c}^{1}\frac{F_q^2}{K(k^2)}\mathrm{Fn}_3\,dk^2 \text{ and } \mathrm{G}_4(r) = \int_{k_c}^{1}\frac{F_q^2}{K(k^2)}\mathrm{Fn}_4\,dk^2. \quad \text{(B.13)}$$

The latter definitions of G_3 and G_4 emerge from the resonance of reverse magnetically precessing particles and thus tend to be small.

The radial and pitch angle integrals contained in Eqs. (B.8) and (B.11) are evaluated numerically. Examples of numerical results for various choices of equilibrium are used in Section 6.4.

Glossary

Distribution Functions

f_h	Hot (h) minority ion distribution function
f_i	Thermal ion (i) distribution function (Maxwellian)
$\delta f_{i,h}$	Perturbed (δ) thermal ion or hot ion (i,h) distribution function
δf_i^e	Perturbed distribution function corresponding to external (e) region
δf_i^s	Perturbed distribution function corresponding to singular (s) layer

Terms Appearing in Dispersion Relation

D	Dispersion relation $D = \delta K + \delta W = 0$
δK	Perturbed inertia
δW	Perturbed potential energy
δW_4	Perturbed potential energy satisfying $\delta W_4 \sim \varepsilon^4$, with $\varepsilon = r/R_0$
$\delta\hat{W}$	Normalised potential energy $\delta\hat{W} = \delta W/(6\pi^2 R_0 B_0^2 \xi_0^2 \varepsilon_1^4/\mu_0)$
δW_c	Perturbed potential energy term corresponding to core (c) plasma (thermal ions and electrons)
δW_f	Perturbed potential energy term corresponding to fluid (f) effects
δW_h	Perturbed potential energy term corresponding to the total contribution of hot minority ions (kinetic and fluid effects)
$\delta W_{ki,h}$	Perturbed potential energy term corresponding to the kinetic (k) effects of thermal ions or hot minority ions (i,h)
δW^S	Perturbed potential energy term corresponding to shaping (S) effects
δW^T	Perturbed potential energy term corresponding to toroidal (T) effects

Frequencies

γ	Mode growth rate defined by $\delta f \sim \exp(\gamma t)$
γ_I	Ideal MHD growth rate satisfying $\gamma_I \propto -\delta W$
ω	Mode frequency defined by $\omega^2 = -\gamma^2$ or $\delta f \sim \exp(-i\omega t)$
$\tilde{\omega}$	Shifted mode frequency $\tilde{\omega} = \omega - \Omega_\Phi(r_1)$
ω_A	Toroidal Alfvén (A) frequency $\omega_A = v_A/R_0$
$\omega_{*i,h}$	Diamagnetic ($*$) frequency (energy dependent) of thermal ions or hot minority ions
ω_{*pi}	Pressure (p) weighted ion diamagnetic frequency (energy independent)
$\omega_{di,h}$	Drift frequency $\omega_d = \omega_{md} + \Omega_\Phi$
$\langle\omega_{mdi,h}\rangle$	Bounce averaged ($<>$) magnetic (m) drift frequency
Ω	Toroidal plasma rotation satisfying $\Omega = \Omega_\Phi + \omega_{*pi}$
Ω_Φ	Toroidal plasma rotation caused by equilibrium electric potential (Φ)
$\hat{\Omega}_\Phi$	Normalised electrostatic toroidal plasma rotation defined $\hat{\Omega}_\Phi = \Omega_\Phi(r_1)/\omega_{*pi}(r_1)$

Special Functions

$K(k^2) = \int_0^{\pi/2} dx \Big/ \sqrt{1 - k^2 \sin^2 x}$	Complete elliptic integral of the first kind
$E(k^2) = \int_0^{\pi/2} dx \sqrt{1 - k^2 \sin^2 x}$	Complete elliptic integral of the second kind
$\Gamma(x) = \int_0^{\infty} dz\, z^{x-1} \exp(-z)$	Gamma function
$\mathrm{erf}(x) = \frac{2}{\sqrt{\pi}} \int_0^{x} dz\, \exp\left(-z^2\right)$	Standard Error function
$\mathrm{erfc}(x) = 1 - \mathrm{erf}(x)$	Complementary Error function
$\mathrm{erfi}(x) = \frac{2}{\sqrt{\pi}} \int_0^{x} dz\, \exp\left(z^2\right)$	Imaginary Error function with property $\mathrm{erfi}(x) = -i\mathrm{erfi}(ix)$

Bibliography

[1] J. D. Lawson, Proc. R. Soc. B **70**, 6 (1958).

[2] J. Jacquinot *et al*, Plasma Phys. Control Fusion **44** Supplement 3A, A13 (1999).

[3] K. Tamabechi, J. R. Gilleland, Yu. A. Sokolov, R. Toschi and the ITER team, Nucl. Fusion **31**, 1135 (1991).

[4] S. von Goeler, W. Stodiek and N. Sauthoff, Phys. Rev. Lett. **33**, 1201 (1974).

[5] I. B. Bernstein, E. A. Frieman, M. D. Kruskal and R. M. Kulsrud, Proc R. Soc London, A **244**, 17 (1958).

[6] T. M. Antonsen, B. Lane and J. J. Ramos, Phys. Fluids **24**, 1465 (1981).

[7] J. Jacquinot *et al*, in Plasma Phys. and Controlled Nucl. Fusion Research 1986 (IAEA, Vienna, 1987), Vol. 1, p449.

[8] D. J. Campbell *et al*, Phys. Rev. Lett. **60** 2148 (1988).

[9] J. C. Hosea and the TFTR group, *Proceedings of the Joint Varena-Lausanne International Workshop on Theory of Fusion Plasmas*, Varena, Italy, 1990 (Editrice Compositori, Bologna, Italy), p233.

[10] F. Porcelli, D. Boucher and M. N. Rosenbluth, Plasma Phys. Controlled Fusion **38**, 2163 (1996).

[11] D. J. Campbell *et al*, in Proc. 15th Eur. Conf. on Controlled Fusion and Plasma Heating (EPS, Dubrovnik, 1988), Vol. 12B, Part 1, p377.

[12] J. Blum, E. Lazzaro, J. O'Rourke, B. Keegan and Y. Stephan, Nucl. Fusion **30**, 1475 (1990).

[13] V. D. Shafranov, Sov. Phys. Tech. Phys. **15**, 175 (1970).

[14] M. N. Rosenbluth, P. Y. Dagazian and P. H. Rutherford, Phys. Fluids **16**, 1894 (1973).

[15] M. N. Bussac, R. Pellat, D. Edery and J. L. Soulé, Phys. Rev. Lett. **35**, 1638 (1975).

[16] A. H. Glasser, J. M. Green and J. L. Johnson, Phys. Fluids **18**, 875 (1975).

[17] M. N. Bussac, D. Edery, R. Pellat and J. L. Soule, in Plasma Phys. and Controlled Nucl. Fusion Research 1976 (IAEA, Vienna 1977), Vol. 1, p607.

[18] G. Ara, B. Basu, B. Coppi, G. Laval, M. N. Rosenbluth and B. V. Waddell, Annals of Physics **112**, 443 (1978).

[19] B. Coppi, R. Galvao, R. Pellat, M. N. Rosenbluth and P. H. Rutherford, Sov. J. Plasma Phys. **2**, 533 (1976).

[20] R. J. Hastie, *Sawtooth Instability in Tokamak Plasmas*, UKAEA Fusion Plasma Physics Note 97/11.1.

[21] T. M. Antonsen, in Theory of Fusion Plasmas, (eds A. Bondeson, E. Sindoni and F. Troyon), Editrice Compositori Bologna, Varenna (1987), p161.

[22] M. D. Kruskal and C. R. Oberman, Phys. Fluids **1**, 275 (1958).

[23] R. J. Hastie and T. Hender, Nucl. Fusion **28**, 585 (1988).

[24] G. Fogaccia and F. Romanelli, in Theory of Fusion Plasmas, Editrice Compositori Bologna, Varenna (1992), p351.

[25] T. M. Antonsen and Y. C. Lee, Phys. Fluids **25**, 142 (1982).

[26] J. W. Connor, R. J. Hastie, T. J. Martin and M. F. Turner, in *Proceedings of the 3rd Joint Varenna-Grenoble International Symposium on Heating in Toroidal Plasmas, CEC, Brussels, 1982*, Vol 1, p65 (1982).

[27] K. McGuire *et al* Phys. Rev. Lett. **50**, 891 (1983).

[28] L. Chen, R. B. White and M. N. Rosenbluth, Phys. Rev. Lett. **52**, 1122 (1984).

[29] B. Coppi and F. Porcelli, Phys. Rev. Lett. **57**, 2272 (1986).

[30] R. B. White *et al.*, Phys. Rev. Lett. **60**, 2038 (1988).

[31] R. B. White, M. N. Bussac and F. Romanelli, Phys. Rev. Lett. **62**, 539 (1989).

[32] B. Coppi, P. Detragiachi, S. Migliuolo, F. Pegoraro and F. Porcelli, Phys. Rev. Lett. **63**, 2733 (1989).

[33] F. Porcelli, Plasma Phys. Controlled Fusion **33**, 1601 (1991).

[34] T. G. Northrop, The Adiabatic Motion of Charged Particles (Interscience, New York 1963).

[35] F. Pegoraro, F. Porcelli, B. Coppi, P. Detragiachi and S. Migliuolo, in Plasma Physics and Controlled Nuclear Fusion Research 1988 (IAEA, Vienna 1989), Vol. 2, p243.

[36] F. Porcelli, D. J. Campbell, W. D. Diachenko, L. G. Eriksson, J. Jacquinot *et al*, in Proc. 15th Eur. Conf. on Controlled Fusion and Plasma Heating (EPS, Dubrovnik, 1990), Vol. 12B, Part 1, p377.

[37] C. K. Phillips and the TFTR Group, Phys. Fluids **4**, 2155 (1992).

[38] T. C. Hender, R. Fitzpatrick, A. W. Morris, P. G. Carolan, R. D. Durst, *et al*, Nucl. Fusion **32**, 2091 (1992).

[39] R. O. Dendy, R. J. Hastie, K. G. McClements and T. J. Martin, Phys. Plasmas **2**, 1623 (1995).

[40] T. H. Stix, Nucl. Fusion **15**, 737 (1975).

[41] K. G. McClements, R. O. Dendy, R. J. Hastie and T. J. Martin, Phys. Plasmas **3**, 2994 (1996).

[42] A. B. Mikhailovskii, Sov. J. Plasma Phys **9**, 190 (1983).

[43] D. Edery *et al*, Phys. Fluids **19**, 260 (1976).

[44] G. Fogaccia and F. Romanelli, Phys. Plasmas **2**, 227 (1994).

[45] T. M. Antonsen Jr. and A Bondeson, Phys. Rev. Lett. **71**, 2046 (1993).

[46] A. B. Mikhailovskii and V. S. Tsypin, Sov J . Plasma Phys. **9**, 91 (1983).

[47] F. Romanelli, L. Chen and R. B. White, Nucl. Fusion **31**, 631 (1991).

[48] G. Laval, C. Mercier and R. M. Pellat, Nucl. Fusion **5**, 156 (1965).

[49] H. P. Furth, Plasma Phys. and Controlled Nuclear Fusion Research 1964, (IAEA, Vienna, 1965), Vol. 1, p103.

[50] J. P. Freidberg *Ideal Magnetohydrodynamics.* Plenum Press, New York (1987).

[51] V. D. Shafranov, Soviet Physics JETP **6**, 545 (1958).

[52] J. W. Connor and R. J. Hastie, Culham Laboratory report CLM-M106 (1985).

[53] H. P. Furth, J. Killeen and M. N. Rosenbluth, Phys. Fluids **6**, 459 (1963).

[54] M. Abramowitz and I. A. Stegun *Handbook of Mathematical Functions.* Dover Publications, Inc, New York (1965).

[55] R. B. White *Theory of Tokamak Plasmas.* North Holland, Amsterdam (1989).

[56] M. N. Rosenbluth and M. L. Sloan, Phys. Fluids **14**, 1725 (1971).

[57] T. M. Antonsen, Jr. and B. Lane, Phys. Fluids **23**, 1205 (1980).

[58] G. F. Chew, M. L. Goldberger and F. E. Low, Proc. R. Soc. London, **A236**, 112 (1956).

[59] J. B. Taylor and R. J. Hastie, Phys. Fluids **8**, 323 (1965).

[60] R. J. Hastie, Private Communication (1998).

[61] N. A. Madden and R. J. Hastie, Nucl. Fusion **34**, 519 (1994).

[62] M. Yamada *et al* Phys. Plasmas **1**, 3269 (1994).

[63] A. Weller *et al*, Phys. Rev. Lett. **59**, 2303 (1987).

[64] R. W. Harvey, M. G. McCoy, G. D. Kerbel and S. C. Chiu, Nucl. Fusion **26**, 43 (1986).

[65] L.-G. Eriksson, T. Hellsten and U. Willén, Nucl Fusion **33**, 1037 (1993).

[66] A. A. Korotkov, A. Gondhalekar and A. J. Stuart, Nucl. Fusion **37**, 35 (1997).

[67] F. Porcelli and S. Migliuolo, Phys. Fluids **29**, 1741 (1986).

[68] L. Zackharov, B. Rogers and S. Migliuolo, Phys. Fluids B **5**, 2498 (1993).

[69] F. M. Levinton, L. Zackharov, S. H. Batha, J. Manickam and M. C. Zarnstorff, Phys. Rev. Lett. **72**, 2895 (1994).

[70] D. F. Start *et al*, Phys. Rev. Lett. **80**, 4681 (1998).

[71] D. Wroblewski, L. K. Huang and H. W. Moos, Phys. Rev. Lett. **61**, 1724 (1988).

[72] J. P. Graves, K. I. Hopcraft, R. O. Dendy, R. J. Hastie, K. G. McClements and M. Mantsinen, UKAEA Fusion Plasma Phys. Note, 99/4.1.

[73] J. P. Graves, K. I. Hopcraft, R. O. Dendy, R. J. Hastie, K. G. McClements and M. Mantsinen, Phys. Rev. Lett. **84**, 1204 (2000).

[74] L.-G. Eriksson *et al.*, Phys. Rev. Lett. **81**, 1231 (1998).

[75] L.-G. Eriksson, E. Righi and K.-D. Zastrow, Phys. Control Fusion **39**, 27 (1997).

[76] H. J. de Blank, 17th Euro. Proc. Phys. Soc. Conf. (Controlled Fusion and Plasma Physics), **2**, 919 (1990).

[77] R. J. Hastie, Private Communication (1997).

[78] J. W. Connor, R. J. Hastie and T. J. Martin, Nucl. Fusion **23**, 1702 (1983).

[79] T. S. Taylor E. J. Strait, L. L. Lao, M. Mauel, A. D. Turnbull, *et al*, Phys. Plasmas **2**, 2390 (1995).